Simulation and Growth of Cadmium Zinc Telluride from Small Seeds by the Travelling Heater Method

by

Jordan Douglas Roszmann
B.Eng., University of Victoria, 2006
M.A.Sc., University of Victoria, 2009

A Dissertation Submitted in Partial Fulfillment of the
Requirements for the Degree of

DOCTOR OF PHILOSOPHY

in the Department of Mechanical Engineering

Simulation and Growth of Cadmium Zinc Telluride from Small Seeds by the Travelling Heater Method

by

Jordan Douglas Roszmann
B.Eng., University of Victoria, 2006
M.A.Sc., University of Victoria, 2009

Supervisory Committee

Dr. Sadik Dost, Supervisor
(Department of Mechanical Engineering)

Dr. Peter Oshkai, Departmental Member
(Department of Mechanical Engineering)

Dr. Thomas Tiedje, Outside Member
(Department of Electrical and Computer Engineering)

Supervisory Committee

Dr. Sadik Dost, Supervisor
(Department of Mechanical Engineering)

Dr. Peter Oshkai, Departmental Member
(Department of Mechanical Engineering)

Dr. Thomas Tiedje, Outside Member
(Department of Electrical and Computer Engineering)

ABSTRACT

The semiconducting compounds CdTe and CdZnTe have important applications in high-energy radiation detectors and as substrates for infrared devices. The materials offer large band gaps, high resistivity, and excellent charge transport properties; however all of these properties rely on very precise control of the material composition. Growing bulk crystals by the travelling heater method (THM) offers excellent compositional control and fewer defects compared to gradient freezing, but it is also much slower and more expensive. A particular challenge is the current need to grow new crystals onto existing seeds of similar size and quality.

Simulations and experiments are used in this work to investigate the feasibility of growing these materials by THM without the use of large seed crystals. A new fixed-grid, multiphase finite element model was developed based on the level set method and used to calculate the mass transport regime and interface shapes inside the growth ampoule. The diffusivity of CdTe in liquid tellurium was measured through dissolution experiments, which also served to validate the model. Simulations of tapered THM growth find conditions similar to untapered growth with interface shapes that are sensitive to strong thermosolutal convection. Favourable growth conditions are achievable only if convection can be controlled.

In preliminary experiments, tapered GaSb crystals were successfully grown by THM and large CdTe grains were produced by gradient freezing. Beginning with this seed material, 25 mm diameter CdTe and CdZnTe crystals were grown on 10 mm diameter seeds, and 65 mm diameter CdTe on 25 mm seeds. Unseeded THM growth was also investigated, as well as ampoule rotation and a range of thermal conditions and ampoule surface coatings. Outward growth beyond one or two centimeters was achieved only at small diameters and included secondary grains and twin defects; however, limited outward growth of larger seeds and agreement between experimental and numerical results suggest that tapered growth may be achievable in the future. This would require active temperature control at the base of the crystal and reduction of convection through thermal design or by rotation of the ampoule or applied magnetic fields.

Contents

Table of Contents **v**

List of Tables **viii**

List of Figures **ix**

Acronyms **xiv**

Symbols **xvi**

Acknowledgements **xix**

Dedication **xx**

1 Introduction **1**
1.1 Contributions 2

2 Background **3**
2.1 Semiconducting Compounds 3
2.1.1 Zincblende Crystal Structure 5
2.1.2 CdTe and CdZnTe 6
2.2 Growth Techniques 10
2.2.1 Vertical Gradient Freezing 11
2.2.2 Travelling Heater Method 12

3 Motivation for CdZnTe THM Growth Using Small Seeds **17**
3.1 THM Experiments in GaSb 18

4 Supporting Technology **22**
4.1 General Experimental Considerations 22
4.1.1 Materials and Preparation 22

4.1.2 Cutting tools . . . 24
4.2 Zone Purification of Source Materials . . . 26
4.3 Synthesis of Source Material by Fast THM . . . 29
4.3.1 Source Material for FOTON 12 M4 Program . . . 31
4.4 Production of Seeds by VGF . . . 35
4.4.1 Superheating of the Melt . . . 35
4.4.2 Procedure . . . 36
4.4.3 Results of VGF Experiments . . . 37
4.4.4 Discussion . . . 38
4.4.5 Conclusion . . . 40
4.5 Dissolution Experiments . . . 40
4.5.1 Motivation . . . 40
4.5.2 Experimental Procedure . . . 41
4.5.3 Analysis . . . 42
4.5.4 Results . . . 43
4.5.5 Discussion . . . 44
4.5.6 Conclusions . . . 47

5 Experimental THM Growth of CdTe and CdZnTe 48
5.1 THM Growth Experiments . . . 48
5.2 Overview of the THM Experimental Study . . . 48
5.3 Experimental Procedure . . . 50
5.3.1 Equipment . . . 51
5.3.2 Ampoule Development for 25 mm CdTe Growth . . . 54
5.4 Unseeded Growth . . . 58
5.5 Seeded Growth of CdZnTe . . . 62
5.5.1 Ampoule Rotation . . . 62
5.5.2 Fixture of Seed Crystals . . . 64
5.5.3 Seeded 65 mm Diameter Growth . . . 68
5.6 Discussion . . . 69
5.7 Conclusion . . . 74

6 Finite Element Simulation of THM Growth Experiments 76
6.1 Introduction . . . 76
6.2 The Enriched Finite Element Model . . . 78

6.2.1 Governing Equations for the Stefan-Type Problem 78
6.2.2 Material Properties 85
6.2.3 Discretization by Weighted Residuals 86
6.2.4 Enrichment by Virtual Interface Elimination 98
6.3 Details of the Simulation Software 110
6.3.1 Open Source Workflow 110
6.3.2 Structure of the Deal.II Simulation Application 111
6.4 1D Simulation of Dissolution and THM 117
6.5 Axisymmetric Simulation of THM Growth 123
6.5.1 Velocity Field 123
6.5.2 Convection and Interface Shape 126
6.6 Discussion 128
6.7 Conclusion 131
6.8 Future Work 132

7 Results and Discussion **133**
7.1 Supporting Studies 133
7.2 Simulations and THM Growth Experiments 134

8 Conclusion **137**
8.1 Conclusion 137
8.2 Future Work 139

Bibliography **140**

List of Tables

Table 2.1 Selected solid and liquid properties for several semiconductors [12, 7] 10

Table 3.1 Summary of GaSb THM growth experiments 18
Table 3.2 Dimensionless quantities for gallium and tellurium THM solutions 21

Table 4.1 Sample specification for FOTON growth project 32
Table 4.2 Samples of feed material delivered for FOTON M4 experiments 33
Table 4.3 Solidification experiments for seed production. 37
Table 4.4 Experimental results 44

Table 5.1 Summary of THM experiments 49

Table 6.1 Material properties used in THM simulations 85
Table 6.2 Basis and test functions used for several weighted residuals formulations. 88
Table 6.3 Update equations for three time stepping schemes. 94
Table 6.4 Workflow and software for the simulations 109
Table 6.5 Key components of the simulation application 112
Table 6.6 Outline of the simulation software with key class methods 116

List of Figures

Figure 2.1 Band structure schematics for silicon, CdTe, and CdZnTe . . . 4
Figure 2.2 The zincblende crystal structure with interpenetrating A and B sub-lattices. At right, the structure is oriented for growth with the (111)A plane facing upward. 6
Figure 2.3 Operation of a x- or γ-ray detector 7
Figure 2.4 Equilibrium phase diagram of $Cd_{1-x}Zn_xTe$ for the values of x used in this project. The existence region of 0.5 ± 10^{-3} is expanded in log scale for clarity. Data from [9, 10, 11] 8
Figure 2.5 Peudobinary phase diagram for the CdTe-ZnTe system, plotted with data from Steininger [9] 9
Figure 2.6 Vertical gradient freezing or Bridgman growth configuration . 13
Figure 2.7 Growth configuration for the travelling heater method 13

Figure 3.1 Top row: Tapered GaSb growth was successful at 2 mm/d but not at 5 mm/d. Bottom row: Under increasingly strong RMF, growth improved with fewer and more structured grains produced even at 5 mm/d [24]. 19
Figure 3.2 Etch pits in GaSb25 appear to show the state of the growth interface when the translation rate was increased from 2 mm/d to 5 mm/d. Right: Preliminary simulations suggested that the thermal conditions in the tapered growth system are similar to those in a straight ampoule [24]. 20

Figure 4.1 Left to right: pits on (111)A surfaces of CdTe65-7 etched with dilute aqua regia, with E-Ag, with E followed by Nakagawa, and with modified Everson followed by Nakagawa etch. 24
Figure 4.2 Tape and wire slurry saws used to cut CdTe and CdZnTe samples 25
Figure 4.3 Core drilling of a 25 mm seed, and shop drawing of a cutting tool (Dimensions in inches) 25

Figure 4.4 The different liquidus and solidus concentrations at at the equilibrium interface temperature results in preferential exclusion or incorporation of solute into the advancing solid. Right: The zone refining test apparatus passes three zones at a time through an ingot with RMF applied to the centre zone. 26
Figure 4.5 The distribution of an impurity after n zone refining passes depends strongly on the effective segregation coefficient, k. Distributions were calculated for a zone length equal to 0.1 times the ingot length using Hamming's method as described by Pfann [28]. 27
Figure 4.6 Schematic of a THM synthesis experiment. 30
Figure 4.7 Left: CdTe65-1 prior to growth Right: Ingot resulting from CdZnTe65-2 30
Figure 4.8 $Cd_{1-x}Zn_xTe$ sample F1-003-FM cast by rapid travelling heater method (THM) for growth experiments on the FOTON M4 satellite. Large grains in the first-to-freeze region of the casting experiments motivated unseeded experiments in the CdZnTe growth study. 34
Figure 4.9 Schematic of the VGF apparatus 36
Figure 4.10 CdTeVB1 before removal from its ampoule. 38
Figure 4.11 Left: Hemispherical tip of CdTeVB3 with visible twin planes. Right: Slabs and a seed cut from CdTeVB3. 38
Figure 4.12 Left: CdTeVB5 during cutting. Right: Typical etch pits from E-Ag solution used to identify the (111A) face of a CdTe slab. 39
Figure 4.13 Quartz crucible prior to processing. 41
Figure 4.14 Predicted interface displacement (solid lines) after fitting the diffusivity to the experimental data. Dashed lines indicate the effect of increasing or decreasing D by $0.001\,mm^2/s$. 45
Figure 4.15 Solution zones after 45, 90 and 180 min at 900 °C. Rectangle is a representative EDS view frame. 45
Figure 4.16 Calculated and measured mole fraction profiles after 45, 90 and 180 min of dissolution at $T = 900\,°C$, $D = 0.009\,mm^2/s$. . . . 46
Figure 4.17 Diffusivities (mm^2/s) measured in this work (white), and calculated by Ko et al. (black)[39]. 47

Figure 5.1 25 mm THM furnace mounted on an open frame for CdTe experiments and enclosed prior to CdZnTe experiments. Right: Ampoule mounted on the final growth pedestal. 52
Figure 5.2 65 mm THM furnace shown prior to CdTe65-6 and opened during replacement of the furnace core 53
Figure 5.3 Final cold finger configurations for the 25 mm and 65 mm THM furnaces. Two thermocouples mounted at opposite ends of a reduced diameter, insulated length were used to approximately measure the heat flux out of the base of the ampoule. 55
Figure 5.4 CdTe12-0 was a typical experiment in untreated quartz ampoules. 56
Figure 5.5 CdTe-13 (left) and CdTe-14, grown in ampoules treated with a sprayed boron nitride surface coating. 57
Figure 5.6 Sand blasted ampoule, as used in CdTe-17 - CdTe-22. Dimensions are in mm. 57
Figure 5.7 CdTe-22 exhibited nearly single-crystal growth expanding from 10 mm diameter to 25 mm 58
Figure 5.8 Left to right: CdZnTe-1 showed large grains after a fine-grain tip region. In an effort to reduce supercooling at the tip, the carbon coating was scratched away in the tip of CdZnTe-2. Both experiments rested on 5 mm of boron nitride on top of a copper pedestal. Insulation surrounded the ampoule tip to a height of 5 mm. 59
Figure 5.9 Clockwise from top left: CdTe65-3,4,6 and 5. From CdTe65-3 to CdTe65-5 progressively more heat extraction yielded larger grains in the bulk but poorer initial nucleation. CdTe65-6 attempted to vary the heat extraction during growth, but it was curtailed by failure of the furnace core. 60
Figure 5.10 Left: Ingot resulting from CdZnTe-6. Right: 10 mm diameter CdZnTe seed recovered from the centre of CdZnTe-6. 63
Figure 5.11 Left: CdZnTe-3 showed a highly asymmetric solution zone and growth interface (marked in white for illustration). Right: Accelerated ampoule rotation in CdZnTe-7 resulted in a more uniform interface and a more axisymmetric system. 63

Figure 5.12 Left: Concave, asymmetric growth interface in CdTe65-7. Right: Accelerated ampoule rotation resulted in a more symmetric growth interface shape in CdTe65-8. 65
Figure 5.13 Left: Slight ridge around the base of CdTe-18 which locked the seed in place. Right: A deliberate 0.5 mm radius was added at the base of CdZnTe-3 in order to allow crystals to be removed intact. 65
Figure 5.14 Left to right: CdZnTe-7 during and after the torching procedure to secure the seed crystal, and the bottom 4 mm of seed locked in place after the remainder of CdZnTe-6 was removed from the ampoule. 67
Figure 5.15 In CdTe65-7 The seed appears intact with nearly single-crystal growth in the first 20 mm of growth followed by large grains with [111] orientation. 68
Figure 5.16 Left: The last to freeze region and final growth interface of CdTe65-8. Right: Single crystal growth was established at the seed and progressed for 15 mm before large grains appeared. . 69
Figure 5.17 Heat flow measured in the support pedestal during thermal profiling of 25 mm experiments. 71
Figure 5.18 Measured wall and axis temperatures during profiling of the 25 mm THM furnace 72

Figure 6.1 Relationship of the steady thermo-solutal convection model and the transient mass transport model. 79
Figure 6.2 Liquidus tellurium content of a Te - $Cd_XZn_{1-X}Te$ mixture as a function of interface temperature and X. Curves are approximated by least-squares to data from [9]. 84
Figure 6.3 Within applied mathematics (left), linear finite elements form a subset of Bubnov-Galerkin weighted residuals methods for approximating the solutions of partial differential equations. Within engineering (right), weighted-residuals formulations are often presented as a branch within finite element analysis. Numerical simulations can also be developed through physical arguments from assemblies of simple bodies or by applying balance laws directly to small volumes. 89

Figure 6.4 Piecewise-constant shape functions for the finite volume method, and linear shape functions for the finite element method . . . 90
Figure 6.5 Normalized linear, quadrilateral and triangular elements with their canonical vertex numbering and typical quadrature points 95
Figure 6.6 A six-patch of elements divided into liquid and solid subdomains Ω_l and Ω_s. Mixed-phase elements are subdivided into patches of single-phase elements. 99
Figure 6.7 Canonical vertex numbering for 1D and axisymmetric mixed phase elements. With quadrilateral elements, two topologies are permitted. Diagonal elements, shown at right, are ambiguous and not allowed. 100
Figure 6.8 Subdivision of a mixed element into regions with positive and negative level set values. The process is identical for a 1D element or along the edge of a 2D element. 101
Figure 6.9 Meshes used for the 25 mm (left) and 65 mm diameter simulations. Centre: Refined mesh to resolve boundary layers near interfaces and the axis. 109
Figure 6.10 A liquid vertex solidifies when the level set, ϕ becomes smaller than $|\phi|_{min}$. The level set is pushed to $-|\phi|_{min}$ to prevent overly large gradients, and the solute fraction, X is set to the solid composition. 114
Figure 6.11 Dissolved distance under diffusive conditions as determined by the analytical solution, experiments and the EVIE simulations. 118
Figure 6.12 Interface displacement in 1D simulations using increasing mesh density. 119
Figure 6.13 Effect of the maximum allowable change in the liquid mole fraction per time step on the calculated interface position after three hours of simulated dissolution using 2^{11} elements. 120
Figure 6.14 Effect of the maximum allowable interface motion per time step on the calculated interface position after three hours of simulated dissolution using 2^{11} elements. 120
Figure 6.15 1D simulation of ternary THM growth at 2 mm/d. 121
Figure 6.16 1D simulation of ternary THM growth at 10 mm/d. 122

Figure 6.17 Velocity vectors and contours of v_r and v_z for a 25 mm diameter tellurium solution zone. Left: Strong initial flow with $v_{max} = 20\,\text{mm/s}$ as CdTe first dissolves into the solution. Right: Weaker thermal convection with $v_{max} = 5\,\text{mm/s}$ after the solution composition has become uniform. 124

Figure 6.18 Sensitivity of the velocity field to the choice of penalty parameter, λ. At values of $\lambda > 5\times10^6$ the flow structure stays the same and velocity is inversely proportional to λ. When the number of liquid elements is doubled, the flow structure is consistent for $\lambda > 10^6$. Diameter is 65 mm 125

Figure 6.19 25 mm diameter growth experiment with a 10 mm seed. $v_{max} = 5\,\text{mm/s}$, $Re = 600$. 126

Figure 6.20 Left: Translation begins with a THM solution that is not quite at steady state. Right: After 6 h the growth interface becomes concave. 127

Figure 6.21 25 mm simulation with lower temperature gradients. $u_{max} = 1.5\,\text{mm/s}$, $Re = 180$ 130

Acronyms

AAR accelerated ampoule rotation

CRSS critical resolved shear stress

deal.II Differential Equations Analysis Library

EDS energy dispersive X-ray spectroscopy

EVIE enrichment by virtual interface elimination

FEM finite element method

FVM finite volume method

LBB Ladyzhenskaya-Babuška-Brezzi

LEC liquid encapsulated Czochralski

LSM level set method

RMF rotating magnetic field

THM travelling heater method

VGF vertical gradient freezing

XFEM extended finite element method

Symbols

A advection matrix

C_A mass concentration of CdTe

C_B mass concentration of ZnTe

$\boldsymbol{d}$ deformation rate tensor

$\boldsymbol{f}$ gravitational body force

Gr_C solutal Grashof number

Gr_T thermal Grashof number

H height of the liquid solution

h heat transfer coefficient

h_L latent heat

$\boldsymbol{i}$ solute flux

K generalized stiffness matrix

k thermal conductivity

k_e effective segregation coefficient

k_0 equilibrium segregation coefficient

L ingot length

l liquid zone length

M generalized mass matrix

N_i finite element shape function

Pr Prandtl number

p pressure

$\boldsymbol{q}$ heat flux

R radius of the ampoule

Ra_C solutal Rayleigh number

Ra_T thermal Rayleigh number

Re Reynolds number

c_p specific heat capacity

T temperature

T_∞ furnace wall temperature

u_n normal interface velocity

$\boldsymbol{v}$ velocity

W weights for Gaussian quadrature

X_A mole fraction of CdTe

X_B mole fraction of ZnTe

α thermal diffusivity

β_C solutal expansion coefficient

β_T thermal expansivity

Γ domain boundary

δ boundary layer thickness

δ_{ij} Dirac delta function

η, ζ isoparametric natural coordinates

Λ matrix of penalty terms

λ penalty parameter

ν kinematic viscosity

ρ density

$\boldsymbol{\sigma}$ stress tensor

ϕ level set function

Ω domain volume

ω relaxation parameter

ACKNOWLEDGEMENTS

With deep gratitude, I happily thank

Andrea for extraordinary patience during this study,

Our Parents for supporting our family throughout this work,

Dr. Sadik Dost for the long term support needed to study slow processes,

5N Plus Inc. for financial and material support, and

The Natural Sciences and Engineering Research Council

DEDICATION

For Genevieve and Jack

Chapter 1

Introduction

Cadmium zinc telluride has long been recognized as a valuable electronic material. As a wide band-gap semiconductor, it can be used at room temperature for X-ray and γ-ray spectrometry and medical imaging, and its high electrical resistivity reduces both power consumption and noise compared to more common silicon and germanium. Importantly, because CdZnTe is a ternary compound its properties depend on its composition, so by controlling the proportion of zinc, CdZnTe can be tuned for specific applications. In addition to bandgap tuning, CdZnTe can be lattice-matched to produce substrates for the growth of infrared focal plane arrays from HgCdTe.

Unfortunately, the very properties that make CdZnTe useful also make it difficult to produce. While electrical resistivity is very helpful in a semiconducting material, the associated thermal resistivity leads to advective energy transfer during production. Because the compound's properties depend strongly on its composition, the stoichiometric control necessary to achieve high resistivity greatly complicates traditional methods used to grow large semiconducting crystals. The methods that have been developed by industry for producing CdZnTe are therefore very slow, labour-intensive and expensive.

This feasibility study attempts to combine the features of several growth methods in order to seek a more affordable way to produce CdZnTe. Solution-based THM growth is employed to achieve control over the product composition, but techniques are incorporated from melt-growth methods such as unseeded growth and growth from small seed crystals. THM growth from small seeds has previously been demonstrated by the author for GaSb. The purpose of this project is to determine whether that success can be replicated in CdZnTe, which is a much more difficult material to produce.

To this end a long course of THM experiments were conducted using several growth configurations. These growth experiments were preceded by preliminary studies to produce seed and source material and to measure material properties needed for associated simulations. Unfortunately, CdTe and CdZnTe boules produced under the conditions studied all contained secondary grains and twin defects; however, there is reason to think that single crystal growth is achievable with improved equipment.

In addition to the experimental study, a new multiphase finite element transport model was developed in order to investigate the effect of applied experimental conditions on growth. The simulations used a new fixed-grid algorithm to track the growth interface. Unfortunately the development of this model was badly delayed by challenges in its implementation and by the frequency of the later experiments so that simulation results were not available until after the experimental study was concluded. The model does however give insight into the experimental conditions that were achieved and what should be changed in future experiments if tapered growth is to be achieved.

1.1 Contributions

This work brings the following contributions to the simulation and growth of compound semiconductiors.

The level set method was employed in a new way to simulate the liquid and solid regions of a tellurium-cadmium-zinc mixture together in a single axisymmetric domain with an unstructured quadrilateral mesh. The method consists of constructing a virtual interface within each mixed-phase element and then eliminating the interfacial terms algebraically from the element matrices. This process of enrichment by virtual interface elimination is adapted and expanded from methods published using triangular elements for Stefan problems such as the melting of pure materials.

The diffusivity of CdTe was measured in liquid tellurium at temperatures similar to those of THM growth.

GaSb crystals were grown at 25 mm diameter from 10 mm seeds, and a CdTe crystal was grown out to 25 mm diameter from 10 mm diameter seed. Large grains were observed in 25 mm diameter CdZnTe grown from 10 mm diameter CdTe and CdZnTe seeds and in 65 mm diameter CdTe boules grown without seeds and using 25 mm seeds. These experimental results suggest that tapered THM growth is possible given sufficient development, but it has not been demonstrated in this work.

Chapter 2

Background

The majority of electronic devices such as sensors and integrated circuits are fabricated from single crystals of semiconducting materials. Due to their very small size, the performance of these devices depends strongly not only on a material's macroscopic properties, but often on lattice defects such as interstitial atoms, dislocations or grain boundaries. Progress in the size and performance of radiation detectors, focal plane arrays and other devices demands ever larger crystals of semiconducting materials with more precise composition and fewer internal defects.

This project focuses mainly on the heat and mass transport phenomena inside the metallic liquid solution of a crystal growth experiment; however, an overview of semiconducting compounds and the techniques used to produce them is presented here briefly to give context and motivation for the current study.

2.1 Semiconducting Compounds

In a semiconductor, only a very small proportion of electrons have enough energy to move through the crystal lattice. Electrons bound to their atoms are said to occupy valence states, and those that can move through the material occupy conduction states. The minimum energy required to excite an electron from a valence to a conduction state is the material's band gap. Silicon is the most widely used semiconductor for a wide range of applications; however it has an indirect bandgap, as seen in Figure 2.1, which means that the highest energy valence states occur in silicon at a different momentum than the minimum energy conduction states [1]. Because of this, electrons changing between valence and conduction states must exchange momentum

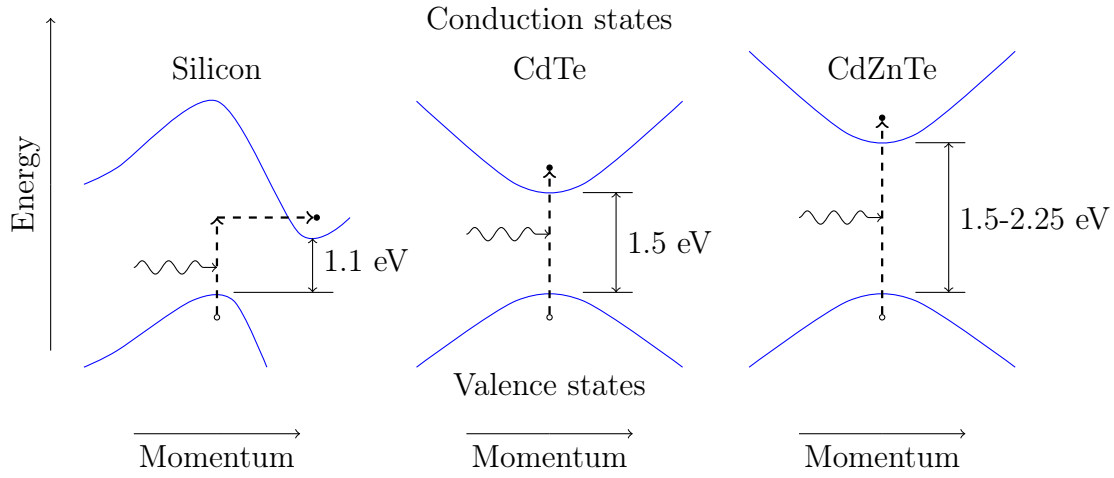

Figure 2.1: Band structure schematics for silicon, CdTe, and CdZnTe

with the lattice through a phonon in addition to absorbing or releasing a photon. CdTe, by contrast, is a direct-bandgap semiconductor with a larger band gap than silicon. Electrons in CdTe do not need to change momentum while absorbing or releasing photons and are therefore much more likely to interact. CdZnTe is also direct, and its bandgap varies with composition. The distinction between direct and indirect semiconductors is important for photoelectric devices. Compared to silicon, a smaller proportion of the photons striking a CdTe photovoltaic panel will be energetic enough to overcome the large band gap and produce charge carriers, but much more photons will interact with the material because the band gap is direct. A 2 µm layer of CdTe may therefore capture energy as efficiently as a 250 µm thick silicon wafer [2].

If a material's band gap is small, infrared or visible photons may carry enough energy to produce charge carriers, but thermal excitation can also produce carriers unless the material is kept cold. Larger band gap materials may be excited only by higher energy photons, and there are fewer thermally excited carriers. In the context of a detector for X-rays or γ-rays, a large band gap material will have lower leakage current and produce less noise due to heat or visible light [3].

In pure silicon or a pure compound such as CdZnTe, covalent bonding binds all of the electrons within the lattice except for a small proportion of intrinsic carriers that are excited into conduction states. An impurity atom or dopant may, however, have the wrong number of valence electrons to bond seamlessly in the structure of the material. Elements such as Al, Cl and Ga contain additional electrons and act as donors, producing n-type material. As, Cu, Li, Ag, Bi and others have a deficient

number of valence electrons, and these act as acceptors, producing p-type material by contributing positively charged carriers (holes). Unless impurity concentrations are kept very low, these extrinsic charge carriers dominate the material's electrical properties.

Two other electrical properties that are important for material used in detectors are the carrier mobility lifetime product, $\mu\tau$, which is a measure of how far excited charge carriers move through the material before recombining, and the resistivity, which determines the amount of leakage current from carriers that are not created by the incident radiation.

Elemental semiconductors silicon and germanium have the most established technology, and their properties favour the growth of very large boules by the Czochralski method. Binary semiconducting compounds can also be formed of atoms from groups III-V or II-VI. Solutions can also be produced either of group IV elements (Si-C and Si-Ge) or of binary compounds. For example GaAs, InAs, GaSb and InSb are each binary III-V compounds that can form the quaternary alloy GaInSbAs. Because of the wide range of possible compositions, compound semiconductors offer a very wide range of properties that cannot be achieved with silicon or germanium.

2.1.1 Zincblende Crystal Structure

Most semiconductors are crystalline, forming either a zincblende or diamond cubic crystal structure. Each of these structures consists of two interpenetrating face-centered cubic lattices offset by one quarter of the cubic diagonal vector. In binary III-V and II-VI compounds, each sub-lattice consists of atoms from one group. In the diamond structure, all atoms are from group IV. Each atom in this structure rests at the centre of a regular tetrahedron formed by its four nearest neighbours.

In most growth processes, zincblende materials are grown with the longitudinal axis aligned along a <100> or <111> crystallographic direction as shown in Figure 2.2. When a <111> direction is aligned aligned vertically, as in the growth of CdZnTe, the (111)A and (111)B planes form horizontal bands. Because the A and B planes appear in pairs, a crystal of zincblende material cut with (111) faces will have an A face and a B face. In CdZnTe, the A face consists of cadmium and zinc atoms, and the B face consists of tellurium atoms. The two faces have different chemistry and respond differently to chemical etchants.

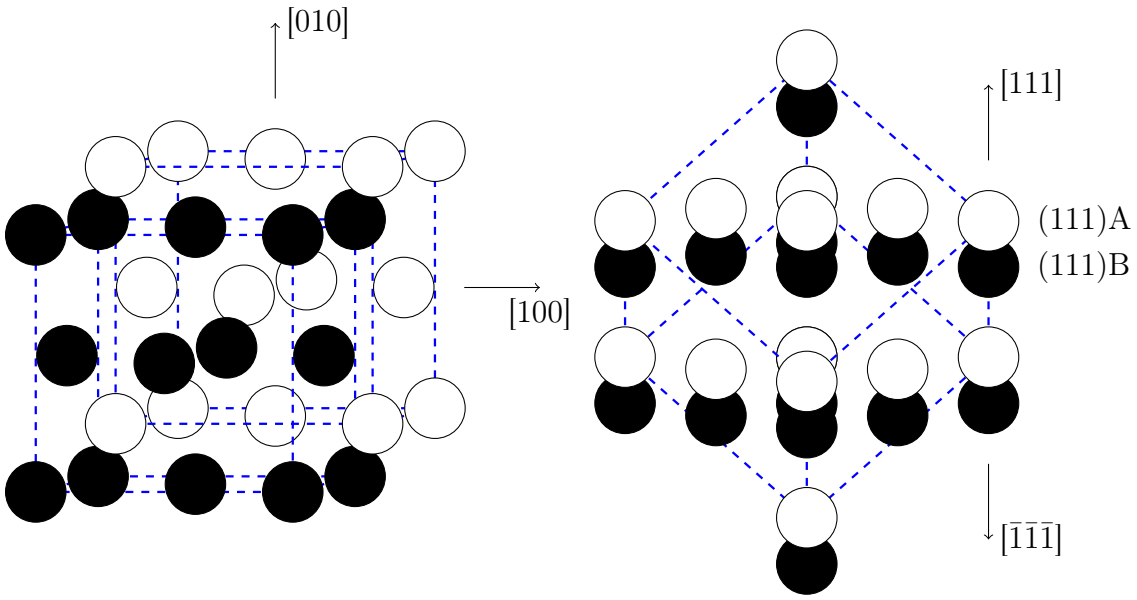

Figure 2.2: The zincblende crystal structure with interpenetrating A and B sublattices. At right, the structure is oriented for growth with the (111)A plane facing upward.

2.1.2 CdTe and CdZnTe

Cadmuim telluride is a II-VI compound with a wide, direct band gap of 1.47 eV. Because of its large atomic number and direct band gap, CdTe has relatively high absorption efficiency and has found wide application in thin-film photovoltaic cells [2]. CdTe transmits infrared light, and it is therefore also used for infrared optics and windows. Large single crystals of CdTe (and CdZnTe) are needed for two applications: first as substrates for the epitaxial growth of infrared detectors from HgCdTe, and second for the production of high-sensitivity x- and γ-ray detectors [4, 5].

The processes studied in this work are designed to produce material for radiation detectors, and the desired material properties are driven by the detectors' principle of operation, which is illustrated in Figure 2.3. An incident photon interacts with the material, generating a large number of charge carriers which are collected and counted. The average energy to produce a charge carrier is a known material property, so the photon's energy can be determined by measuring the number of charge carriers it created. The energy resolution of a detector therefore depends on the ability to accurately measure the number of charge carriers produced by each photon.

The electrical properties of CdTe make it an excellent material for radiation detectors. Apart from its high absorbtion efficiency, its large band gap gives it high

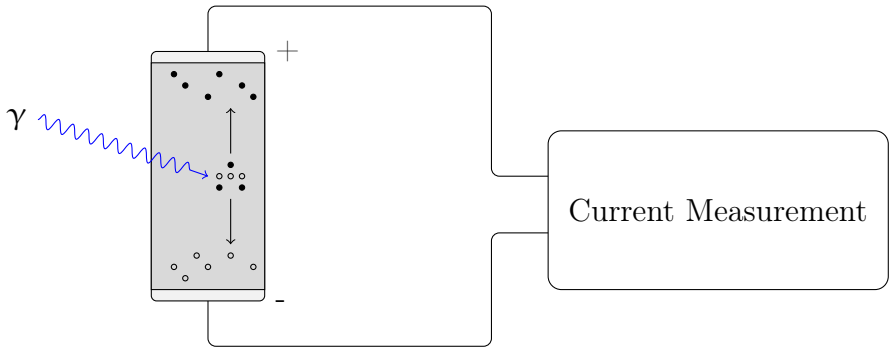

Figure 2.3: Operation of a x- or γ-ray detector

intrinsic resistivity which leads to lower leakage current and less noise in detectors. This property allows CdTe detectors to be used at room temperature as opposed to silicon or germanium devices which require cryogenic cooling. CdTe also has high charge mobility so that carriers can be collected quickly, and long lifetime so that carriers do not recombine before they can be collected. Taken together, these properties make CdTe a very desirable detector material if it can be produced economically.

Despite its high intrinsic resistivity, CdTe grown for detectors risks having much lower resistivity because of extrinsic charge carriers. High resistivity material is achieved first by reducing the concentrations of impurities, which generally act as acceptors [6]. Bavenstov et al recommend that in order to achieve intrinsic resistivities, impurities would need to be reduced below the order of $10^8\,\mathrm{cm}^{-3}$, but this is not currently achieved consistently in practice.

In addition to impurities, deviation from exact 50% stoichiometry creates extrinsic charge carriers that reduce CdTe's resistivity and create leakage current in detectors. The defects in CdTe that lead to these carriers are cadmium vacancies or interstitial atoms leading respectively to p-type or n-type carriers [7]. This narrow solubility region is expanded for emphasis in the centre of Figure 2.4. The solidus lines that define the the existence region extend as far as 10^{-4} mol% at high temperature, but they return at lower temperatures to much smaller deviations from equal stoichiometry. This retrograde solid solubility means that CdTe formed at high temperature may contain dissolved Cd or Te, which will precipitate at lower temperatures leading to point defects and extrinsic charge carriers. Retrograde solid solubility is a significant problem for CdTe grown from the melt. The resulting defects and precipitates significantly reduce its resistivity and can even lead to polycrystallinity. Great care is therefore taken to maintain a precise Cd-rich growth environment, and slow

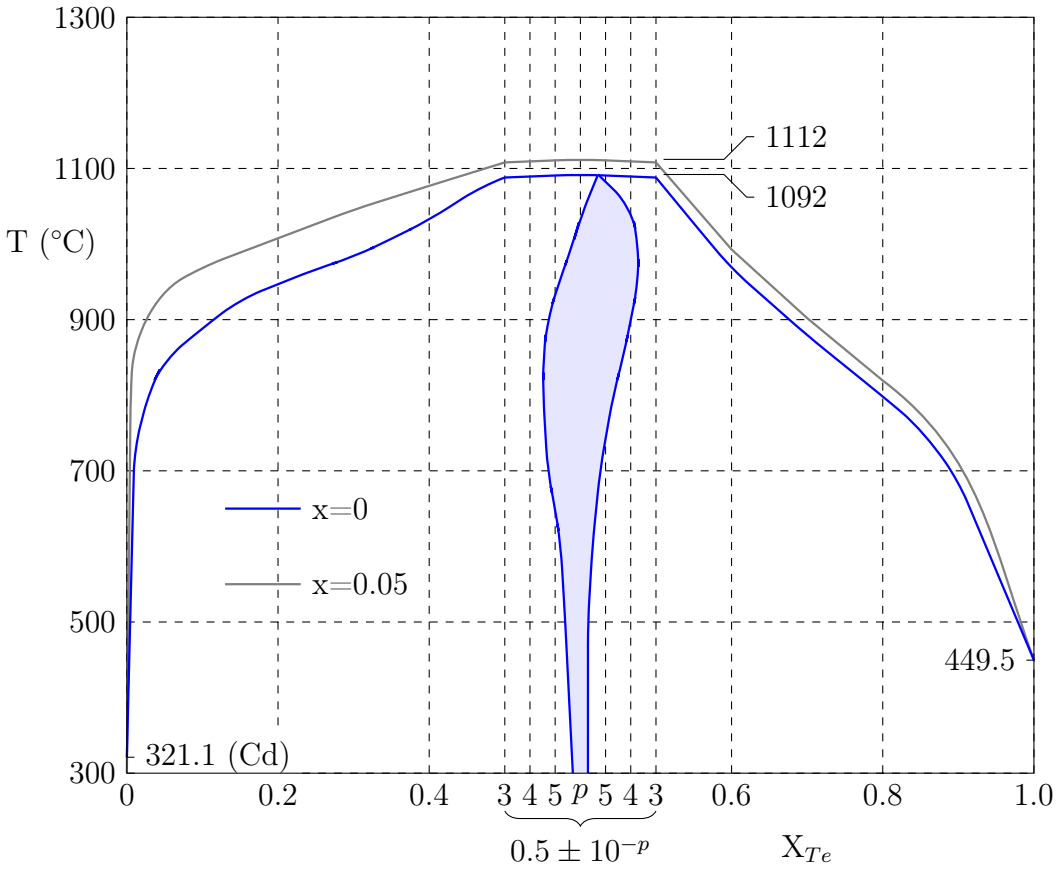

Figure 2.4: Equilibrium phase diagram of $Cd_{1-x}Zn_xTe$ for the values of x used in this project. The existence region of 0.5 ± 10^{-3} is expanded in log scale for clarity. Data from [9, 10, 11]

post-growth annealing processes are used to correct the final composition [8]. At temperatures near 700 °C, the solubility of Te is two orders of magnitude lower than at temperatures near the melting point. Lower temperature solution-based growth methods therefore avoid many of the defects associated with retrograde solubility.

In practice, impurities and stoichiometric deviation cannot be eliminated and lead to p-type material. CdTe is therefore often doped with chlorine, which acts as a donor to compensate for the extrinsic holes and achieve higher resistivities.

When Zn is added to CdTe, the bandgap of the resulting material increases. This allows high resistivity and room temperature detector operation to be achieved without additional doping with chlorine. The smaller Zn atoms also reduce the material's atomic spacing and increase its hardness. Unfortunately, the different atom size also creates strain in the crystal and makes it more prone to the formation of defects and

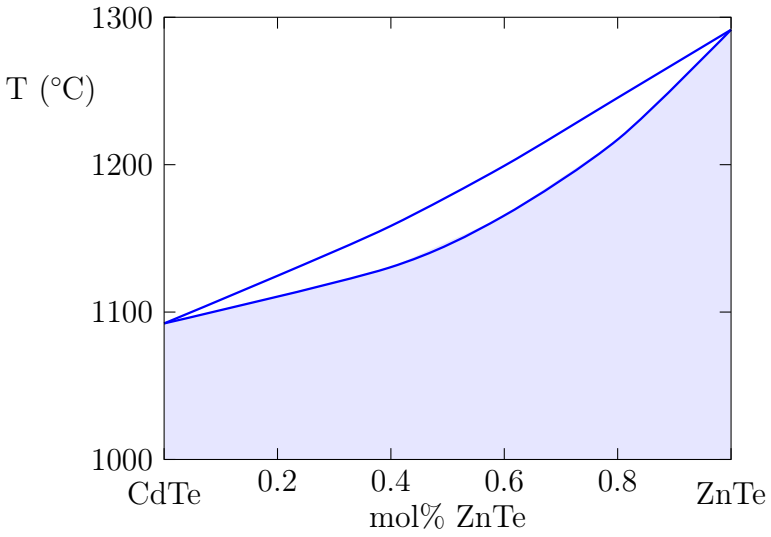

Figure 2.5: Peudobinary phase diagram for the CdTe-ZnTe system, plotted with data from Steininger [9]

more sensitive to strain induced during production.

CdZnTe is an example of a tunable compound semiconductor. CdTe and ZnTe are each binary II-VI semiconductors with fixed properties and compositions; however, they form a pseudobinary alloy system with continuous variation of material properties. In particular, the lattice parameter and band gap can be selected for producing substrates or detectors by controlling the material composition. $Cd_{.96}Zn_{.04}Te$ is lattice-matched for producing CdHgTe infrared detectors, while $Cd_{.9}Zn_{.1}Te$ is used for high energy radiation detectors. In this work, $Cd_{.95}Zn_{.05}Te$ was grown because this composition was readily available.

The CdTe-ZnTe pseudobinary system exhibits a large difference between the liquidus and solidus compositions, as shown on the equilibrium phase diagram in Figure 2.5. This has important implications for the production of ternary crystals. When a liquid CdTe-ZnTe mixture solidifies, the ZnTe is incorporated preferentially into the solid, depleting the Zn content of the liquid. If the melt is not replenished, this results in a composition gradient in the resulting solid which in turn creates non-homogeneous material properties.

Apart from the variation of electrical properties with composition, telluride compounds have other properties that make them difficult to produce in large quantities. The thermal properties of CdTe and CdZnTe are compared to other semiconductors in Table 2.1. Like the electrical resistivity, the thermal resistivity of the wide band

Table 2.1: Selected solid and liquid properties for several semiconductors [12, 7]

Property	CdTe	GaAs	Si	Units
Thermal Conductivity (l)	1	18	54	$Wm^{-1}\ K^{-1}$
Thermal Diffusivity (l)	0.49	7.26	21.3	$\mu m^2 s^{-1}$
Prandlt Number (l)	0.413	.068	.013	
Critical resolved shear stress (s)	0.2	0.7	3.6	MPa

gap II-VI compounds is much larger than either elements or III-V materials with narrower band gaps. The low thermal conductivity also leads to low diffusivity and large Prandtl numbers. These complicate production methods for two reasons. Heat cannot be easily removed from the growth environment, so temperature conditions are difficult to control at the point of growth. Energy transport in liquid melts tends to include significant convection as well as conduction, and the associated flow structures can destabilize growth interfaces.

In addition to poor energy transport, the critical resolved shear stress (CRSS) is very low (300 kPa). Dislocation defects can therefore be generated easily by thermal stress during growth. The resulting need to maintain small radial temperature gradients further complicates the challenge of managing energy transport in the growth environment. Finally, CdTe is highly ionic, and therefore has a very low stacking fault energy which makes it very susceptible to twinning. Twin planes with (111) orientation are found in virtually all CdTe and CdZnTe crystals [7]. High dislocation densities and twinning affect both device efficiency and yield of useful material.

CdTe and CdZnTe have very desirable properties for room-temperature radiation detectors, but their thermal properties and the need for precise composition control complicates the processes used to produce them. Gradient freezing produces non-homogeneous, non-stoichiometric material. The travelling heater method yields stoichiometric and homogeneous material, but at the expense of very slow and expensive production. This work aims to combine elements of both methods to achieve telluride compounds with uniform properties at lower cost.

2.2 Growth Techniques

The majority of semiconducting devices are manufactured from large wafers sliced from bulk crystals of Si, and to a lesser extent Ge and GaAs. These large ingots are

overwhelmingly produced by the Czochralski method of pulling from the melt. Where Czochralski growth is not possible, bulk crystals can also be grown by a wide range of less efficient methods. These include growth from liquid melts and solutions, from vapours, or in the solid state through heat treatment. Solid and vapour phase growth are extremely slow, and apart from epitaxy the vast majority of growth processes are based on solidification from melts or solutions.

Czochralski growth was investigated for CdTe in the 1970s and 1980s [13]. In the Czochralski processes, a narrow seed crystal is dipped into a large bath of liquid and withdrawn slowly. The rate of withdrawal is controlled to maintain a steady crystal diameter throughout the growth process. Several properties of CdTe and CdZnTe make this impractical, however. First, the high vapour pressure of Cd over molten CdTe necessitates encapsulation of the melt with a layer of liquid B_2O_3 compressed by an inert high-pressure (75 atm) atmosphere. Although liquid encapsulated Czochralski (LEC) growth is used routinely to grow III-V compounds, it has not been successful with II-VI materials. These materials have lower CRSS and are more much more prone to high dislocation density, twinning and polycrystalinity due to thermal strain or large pressures. Most importantly, however, successful LEC growth depends on good control of the thermal conditions at the growth interface. The much poorer heat transport in II-VI materials makes sufficient cooling of the crystal impossible to achieve, especially without inducing large thermal strains.

The failure of LEC has required that tellurides continue to be grown by much slower gradient freezing and travelling solvent methods. Both of these were employed in this work, and the experimental details of each method will be described in Chapter 4. They are described briefly here in order to explain why and how they are used to produce high quality CdTe and CdZnTe, and to provide background to the numerical simulations described in Chapter 6.

2.2.1 Vertical Gradient Freezing

Gradient freezing is the most common production method for CdZnTe. It consists of melting the compound in a quartz or graphite ampoule, and solidifying it by cooling under a temperature gradient. When the cooling is accomplished by translating the sample or heater, the method is called Bridgman growth. When the experiment is stationary with the temperature field changed electronically, the technique is simply called gradient freezing. Vertical gradient freezing (VGF) was used in this work to

produce seed crystals for later growth experiments.

The process for a VGF growth experiment is as follows: precursor metals or precompounded, polycrystalline material is placed in a quartz or graphite crucible and sealed in a quartz ampoule under vacuum. The system is heated above the compound's melting temperature, and the melt may be further superheated at least 10 °C above its melting point to destroy the molecular tetrahedra, rings and chains that appear to remain in CdTe upon melting [7]. A temperature gradient is established to stabilize the growth interface, and growth proceeds by lowering the temperature. When the crystal is fully solid, it is cooled slowly to room temperature, removed and processed.

Atmosphere control is critical in order to achieve high-resistivity material using VGF. The congruent melting point in the CdTe phase diagram occurs under Te-rich conditions, as can be seen in the phase diagram in Figure 2.4. In order to crystallize highly stoichiometric solid, slightly cadmium-rich conditions must be maintained in the melt. This lowers the equilibrium temperature slightly to coincide with the crossing of the Cd-rich solidus line with the stoichiometric composition. To maintain the cadmium content of the melt, a temperature-controlled cadmium reservoir is used to control the Cd partial pressure in the ampoule's atmosphere.

Like LEC, VGF produces CdZnTe crystals with varying composition. Smaller zinc atoms are incorporated preferentially into the solid, which depletes the zinc-content of the melt. Depending on the shape of the growth interface, the compositon of the resulting ingot may vary radially as well as axially. If a narrow composition range is required for a specific application such as lattice-matched substrates, only a small portion of the ingot might have the desired properties.

2.2.2 Travelling Heater Method

The THM has become a leading method for producing high quality CdZnTe crystals for use in room temperature radiation detectors, and it has been the focus of intense research in the past two decades [14]. Crystal growth by THM seeks to overcome many of the inherent problems of VGF through the use of a travelling solvent zone to dissolve rather than melt the source material. The principal advantages of THM are its lower process temperature, the ability to produce homogeneous crystals, and the use of seed crystals to produce monocrystalline ingots. Its disadvantages are the high cost of large seed crystals, its very slow growth rate, and the presence of tellurium

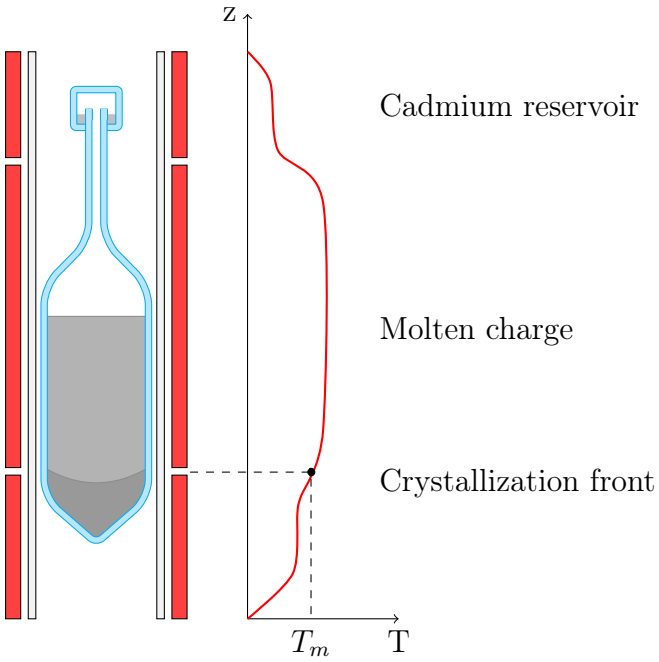

Figure 2.6: Vertical gradient freezing or Bridgman growth configuration

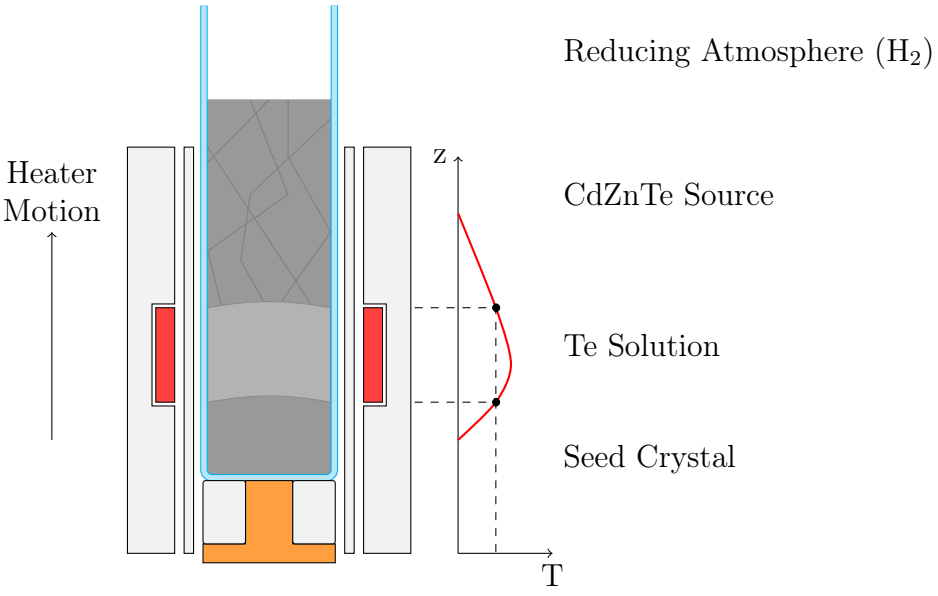

Figure 2.7: Growth configuration for the travelling heater method

inclusions in most grown material.

To produce crystals by THM, a large seed crystal is secured in the bottom of a quartz ampoule, which is usually coated with graphite to prevent sticking. A metallic mixture is added to form the solution zone, and then source material is added at the top consisting of either polycrystalline compound or precursor metals. The resulting configuration can be seen in Figure 2.7. The ampoule is purged and usually sealed with a low pressure reducing atmosphere. The solution zone is melted by a narrow heater, and growth proceeds by translating either the ampoule or the heater. When all of the source material has been dissolved by the working solution, growth is complete and the crystal is cooled to room temperature and removed from the ampoule.

The key characteristic that defines THM is the travelling working solution. In the growth of tellurides, Te is the most common solvent used; however in principle any liquid may be used in which CdTe is sufficiently soluble. Cadmium solvent zones have been reported, but Te is preferable. On reason for this is the width of the existence region near 50% stoichiometry. For temperatures below 800 °C, the solidus can be seen in Figure 2.4 to deviate from 50% less on the Te-rich side than on the Cd-rich side. Tellurium solutions can therefore be expected to grow material with more precise stoichiometry. Moreover, free Te is much less toxic than Cd, and it is less volatile which reduces evaporation of the solution.

The use of a solvent lowers the growth temperature of THM from the CdTe melting temperature of 1092 °C down to 700 °C - 900 °C. This has many advantages. Lower temperatures do not degrade the quartz growth ampoules and reduce contamination. The narrower solidus region leads to more precise stoichiometry than is typically achievable with melt growth. The lower temperatures should also mean lower thermal stresses and therefore fewer dislocations and defects in the grown material, although this may not be the case in practice.

The other major advantage of growth from a saturated solution is control of the composition of the product crystal. Once the solution has reached saturation, the dissolution of further source material causes material with the same composition to deposit at the growth interface. Because uniform polycrystalline source material is easily achieved by rapid quenching, THM can be used to produce crystals of uniform composition. A related advantage is also that impurities that do not reach their saturation limits in the solution may be rejected from the interface and carried out with the solution itself. This purification effect is a welcome contrast to melt processes where impurities have nowhere to go other than the last-to-freeze region of the ingot.

THM presents several challenges however, both in its practical application and in theoretical studies. In melt growth, solidification is governed by energy transport. Growth rates are slower in CdTe than in other materials that conduct heat more readily, but they are still relatively fast, on the order of several millimetres per hour. By contrast, growth in THM is driven by both heat and mass transport in the saturated solution zone. Solute transport from the dissolution interface to the growth interface limits growth rates to less than 10 mm per day.

Another major drawback to THM is the requirement for large seed crystals. Seeds are typically cylinders with the same diameter as the target crystal product and thickness up to a third of the overall experimental height. Such crystals are difficult to obtain and very expensive. Indeed, needing seed crystals comparable to the desired product is a drawback nearly unique to THM. The goal of the current work is to investigate whether THM growth is achievable using smaller diameter seeds or in an unseeded configuration such as are commonly used in VGF growth.

Convection, Ampoule Rotation and Applied Magnetic Fields

The position, morphology and stability of the solid-liquid interfaces in THM are driven by more complicated processes than in melt growth. In melt growth, the interfaces may be reasonably assumed to be isothermal and their position is determined from the energy equation and the material melting temperature. In THM, this is only true if the solution zone has a uniform composition. In general, even assuming local equilibrium the equilibrium phase diagram allows variation of both temperature and liquid composition across each interface. Moreover, small variations in temperature lead to significant changes in solubility and therefore rapid growth or dissolution unless the normal temperature gradient is large ($1 - 10\,\mathrm{K/mm}$). Such large temperature gradients, however, tend to induce strong convection in the solution zone. Rapid dissolution also changes the local solution composition producing a strong body force, strong convection and transient variations of both temperature and composition at the interface. The transport regime governing THM growth processes is therefore more complicated and more difficult to model or control than comparable melt processes. The inability to achieve favourable transport conditions is one factor that has limited both the size of THM product crystals and the rate at which they can be produced.

Because of the complicating impact of natural convection in THM systems, sev-

eral techniques have been developed aimed at either enhancing or disrupting flow in the liquid zone. Accelerated ampoule rotation (AAR) has been applied with success by several groups working with CdTe and CdZnTe from 1975 to the present day [15, 16, 14]. This work will be described in more detail in Section 6.5.2. AAR disrupts existing natural convection in cylindrical systems and replaces it with stronger but more controllable forced convection. Another approach to suppressing convection is to reduce the strength of the driving body force either through experimentation in microgravity environments or through the use of a static magnetic field. More commonly, however, a rotating magnetic field (RMF) is applied. Like AAR, RMF induces azimuthal flows that disrupt natural convection cells and replace them with controllable forced convection. Because the resulting body force is relatively weak, RMF is usually employed when natural convection is weaker such as in gallium solution zones or in microgravity experiments, but it has been studied numerically for ground-based growth as well [17, 18, 19]. Neither AAR nor RMF was used in the present study apart from slow rotation of the final growth experiments which was intended only to promote axisymmetry.

Current State of the Art

THM growth of CdTe at 50 mm diameter or larger is now routine in industry with crystals up to 100 mm diameter reported by Acrorad using AAR [20]. Industrial CdZnTe growth at up to 100 mm diameter is also used at Redlen Technologies [21, 22]. These THM processes are proprietary with their details, particularly the control of convection in the liquid zone, kept as trade secrets. Both of these technologies are known to use large seed crystals which reduces the change in thermal conditions over the course of a growth experiment. Outward THM growth from small seeds has not been reported.

Chapter 3

Motivation for CdZnTe THM Growth Using Small Seeds

There are many reasons why THM should be a leading method to produce large CdZnTe crystals. In particular, THM produces oriented ingots with uniform composition. In contrast, melt growth techniques such as VGF produce ingots with random orientation and variable composition, within which only a fraction of the material has the necessary composition and from which large grains need to be identified and mined. A large crystal grown by THM need only be cut into wafers.

Unfortunately THM growth is slow and expensive, and a principal source of the cost is the need for large, oriented seeds. With existing technology, seeds must be produced either through larger VGF experiments or by cutting existing crystals already produced by THM. The ability to use small seed crystals to instigate THM growth would represent a significant cost savings.

A previous experimental study demonstrated that THM is possible from small seed crystals in the GaSb system. That work is described below. The current study attempts to reproduce this success with CdZnTe, which is more technically relevant and more difficult to produce.

The goals of this study were to:

1. Develop the supporting technologies required to grow CdZnTe by THM.
2. Demonstrate the THM growth of CdZnTe using small seed crystals.
3. Improve understanding of the phenomena within THM growth systems by measuring transport properties and by simulating experiments numerically.

Table 3.1: Summary of GaSb THM growth experiments

Experiment	Seed Dia.	Rate	Magnetic Field	Result
25 mm diameter				
GaSb12	25 mm	2 mm/d	-	Single crystal
GaSb13	25 mm	2 mm/d	0.8 mT, 100 Hz	Single crystal
GaSb16, GaSb18	10 mm	2 mm/d	-	Single crystals
GaSb19, GaSb20	10 mm	5 mm/d	-	Polycrystalline
GaSb21, GaSb22	10 mm	5 mm/d	0.8 mT, 75 Hz	Polycrystalline
GaSb23, GaSb24	10 mm	5 mm/d	1.94 mT, 50 Hz	Single crystals
50 mm diameter				
GaSb25	25 mm	2 mm/d	-	Single crystal

3.1 THM Experiments in GaSb

GaSb is similar to CdTe in many ways, being a compound semiconductor with zincblende crystal structure. It is, however, easier to produce by THM or by Czochralski growth due in part to its higher thermal conductivity. THM growth of GaSb was a part of the author's M.A.Sc thesis, which focused on the effect of RMF on the growth process. Four cylindrical crystals were grown in that work which showed no observable effect due to the addition of the fields [23]. Subsequent experiments showed, however, that 25 mm samples could be produced by growing from 10 mm seed crystals. Some tapered growth was also demonstrated in a 50 mm crystal grown on a 25 mm seed as seen in Figure 3.1. This tapered growth was published prior to the current study [24].

The tapered growth of GaSb required a significant development process and improvements to the THM equipment, but it was simpler and more forgiving than the growth of CdTe or CdZnTe. Gallium melts at only 30 °C, which simplified loading and casting procedures, and GaSb seed crystals were core drilled from commercially available Czochralski-grown oriented slabs using standard diamond cutting tools. Gallium is much less prone to convection than tellurium, having a Prandtl number one tenth as large [23], and the lower process temperature for GaSb THM meant more controlled, consistent growth conditions. These effects made it much simpler to maintain favourable conditions at the growth interface for GaSb experiments than in the subsequent CdTe or CdZnTe experiments.

Some of the key results from the GaSb THM growth trial are shown in Figure 3.1. After a long development period with straight and tapered THM growth experiments, GaSb18 demonstrated successful growth out from a 10 mm diameter seed to a final

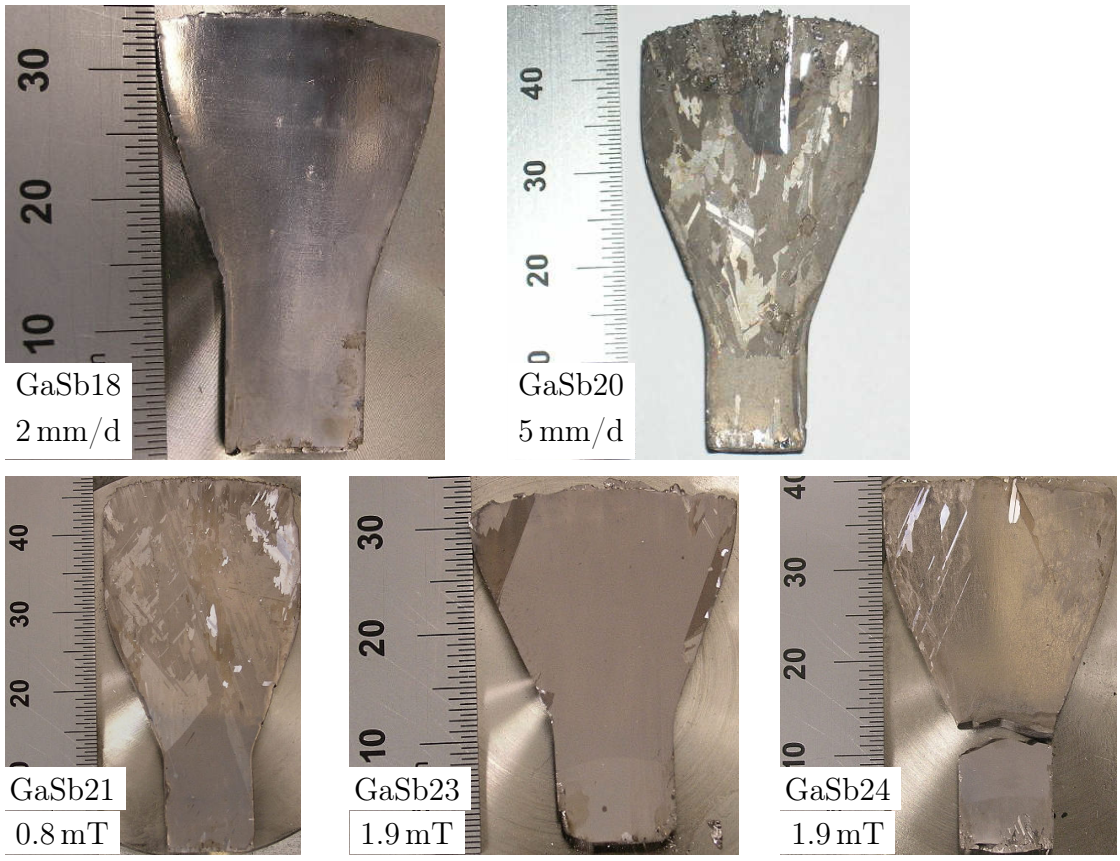

Figure 3.1: Top row: Tapered GaSb growth was successful at 2 mm/d but not at 5 mm/d. Bottom row: Under increasingly strong RMF, growth improved with fewer and more structured grains produced even at 5 mm/d [24].

diameter of 25 mm with a growth rate of 2 mm/d. Attempts to grow at 5 mm/d were initially unsuccessful until GaSb23 and GaSb24 in which single crystals were produced with occasional secondary grains by growing at 5 mm/d under an applied rotating field of 2 mT,50 Hz. The results were not conclusive enough to claim an effect from the magnetic field, but they did show that single crystals can be grown by THM using smaller diameter seeds, at least in GaSb.

GaSb25 was the first growth experiment using a new, larger THM furnace. It was an attempt to grow a 50 mm diameter crystal from a 25 mm diameter seed, and it showed modest promise. Growth proceeded for 15 mm at 2 mm/d before accelerating to 5 mm/d and then stopping abruptly. After cutting and etching, a line of etch pits appears to trace the shape of the growth interface at the moment of the increase in growth velocity. GaSb25 can be seen in Figure 3.2. The convex shape of the interface matches those achieved in the GaSb experiments at smaller diameter. Growth at

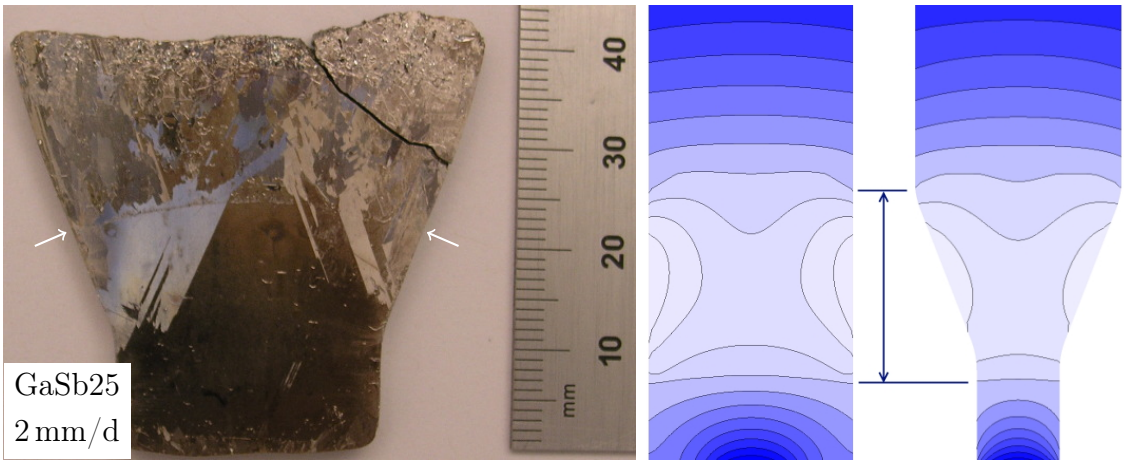

Figure 3.2: Etch pits in GaSb25 appear to show the state of the growth interface when the translation rate was increased from 2 mm/d to 5 mm/d. Right: Preliminary simulations suggested that the thermal conditions in the tapered growth system are similar to those in a straight ampoule [24].

2 mm/d showed largely single crystal growth with several twin defects. The appearance of the material grown in this region showed up again much later in the large diameter CdTe grown in the late stages of this study. After the growth rate increased to 5 mm/d, the material became highly polycrystalline.

The GaSb growth study demonstrated tapered growth by THM to 25 mm diameter beginning with a 10 mm diameter seed crystal and it showed modest success when a 25 mm diameter seed was grown out in a 50 mm diameter growth system. Moreover, applying RMF appeared to improve the growth conditions and increase the maximum growth rate from 2 mm/d to 5 mm/d. Because of the ease of handling and the well-understood chemical properties of GaSb, etch pits were revealed in GaSb18 and GaSb25 that showed a favourable interface shape and good growth conditions. This success in the GaSb system was good motivation therefore to extend the work to CdZnTe growth.

Although it was useful to study the THM process and demonstrate outward growth from a small seed crystal, GaSb is not a commercially important material for THM because it is readily grown by the much more economical Czochralski method. In fact, the material properties that make Czochralski growth possible also make GaSb much easier to grow by THM than CdZnTe. The very high electrical resistivity of CdTe and CdZnTe, although very helpful for the performance of detectors, is associated with a much lower thermal conductivity compared to GaSb. In the context

Table 3.2: Dimensionless quantities for gallium and tellurium THM solutions

Number	Symbol	Definition	Gallium	Tellurium	
			25 mm	25 mm	65 mm
Prandtl Number	Pr	ν/α	.004	.06	.06
Thermal Grashof	Gr_T	$g\beta_T \Delta T H^3/\nu^2$	10^7	10^7	10^8
Solutal Grashof	Gr_C	$g\beta_C \Delta C H^3/\nu^2$	10^3	10^6	10^7
Thermal Rayleigh	Ra_T	$g\beta_T \Delta T H^3/\alpha\nu$	10^5	10^6	10^9
Solutal Rayleigh	Ra_C	$g\beta_C \Delta C H^3/D\nu$	10^4	10^5	10^6
Reynolds Number	Re	$v_{max} H/\nu$	10^1	10^2	10^3

of THM, this means that temperature gradients are larger in the liquid zone and thermal convection is stronger. This difference is demonstrated by the characteristic dimensionless numbers listed in Table 3.2. The Prandtl number, for example, is ten times larger in CdTe than in GaSb. At the same time, the body force that can be generated by a magnetic field B with angular velocity ω is proportional to the material's electrical conductivity σ_E.

$$f = \frac{1}{2}\sigma_E B^2 \omega r \tag{3.1}$$

In the CdTe system subjected to the same temperature profile and applied magnetic fields, we should therefore expect thermal convection that is 10 times stronger and an electromagnetic body force that is 10 times weaker than in a similar GaSb system. In THM of GaSb, RMF serves to add mixing to a solution zone with relatively little convection. In CdTe and CdZnTe systems, if RMF has any effect it is to disrupt the strong convection that already exists. Because the magnetic force is expected to be much weaker and because the telluride system already has strong convection, the investigation of RMF was not a high priority for a study of CdTe or CdZnTe THM growth.

Although CdTe and CdZnTe are more difficult to produce than GaSb by THM the tremendous cost of large seed crystals makes the extension of tapered growth to these new materials very valuable if it can be demonstrated reliably.

Chapter 4

Supporting Technology

Growing single crystals by THM requires several supporting technologies to provide appropriate seed and source material and to handle and process the resulting ingots. In addition to the central THM study in this work, supporting studies were carried out. First, the material handling procedures used in the GaSb study needed to be adapted for CdTe and CdZnTe, which were much more difficult to cut and to etch. Zone refining of tellurium and cadmium precursors has also been investigated, which gave insight into the transport phenomena in liquid tellurium. The synthesis of CdTe and CdZnTe by rapid THM was investigated, and seed crystals were grown by VGF. Finally, the diffusion rates of CdTe and ZnTe were measured in liquid tellurium in order to improve understanding of the transport processes in the THM system. These smaller studies supported the THM growth study which was the primary focus of this work.

4.1 General Experimental Considerations

The materials and processes developed for this study were used in the supporting work as well as the THM growth study. They are presented once below as a reference for all of the experimental studies that follow.

4.1.1 Materials and Preparation

Tellurium, CdTe, CdZnTe and ZnTe for this research were provided by 5N Plus Inc. Compounds were prepared by THM with 6N (99.9999%) purity and crushed and screened to a uniform particle size. The particles were packaged under vacuum by

5N Plus and unsealed in a cleanroom immediately prior to loading into experiments. Tellurium with 6N and 5N5 (99.9995%) purity was provided in shotted form with 4 mm particles.

Several etch recipes were used to clean, prepare and analyze the II-VI materials and glassware.

Aqua regia (3 HCl : 1 HNO_3) was used to etch glassware prior to experiments. The acid was mixed in the ampoule and allowed to react for four to eight hours. Aqua regia was also used occasionally to rapidly dissolve or etch CdTe. With different proportions (1 HCl : 1 HNO_3 : 2 H_2O), aqua regia chemically polishes CdTe and CdZnTe[25]. Occasionally, equilateral etch pits were observed on uneven (111)A surfaces etched with a dilution of the latter etch.

E-Ag Solution (4 g $K_2Cr_2O_7$: 10 ml HNO_3 : 20 ml H_2O : 1.5 mg $AgNO_3$) produces pits on (111) surfaces[25]. Without the $AgNO_3$, the E solution rapidly polishes (111) surfaces, and this etch was used to reduce the diameter of samples. The addition of Ag^+ slows the reaction and produces tetrahedral pits on the (111)A surface and flat-bottomed equilateral pits on the (111)B surface.

Modified Everson etch (1 HF : 3 HNO_3 : 4 2%$AgNO_3$) was used to rapidly etch polished surfaces to reveal grain structure. It also produced etch pits in (111)B faces. The original Everson etch (1 HF : 4 HNO_3 : 25 Lactic Acid) was not used in these projects[26].

Nakagawa etch (3 HF : 2 H_2O_2 : 2H_2O) was used occasionally to produce etch pits on (111)A faces and to reveal grain structure[27].

The preparation of seed crystals required identification of (111)A and (111)B faces before and after cutting the seeds. This was usually accomplished by mechanical and chemical polishing followed by etching with E-Ag solution and microscopic inspection. Figure 4.1 shows the characteristic equilateral etch pits generated on (111)A surfaces by the various recipes used in this work.

Fused-silica quartz ampoules were used for all experiments. Ampoules for VGF and dissolution experiments used no surface coatings, while later THM experiments used a pyrolized graphite coating applied by Sandfire Scientific Ltd. Prior to each experiment, uncoated glassware was etched for four hours with aqua regia, rinsed thoroughly and soaked in deionized water overnight. Prior to loading coated and

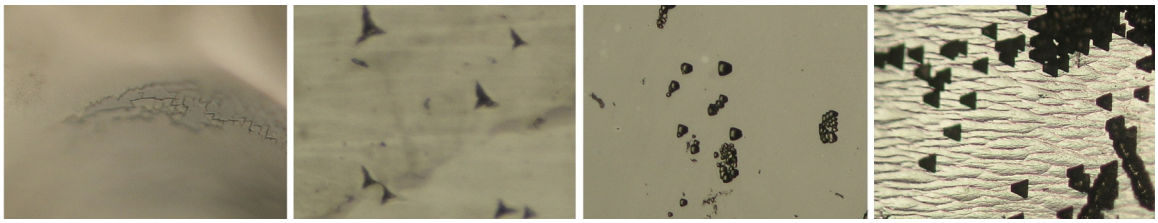

Figure 4.1: Left to right: pits on (111)A surfaces of CdTe65-7 etched with dilute aqua regia, with E-Ag, with E followed by Nakagawa, and with modified Everson followed by Nakagawa etch.

uncoated ampoules were rinsed with methanol and dried overnight or baked under vacuum to remove residual water in the quartz.

4.1.2 Cutting tools

Four tools were used to process CdTe and CdZnTe samples in this work. Small, fast cuts were made using an IsoMet disk saw from Beuhler with fine diamond grit. This was used, for example, to slice dissolution experiments along their length. All diamond tools, however, including the ones used successfully in preliminary GaSb experiments, were found to chip and crack CdTe badly.

Large ingots were sliced on a tape saw using a slurry of 400-grit boron carbide suspended in a mixture of water and glycerine. The tape saw is large enough to accommodate boules up to 65 mm diamater, such as the one shown in Figure 4.2, but it requires frequent changes of slurry and extremely slow feed rates (5 mm/h) to achieve flat cuts.

The wire saw, Model 850 from South Bay Technology, was much faster than the tape saw but useful only for cuts smaller than 50 mm. The wire blades were prone to breakage and had to be replaced several times during the cutting of most ingots. Saw components including bearings and spindles were also replaced several times during the project due to infiltration of the cutting slurry. The guide grooves on the saw's spindles also required frequent re-conditionning to reduce wire breakage.

Core drilling of the cylindrical seeds for THM experiments was problematic. Seeds for preliminary GaSb experiments were obtained successfully using diamond grit core drills mounted in a drill press. These tools invariably shattered CdTe samples. A new system was therefore constructed to improve control of the drilling procedure and the diamond tools were replaced with a boron carbide slurry. Brass and steel cutters were fabricated to allow core drilling of seeds up to 25 mm tall. A cutting

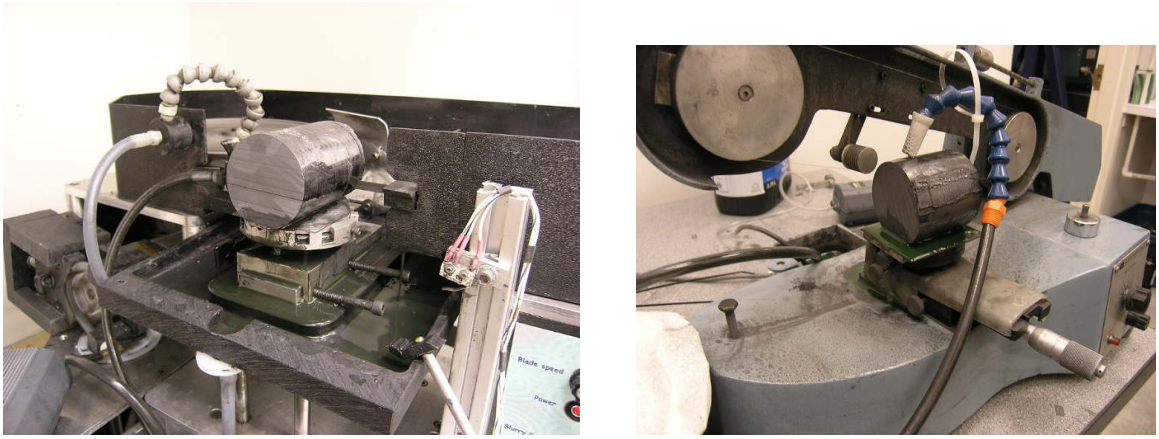

Figure 4.2: Tape and wire slurry saws used to cut CdTe and CdZnTe samples

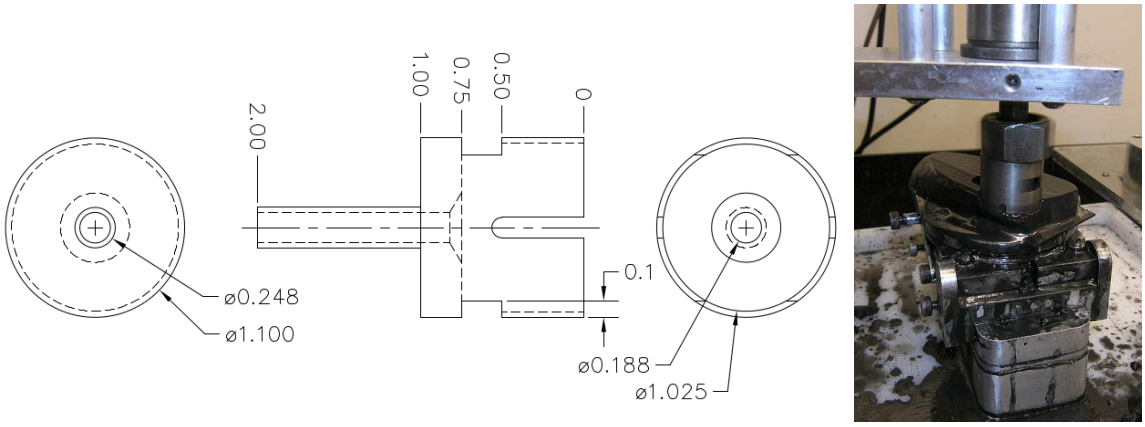

Figure 4.3: Core drilling of a 25 mm seed, and shop drawing of a cutting tool (Dimensions in inches)

tool for 25 mm seeds is shown in Figure 4.3. The shaft is designed to slide within a hollow drive axle and to slip as necessary to prevent damage to the part. Torque is maintained by friction within the axle or by a silicone o-ring placed between the axle and the top surface of the cutting tool. The tool also has slots to allow slurry to be sprayed onto the top of the seed during cutting and to move slurry to and from the cutting edge. The resulting process was very slow, requiring frequent attention for up to ten hours to produce one seed. It does, however, eliminate shattering of the seed material and gives smooth cutting faces without chipping.

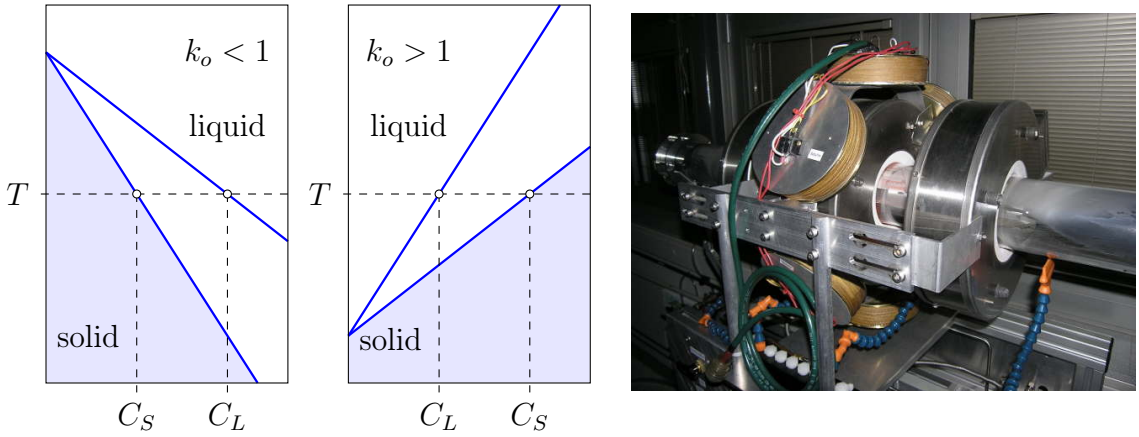

Figure 4.4: The different liquidus and solidus concentrations at at the equilibrium interface temperature results in preferential exclusion or incorporation of solute into the advancing solid. Right: The zone refining test apparatus passes three zones at a time through an ingot with RMF applied to the centre zone.

4.2 Zone Purification of Source Materials

The first experimental study related to this work was in the zone refining of tellurium and cadmium precursor materials. This work was carried out concurrent with the THM studies in GaSb and CdZnTe.

All crystal growth processes and semiconductor applications require very pure starting materials. In the case of CdZnTe crystal growth, the elemental precursors are purified first by distillation and then by zone refining. Zone refining consists of melting a short length of a solid ingot and then passing molten zones from one end of the ingot to the other. At the solidification front of each molten zone, impurities are either included or rejected preferentially from the forming solid. Repeated zone passes therefore carry some impurities to the tail of the ingot while causing others to migrate toward the nose. After a sufficient number of zone passes, regions of the ingot are pure enough for use as feed material for crystal growth processes.

The effectiveness of a zone refining pass is determined by two factors: the efficiency with which an impurity is segregated at the solidification front and the transport of the impurity within the molten zone.

Segregation of impurities is governed by the thermodynamics of the material system. When solid and liquid mixtures form an interface at local equilibrium, the location of the interface will be such that the Gibbs free energy of the total system

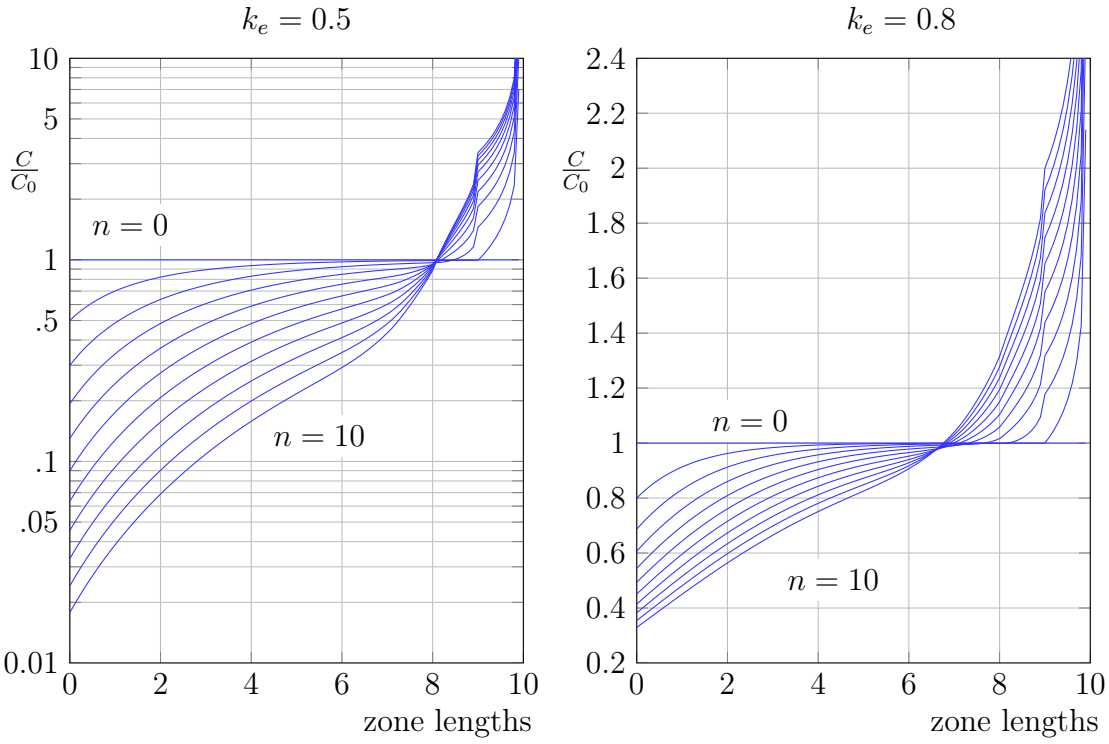

Figure 4.5: The distribution of an impurity after n zone refining passes depends strongly on the effective segregation coefficient, k. Distributions were calculated for a zone length equal to 0.1 times the ingot length using Hamming's method as described by Pfann [28].

is minimized and therefore the chemical potentials of the solid and liquid mixtures are equal to each other. This is the basis from which equilibrium phase diagrams are drawn such as the one for CdTe-ZnTe shown in Figure 2.5 or the phase diagrams shown on the left in Figure 4.4. At such an interface at equilibrium, the solid and liquid concentrations are determined from the liquidus and solidus lines on the equilibrium phase diagram and from the interface temperature, T. The ratio between the solid and liquid concentrations is called the equilibrium segregation coefficient [28].

$$k_o = \frac{C_S}{C_L} \tag{4.1}$$

In addition to the direct effect of the equilibrium segregation coefficient, transport in the liquid zone affects the effectiveness of each zone pass. Solute rejected from the solidification front accumulates in the interfacial liquid because of the diffusive boundary layer that exists near the interface. The form of the quasi-steady, diffu-

sive concentration profile is very similar to that discussed in dissolution experiments in Section 4.5. Importantly, the accumulation of solute at the interface increases the concentration incorporated into the solid. The effect of this accumulation is expressed through the effective segregation coefficient which is less favourable than the equilibrium segregation coefficient. Assuming a steady rate of solidification and diffusion, this segregation coefficient can be expressed in terms of the growth rate f, boundary layer thickness δ and diffusivity D.

$$k_e = \frac{1}{1 + \left(\frac{1}{k_o} - 1\right)\exp(-f\delta/D)} \tag{4.2}$$

Using this effective segregation coefficient, the concentration profile after n zone passes can be expressed as a function of distance [28].

$$\frac{C_n(a)}{C_o} = 1 - (1 - k_e)e^{-ak_e} \times \left[n - \sum_{s=1}^{n-1}(n-s)k_e^{s-1}e^{-sk_e}\frac{(s+a)^{s-2}}{s!}\left[a(s-1) + (1-ak_e)(s+1)\right]\right] \tag{4.3}$$

The distance a is typically normalized with respect to the lenth of the liquid zone, l, which is some fraction of the ingot length L. A reasonable zone length is $0.1L$. This equation is valid only in the region more than n zone lengths away from the tail of the ingot. The increased concentration in the final zone length will in fact be reflected forward in subsequent zone passes, and final concentration profiles need to be developed through iterative means. Such profiles have been generated for a wide range of conditions, and two such plots can be seen in Figure 4.5.

The effectiveness of the zone refining passes is characterized by the effective segregation coefficient. The further the coefficient is from unity, the fewer passes are required to achieve purification. This is illustrated in Figure 4.5 in which the lowest relative concentration achieved after 10 passes of a molten zone is 0.02 when $k_e = 0.5$ but only 0.25 when $k_e = 0.8$. 0.8 is the approximate segregation coefficient of selenium in tellurium, and it is selenium that necessitates the majority of zone passes during the refining of tellurium.

Two zone refining studies were conducted prior to the current work that aimed to improve mass transport near the solidification front, reduce the thickness of the diffusion boundary layer, and reduce the effective segregation coefficient. The first

study, which was lead by Jordan Haas, used strong electric current to sweep solute away from the solification front [29]. The second study, carried out by the author, attempted to improve mass transport through the application of RMF to the liquid solution [30]. Neither study showed a significant improvement in the effective segregation coefficient.

One reason that electromigration and magnetic stirring did not improve transport in the molten tellurium zones is the low electrical and thermal conductivities of tellurium. While the low electrical conductivity limited the strength of the electromagnetic forces achievable in the tests, the associated low thermal conductivity promoted strong natural convection in the solution zone which out-weighed any effect of the applied fields. The lack of any detectable effect in the zone refining experiments makes it less likely that RMF would significantly affect transport in tellurium THM solution zones which also experience strong convection.

Zone refining experiments were also conducted in cadmium. Cadmium has a much higher thermal conductivity than tellurium, which makes thermal control of the molten zones much more difficult. Compressed air was used to cool the ingot between molten zones, making the zone size more stable. A side effect of this stabilization was to enhance the convection in each zone, but no significant change was observed in the effective segregation coefficients.

4.3 Synthesis of Source Material by Fast THM

In preparation for THM growth studies, synthesis experiments were carried out in both the 25 mm and the 65 mm research furnaces. The THM synthesis process is identical to the growth process described in Section 2.2.2, but with the compounded CdTe source material replaced with metallic cadmium and tellurium. During processing, the upward motion of the travelling liquid tellurium zone continually dissolves the metals, which react to form the CdTe compound which then precipitates into an ingot below the advancing solution zone. One advantage of the method is that the highly exothermic compounding reaction is largely controlled by the translation rate. Ternary synthesis by THM also shares the advantage of ternary growth, producing a uniform composition in the resulting ingot. The synthesis process is often referred to as fast THM because because a single crystal product is not required. Translation rates can therefore be as high as than 20 mm/d compared to growth processes which are typically limited to 1 or 2 mm/d.

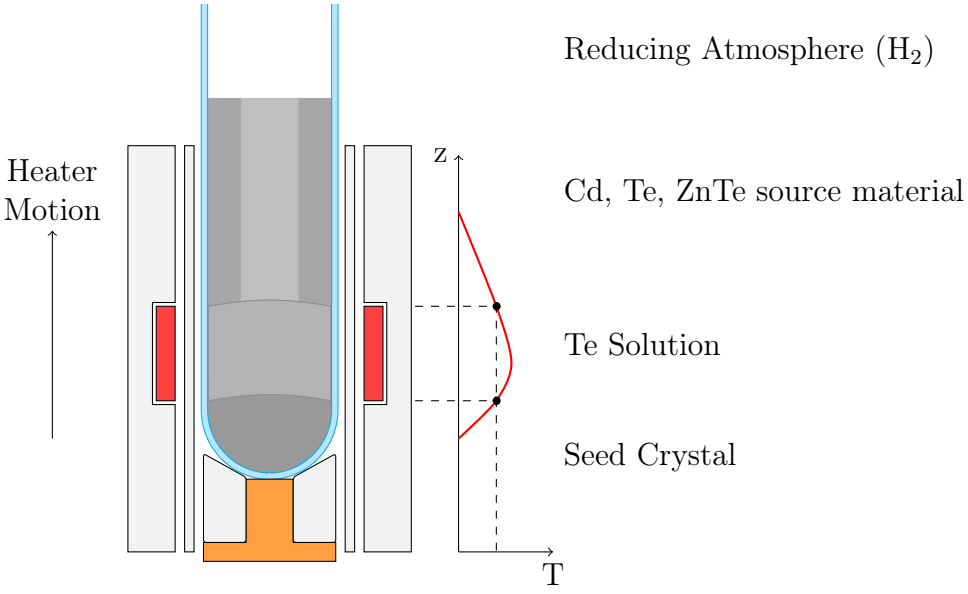

Figure 4.6: Schematic of a THM synthesis experiment.

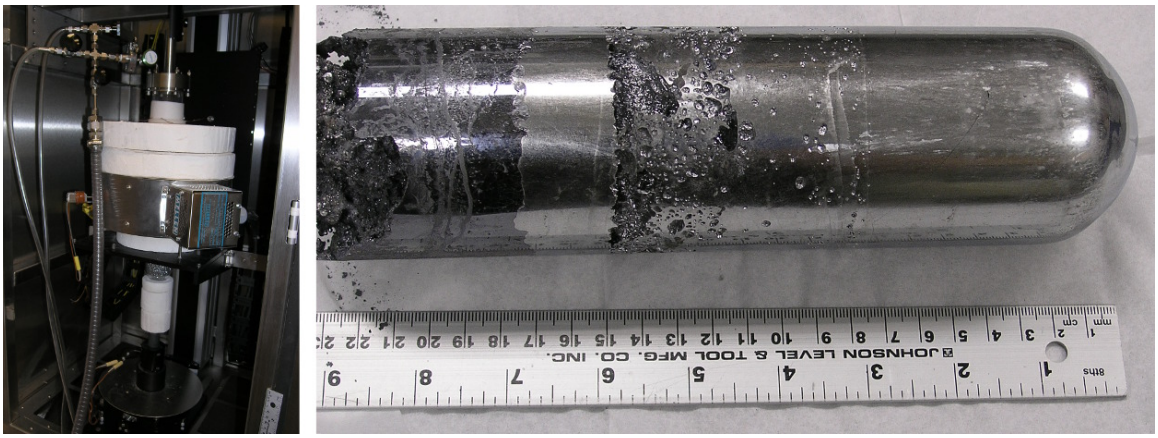

Figure 4.7: Left: CdTe65-1 prior to growth Right: Ingot resulting from CdZnTe65-2

Synthesis experiments were part of three different projects related to the current work. First, in previous work before even the preliminary THM growth study with GaSb, rapid THM synthesis of CdTe from the elements was studied using the same 25 mm diameter furnace. In that work, a rotating magnetic field was applied to the solution zone, but no effect was found on the maximum rate at which large-grain CdTe could be synthesized [23]. With and without the magnetic field, synthesis progressed smoothly at translation rates up to 50 mm/d, but the solidification interface broke down and tellurium was incorporated into the synthesized product when the translation rate was higher. Subsequent observation of grain structure showed no difference in ingots grown at 50 mm/d with varying magnetic field strengths. As was found in the zone refining study, the low thermal and electrical conductivities of liquid tellurium promoted strong thermal convection while limiting the magnitude of electromagnetic forces.

Synthesis experiments were carried out again during commissioning of the larger 65 mm THM furnace for the current growth study. The experimental configuration was as shown in Figure 4.6. CdTe was synthesized from Cd and Te, and CdZnTe was produced from Cd, Te and ZnTe. These experiments, shown in Figure 4.7 and referred to later as CdTe65-1 and CdZnTe65-2, showed that the necessary temperature conditions for THM growth had been achieved in the 65 mm system. Observation of the hemispherical first-to-freeze region revealed immediate large-grain growth and the grains established at the outset grew in vertical columns. The nucleation and growth of large grains in this system was one reason why unseeded THM growth was attempted in the smaller 25 mm furnace in experiments CdZnTe-1 and CdZnTe-2.

4.3.1 Source Material for FOTON 12 M4 Program

In addition to these THM synthesis experiments, an opportunity arose early in the present study to prepare CdZnTe source material via rapid THM for a multinational project under the auspices of the European Space Agency. Crystal growth has been an important aspect of space science for many years, and many crystal growth experiments have been conducted under low gravity conditions on a variety of orbital platforms. Low gravity eliminates buoyancy and therefore thermal and solutal convection. It is therefore very useful for studying diffusion and the effect of applied magnetic fields on the quality and properties of crystallized material [31].

The original goal of the project *Crystallization of CdZnTe* was to conduct growth

Table 4.1: Sample specification for FOTON growth project

Specification	Value
Composition	$Cd_{.95}Zn_{.05}Te$
Diameter	31.9 mm
Length	80 mm
Weight	350 g
Number of Samples	5

experiments on the international space station; however the toxicity of cadmium prohibits experiments on manned orbiting platforms. The project therefore changed its focus to the Russian unmanned FOTON series of satellites. The FOTON facility is an excellent vehicle for crystal growth in space. It offers much lower acceleration than the ISS because it is unmanned. The FOTON's POLYZON furnace offers facility for crystals up to 40 mm diameter. Finally, long term experiments are possible with heavy metal compound semiconductors.

The THM growth experiments were to be carried out in the POLYZON furnace, both on the ground and on board the FOTON M4 satellite. The POLYZON furnace consists of 8 independently controlled cylindrical heater zones, which can be located at different positions along the furnace axis. For THM growth, the heaters are positioned to allow a thermal spike to be translated axially via electronic control. The furnace is also equipped to displace the sample and to apply RMF with variable field strength and frequency.

The objective of the work in our facility was to provide polycrystalline feed material for these experiments. All samples were to be identical within the limits of practicability in terms of diameter, length, composition, grain size and lack of porosity. The sample specifications were as listed in Table 4.1.

A single batch of 5% CdZnTe was procured from 5N Plus, which had been produced by the company's standard fast THM process and then crushed to 2 mm particles, mixed, and sealed and shipped under vacuum in packages containing 500 g each.

The five ingots of feed material listed in Table 4.2 were cast by fast THM using this study's (nominal) 25 mm diameter furnace after CdTe growth experiments had finished but before the CdZnTe growth experiments. Ampoules for this work were made from semiconductor grade quartz, vacuum formed to 32 mm diameter over a length of 100 mm from the flat ampoule bottom. An individual 500 g package was

Table 4.2: Samples of feed material delivered for FOTON M4 experiments

FOTON ID	UVic ID	Feed Material	Diameter mm	Length mm	Mass g
F1-004-GM	THM-F4-2013-0	CdTe , ZnTe	31.95	81	375
F1-005-GM	THM-F4-2013-1	$Cd_{.95}Zn_{.05}Te$	31.95	83	386
F1-001-FM	THM-F4-2013-2	$Cd_{.95}Zn_{.05}Te$	31.85	86	401
F1-002-FM	THM-F4-2013-3	$Cd_{.95}Zn_{.05}Te$	31.9	90	420
F1-003-FM	THM-F4-2013-4	$Cd_{.95}Zn_{.05}Te$	31.9	90	420

openned for each experiment and loaded into the ampoule followed by 50 g of 6N tellurium as solvent. The ampoule was sealed and then evacuated several times and purged with pure hydrogen gas. A slow flow of hydrogen was established for the duration of the casting process.

During processing, a hot zone was established below the initial position of the tellurium solvent and then translated to the ampoule base at 20 mm/d. During this time, the tellurium migrated to the hot zone and moved with it to the bottom of the ampoule. Past experiments have shown that this results in a contiguous, but porous compounded charge above the solution zone. The direction of the ampoule motion was then reversed and the solvent passed upward through this compound at 5 mm/d producing a solid ingot with uniform composition.

The samples produced by this method were weighed and inspected from the outside for evidence of voids and cracking, but internal inspection was very limited in order to avoid destroying the samples. Thin slices were cut from the top and bottom and stored for possible future analysis. In addition, a flat surface 3 mm wide was ground along the edge of sample F1-003-FM and the composition was measured on the outside surface along the ingot's length using energy dispersive X-ray spectroscopy (EDS). The results shown in Figure 4.8 suggest a level distribution of zinc from one end to the other with significant local variability. It should be noted, however, that the x-rays used in EDS do not penetrate deeply due to CdZnTe's high atomic number and although the frame size used in measurements was approximately 1 mm^2, the mass sampled in each measurement is not sufficient to eliminate surface effects or variation caused by grain boundaries.

Because of a delay in the delivery of the feed material, an initial trial ingot was produced using 6N CdTe and ZnTe particles from 5N Plus which were on hand at UVic. The trial was very successful and was macroscopically indistinguishable from

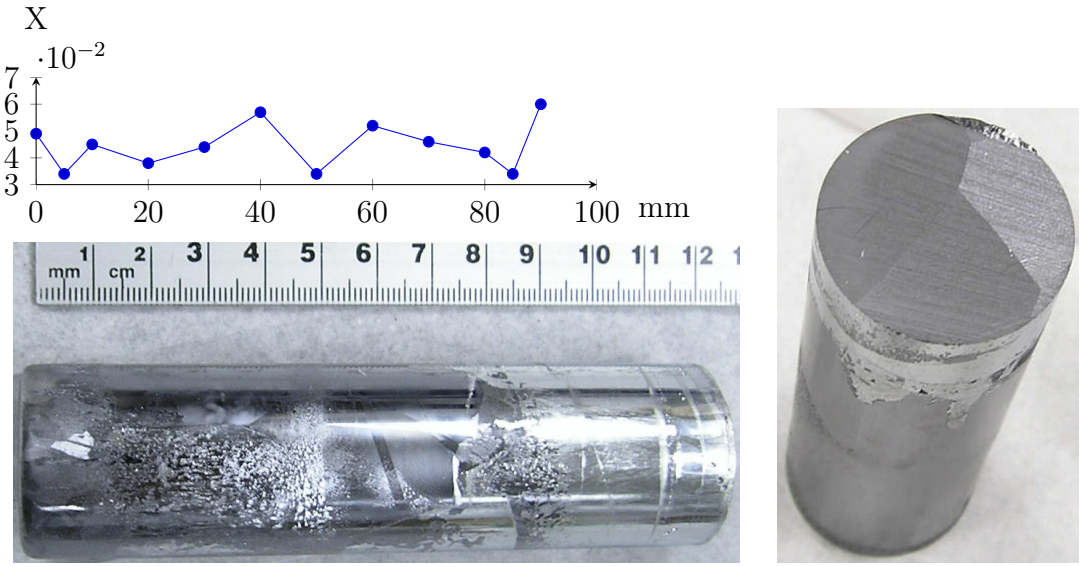

Figure 4.8: $Cd_{1-x}Zn_xTe$ sample F1-003-FM cast by rapid THM for growth experiments on the FOTON M4 satellite. Large grains in the first-to-freeze region of the casting experiments motivated unseeded experiments in the CdZnTe growth study.

the later samples produced with ternary feedstock. It was provided as F1-004-GM for preliminary ground testing of the growth furnace. It is expected that this sample has different trace impurities than the others, but such differences would have no impact on the determination of growth parameters for subsequent flight samples.

Although the casting program was not a THM growth study, it demonstrated several techniques that were adopted for subsequent experiments. The procedure of consolidating particulate source with a downward THM pass had been used in CdTe growth experiments but it was refined in the casting experiments. The ampoules used for the casting process were also the first to be treated with the pyrolized graphite coating used in later CdZnTe growth experiments. The presence of large grains near the first-to-freeze region of the resulting ingots was one reason why unseeded growth was attempted in subsequent CdZnTe experiments.

4.4 Production of Seeds by VGF

The vertical gradient freezing method for growing crystals was described previously in Section 2.2.1. CdTe seed crystals were produced via VGF so that THM growth experiments could be attempted. The specific VGF process used was very simple, and no attempt was made to achieve excellent material properties or even large single crystals.

4.4.1 Superheating of the Melt

The structure of molten CdTe is a current topic of debate, and no attempt was made in this work to contribute to the knowledge in this area. The recommendations of past authors were followed, however, with regards to superheating of the melt, and the results were positive enough to warrant comment here.

Rudolph, comparing the results of several studies, suggests that at temperatures less than 9 °C above the melting temperature, CdTe remains 95 percent associated and contains molecular complexes including tetrahedra, rings or chains. This highly structured fluid nucleates grains readily with very little supercooling. When the liquid is superheated to higher temperatures, it dissociates into individual species. Such dissociated liquid has been reported to supercool up to 30 °C before freezing rapidly [7]. Superheated melts do, however, produce larger grains and fewer twins in CdTe crystals grown by VGF and also by the heat exchanger method [32]. Presumably this is because larger ring and chain structures are not available to nucleate new grains and growth proceeds in atomic steps. Rudolf recommends superheating CdTe melts prior to growth. In unseeded growth, this produces a rapidly crystallized tip region with small grains followed by self-oriented growth with fewer grains and twins in the remainder of the ingot. This initial supercooling suggests that once a melt has been superheated, it remains largely free of complex structures even as its temperature is lowered below the melting point.

At the University of Victoria in 1999, Lingzhi Li demonstrated some success in combining low and high superheating of the melt. Prior to growth, a temperature gradient was established with less than 10 °C superheating at the ampoule base and up to 25 °C at the top. Cooling from this state produced single crystals with 25 mm diameter.

This work extended Li's approach by superheating the melt after the nucleation of an initial "seed" in the base of the ampoule. This was accomplished by imposing

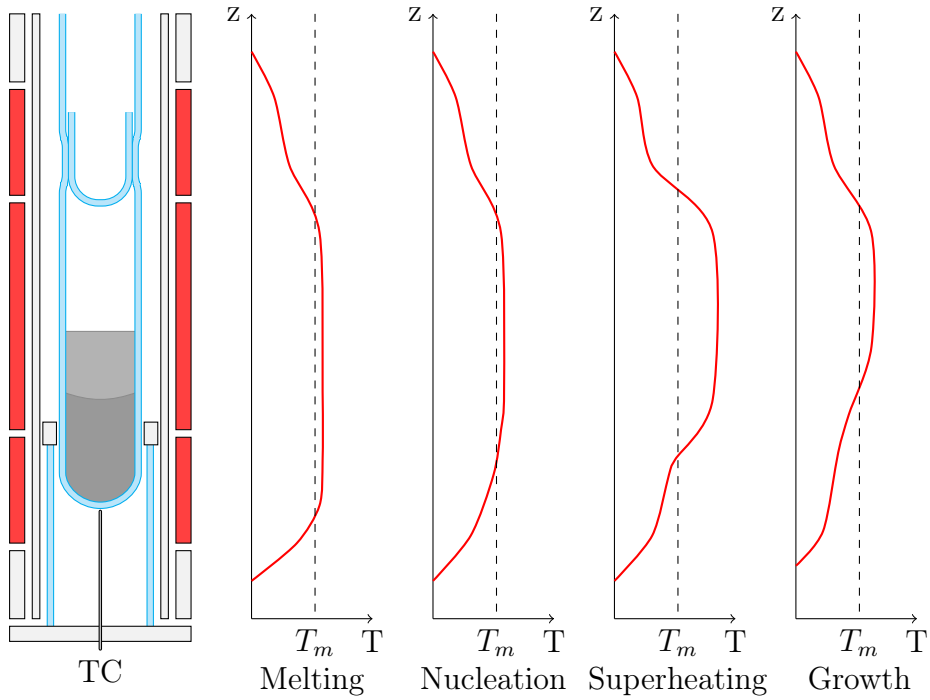

Figure 4.9: Schematic of the VGF apparatus

a steep temperature gradient near 1 °C/mm after the onset of solidification. This procedure ensured complete dissociation of the melt, and it resulted in a single crystal structure containing relatively few twin planes.

4.4.2 Procedure

Gradient freezing experiments were carried out using 25 mm and 50 mm diameter quartz ampoules with hemishperical bottoms.

Prior to each experiment an ampoule and sealing plug were etched with aqua regia, rinsed and dried. Broken CdTe was poured into the ampoule followed by the sealing plug which rested on top of the material during the sealing process. After repeated evacuation and purging, the ampoule was sealed under vacuum with an oxy-hydrogen torch, and the sealed ampoule suspended in a three zone, 75 mm diameter vertical furnace. A ring of solid insulation, supported by a quartz tube, separated the airspaces of the bottom and middle furnace zones at the midpoint of the sample as shown in Figure 4.9. The tube and insulation ring reduced airflow and increased the axial temperature gradient in the sample.

The entire charge was melted and superheated by only 5 °C. A thermocouple in

Table 4.3: Solidification experiments for seed production.

Experiment	Diameter	Mass	Result
CdTeVB1	25 mm	250 g	Two large grains
CdTeVB2	25 mm	250 g	Two large grains
CdTeVB3	50 mm	1000 g	50 mm of growth with one twin
CdTeVB4	50 mm	1000 g	Several large grains.
CdTeVB5	50 mm	1000 g	Large grain with twin slabs

contact with the tip of the ampoule recorded its temperature as the lower furnace zone was cooled to nucleate a pseudo-seed in the hemispherical tip. The tip was held below the melting temperature, and the remainder of the melt was superheated by 20 °C. The superheating was reduced and the system was cooled at 1 K/h to solidify the crystal. The system was then cooled to room temperature at 100 K/h.

4.4.3 Results of VGF Experiments

Boules were grown at 25 mm and 50 mm diameter, and Table 4.3 summarizes their results. The two smaller diameter experiments each showed two long grains occupying half of the ingot. The grains were not large enough to yield seeds for THM growth, but the ingots provided useful THM source material. Both ingots have recesses near 70 mm above the ampoule base as can be seen in Figure 4.10. It appears that the top 20 mm of the ingots solidified from the top down due to radiative cooling of the top of the ingots. The three larger boules have similar recesses, but slightly lower near 50 mm from the base of the ingot. At this height, the ingots are bisected by a break in the grain structure. There is also cracking in this vicinity. These larger ingots have nearly single crystal structure in the bottom 50 mm of the growth.

The lower 50 mm of the three larger boules each had two or three twin planes. These were identified visually from the outside, and each ingot was cut parallel to the twin planes to produce three slabs 15 mm thick. Chemical etching with E-Ag solution confirmed that the top surface of each slab was perpendicular to the <111>A crystallographic direction. Cylindrical seeds for THM growth experiments were core drilled from these slabs.

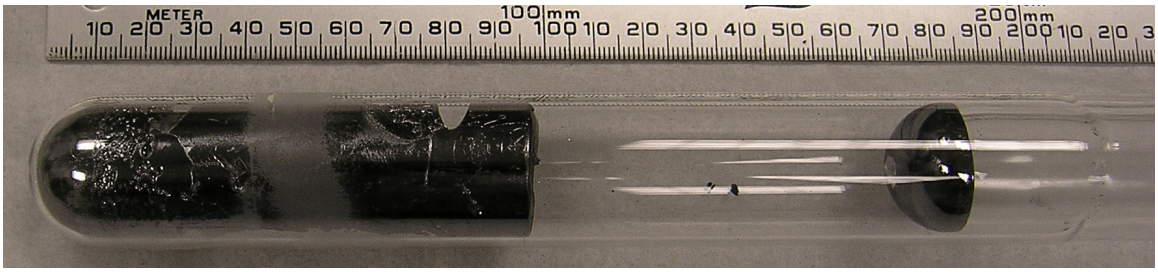

Figure 4.10: CdTeVB1 before removal from its ampoule.

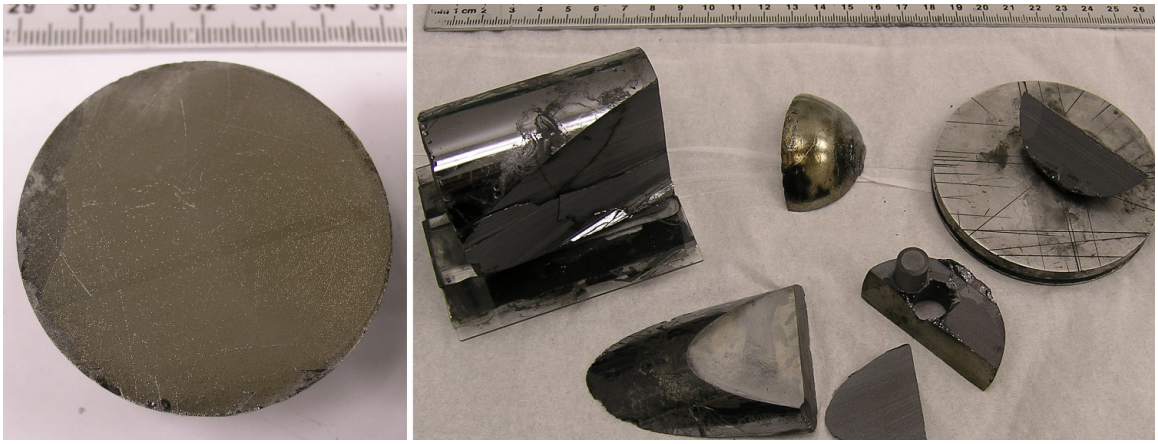

Figure 4.11: Left: Hemispherical tip of CdTeVB3 with visible twin planes. Right: Slabs and a seed cut from CdTeVB3.

4.4.4 Discussion

The VGF experiments in this work were not aimed at growing detector-grade CdTe, but they might better be described as casting experiments aimed at producing large enough grains to produce small seed crystals for THM growth. This goal was achieved, and the resulting material was sufficient to provide seed crystals for the THM experimental study. In the three larger experiments, single crystals were established at the onset of growth and proceeded with a small number of twin planes for around half of each ingot's volume.

The superheating strategy appears to have been successful. Large grains were established in the first-to-freeze region. There is no evidence of sudden crystallization, which suggests that the solid tip was maintained during superheating of the melt. After the heat treatment, the melt produced relatively clean large grain material with few side grains. Once cut parallel to the twin places, the ingots produced single crystal slabs up to 15 mm from which cylindrical seed crystals for THM experiments

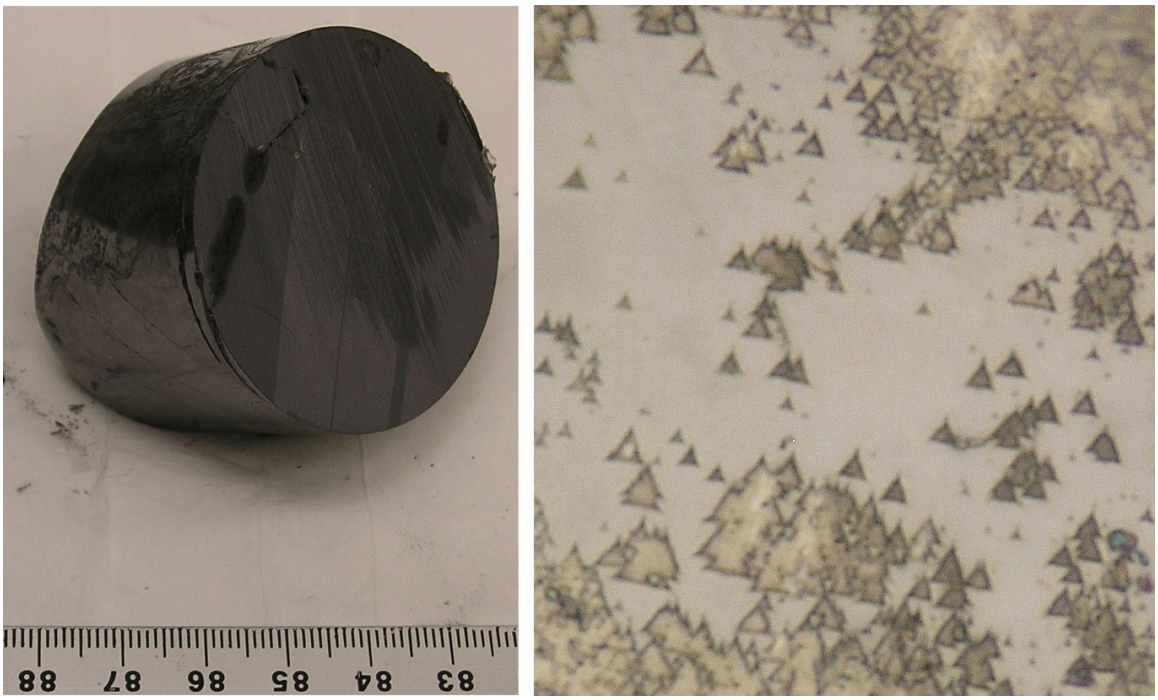

Figure 4.12: Left: CdTeVB5 during cutting. Right: Typical etch pits from E-Ag solution used to identify the (111A) face of a CdTe slab.

were core-drilled.

Unfortunately, the upper region of each ingot did not produce useful seed material. Each ingot cooled radiatively from the top during growth, causing the ingot to solidify from both ends. The resulting voids reduced the useful ingot volume by half.

The cutting of seed crystals was straightforward but labour-intensive. The cutting process for the first seed produced from CdTeVB3 can be seen in Figure 4.11. Twin planes were identified in each ingot, and slabs were cut parallel to these planes using a tape saw with boron-carbide slurry. The slabs were mechanically polished and then etched with E-Ag solution as described in Section 4.1. The twin planes in CdTeVB5 are visible in Figure 4.12 along with etch pits produced on the planes after cutting and polishing.

With the (111A) and (111B) faces identified, cylinders were core-drilled from the slabs using brass and stainless steel cutting tools fabricated to work with a boron-carbide slurry. Unfortunately, mechanical damage could not be completely avoided during the fabrication process. This was mitigated by cutting the seeds large and then removing 0.5 mm of material by chemical etching.

4.4.5 Conclusion

Cylindrical CdTe seed crystals for the THM study were cut from large-grain ingots grown by VGF. Three 1 kg ingots were produced and processed into seed crystals. An untested to superheating of the melt was employed successfully in the VGF experiments. Nucleation after small superheating produced large initial grains which were preserved during larger superheating of the melt. Although this method produced large grains in the first to freeze region, radiative cooling of the ingot tops disrupted growth in the upper half of each ingot. Nonetheless, enough large grains were obtained and mined to provide the seeds for the subsequent THM study.

4.5 Dissolution Experiments

4.5.1 Motivation

Simulations of crystal growth processes rely on knowledge of the underlying material properties. In the context of THM in particular, the dependance of liquid properties on temperature and composition has not been widely studied. For the THM simulations in this work, most material properties were chosen to match the simulation results published by others. The diffusivity of CdTe, however, was also measured at two temperatures relevant to THM growth.

Mass transport in THM is dominated by advection due to liquid tellurium's low viscosity, low thermal conductivity, and strong thermal and solutal expansion. The systems in this project are characterized by Grashoff and Prandtl numbers in the range of 10^9 and 0.06. Under the right conditions, however, such as experiments in microgravity or under large magnetic fields, diffusion may become significant. Diffusive boundary layers also exist at solid-liquid interfaces even when convection is strong, so diffusion rates should be understood in order to correctly model solution growth processes.

Diffusivity measurements contributed to the THM study in three ways. First, they established the value of a parameter for simulations. Second, the simple isothermal geometry of the diffusion experiments was an important test of the simulation software during its development. Third, the dissolution experiments gave quantitative results suitable for publication within the context of a THM development process that was more difficult to quantify. This work has been published in the Journal of Crystal Growth [33], and Section 4.5 consists almost entirely of the content of that publication.

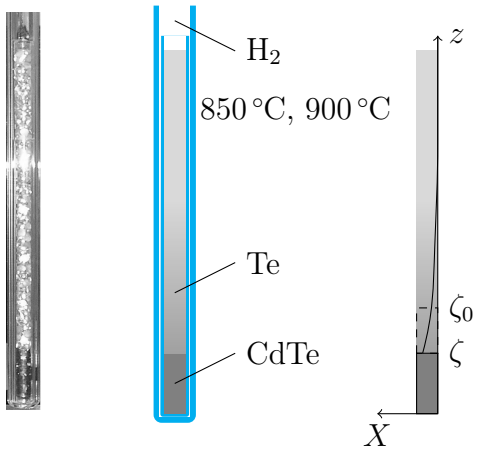

Figure 4.13: Quartz crucible prior to processing.

4.5.2 Experimental Procedure

Because convection tends to dominate transport rates, the value of the diffusion coefficient must be measured under conditions that minimize convection. For such measurements, a microgravity platform is best whenever possible. In earth-based experiments, convection is controlled or suppressed either by using small systems or with applied magnetic fields.

In the present work, CdTe samples were dissolved in isothermal liquid tellurium under diffusive conditions for three different experiment durations. For each experiment, the rate of dissolution was compared to a 1-D analytical diffusion model. The molar fraction of CdTe was also measured in the solution zones of three representative samples to validate the model and confirm that the experiments were diffusion-dominated.

In order to achieve diffusive conditions, the dissolution experiments were performed using slender quartz tubes and a stable configuration, as shown in Figure 4.13. CdTe is heavier than tellurium in solution, so to minimize natural convection the cylindrical CdTe sample was placed below the solvent in a 7 mm diameter quartz ampoule. The CdTe and Te were precast at 7 mm diameter and were 20 mm and 80 mm tall respectively.

The CdTe samples were dissolved for 45 min, 90 min or 180 min. For each dissolution time two experiments were performed at 850 °C, and three at 900 °C.

The ampoules were first heated to 400 °C in the top zone of a vertical furnace for 30 min under hydrogen atmosphere. Each dissolution experiment was initiated

by lowering the ampoule into the hotter isothermal zone of the furnace causing the tellurium to melt and the CdTe to dissolve into the solution. At the end of the dissolution period, the ampoule was removed from the furnace and quenched in air. The ampoule and sample were cut along the axis for analysis.

The length of the processed CdTe rod was measured, and the diffusivity was calculated from its change in length over the duration of the dissolution. To confirm that the transport regime was diffusive, the mole fraction of CdTe was measured by EDS along the axis of three representative samples. The measurements were taken using an Oxford Instruments Link ISIS EDS X-Ray microanalysis system on a Hitachi S-3500N scanning electron microscope. The results match the analytical prediction and confirm that the transport was diffusion dominated.

4.5.3 Analysis

The evolution of the atomic fraction, X, of CdTe in an isothermal liquid Te solution is governed by the mass transport equation, which has diffusive and advective terms.

$$\dot{X} + \operatorname{grad} X \cdot \mathbf{v} + D \operatorname{div} \operatorname{grad} X = 0 \tag{4.4}$$

Where X is defined to be 1 in CdTe compound and 0 in pure tellurium, D is the diffusivity of CdTe in the solution, and $\mathbf{v}$ is the velocity driven by solutal convection. In solution, CdTe is accepted to be 5.6 percent heavier than Te [34, 35]. If a solution is richest in CdTe at the bottom, it is therefore in a stable configuration, and the velocity will be very small. Under these conditions, the system may be assumed to be dominated by diffusion, and thus Eq. 4.4 in 1-D becomes

$$\frac{dX}{dt} - D\frac{d^2X}{dz^2} = 0. \tag{4.5}$$

We now use this equation to estimate the diffusivity. To obtain an analytical solution, the moving boundary condition at the dissolution interface must be handled through a change of variables. Using the initial interface position ζ_0, initial liquid mole fraction X_∞, and the equilibrium interface mole fraction X_i, we therefore replace the height z, interface position ζ and mole fraction X with natural variables.

$$z^* = z - \zeta_0 \qquad \zeta^* = \zeta - \zeta_0 \qquad X^* = \frac{X - X_\infty}{X_i - X_\infty} \tag{4.6}$$

The resulting Stefan problem can now be stated. We seek the interface position $\zeta^*(t)$ and mole fraction $X^*(z^*, t)$ in the domain $t \in [0, \infty)$ and $z^* \in [\zeta^*(t), \infty)$, given the following governing equation and boundary conditions.

$$\frac{dX^*}{dt} = D\frac{d^2X^*}{dz^{*2}} \tag{4.7}$$

$$\frac{d\zeta^*}{dt} = D\frac{X_i - X_\infty}{1 - X_i}\frac{dX^*}{dz^*}\bigg|_{z^*=\zeta} \tag{4.8}$$

$$\zeta^*(0) = 0 \tag{4.9}$$

$$X^*(z^*, 0) = 0 \tag{4.10}$$

$$X^*(\zeta^*, t) = 1 \tag{4.11}$$

$$X^*(\infty, t) \to 0 \tag{4.12}$$

This system has an established similarity solution using the complementary error function with an appropriate choice of a constant η [36].

$$X^* = \frac{\operatorname{erfc} \eta\frac{z^*}{\zeta^*}}{\operatorname{erfc} \eta} \qquad\qquad \zeta^* = \eta\sqrt{4Dt} \tag{4.13}$$

$$\operatorname{erfc} x = \frac{2}{\sqrt{\pi}}\int_x^\infty e^{-s^2}\,\mathrm{d}s \tag{4.14}$$

The constant η is found by comparing Eqs. 4.8 and 4.13 and solving numerically.

$$\eta + \frac{1}{\sqrt{\pi}}\frac{X_i - X_\infty}{1 - X_i}\frac{e^{-\eta^2}}{\operatorname{erfc} \eta} = 0 \tag{4.15}$$

When the dissolution distance ζ^* and elapsed time are known, the diffusion coefficient is calculated directly from Eq. 4.13.

4.5.4 Results

The distance dissolved in each experiment is summarized in Table 4.4. Dissolution distance increases with time and temperature, as expected.

The diffusion coefficient was calculated for each experiment using Eq. 4.13, and the model was also fitted to the measured distances in a least squares sense. The resulting diffusivity values are $0.008\,\mathrm{mm}^2/\mathrm{s}$ at $850\,^\circ\mathrm{C}$ and $0.009\,\mathrm{mm}^2/\mathrm{s}$ at $900\,^\circ\mathrm{C}$ with

Table 4.4: Experimental results

T (°C)	t (min)	ζ (± 0.5 mm)
850	45	3.0, 3.5
	90	4.4, 4.7
	180	7.0, 8.0
900	45	4.8, 5.1, 5.2
	90	7.5, 7.6, 7.7
	180	9.7, 10.1, 10.1

a standard deviation of 0.001 mm^2/s. This uncertainty is shown in Figure 4.14, which compares the experimental results to the interface motion predicted by the analytical model.

4.5.5 Discussion

Uncertainty in the dissolved distance arises from the measurement process itself, from the fit of CdTe rods in the crucible and from the fit of rods against each other when short pieces needed to be stacked. The length of each rod was measured with calipers before the experiment, and the height of the CdTe stack was measured again after dissolution and cutting. An overall uncertainty of 0.5 mm is estimated for the differential measurement.

The dissolution time is also affected by the time required to heat the sample from 400 °C to the process temperature. Using a lumped capacitance model, the time to achieve 90 percent of the temperature change is 5 minutes. The effect of including this time delay in the analysis was to increase the calculated diffusivities by at most 5 percent, and it is likely that the effect is much smaller as diffusion will begin before the temperature has settled. The results reported therefore do not account for any delay at the start of the experiments.

To confirm that the transport regime was diffusive, the mole fraction was measured along the axis of three representative samples using EDS. The compound segregated upon solidification into a needle pattern, so averaging was employed during the measurements. Each reading was taken by scanning a view frame measuring 1.6 mm x 1.2 mm. The samples are shown in Figure 4.15 with a rectangle indicating the view frame of the microscope.

Despite the large scanning area, segregation resulted in highly variable mole fraction readings. Figure 4.16 shows the mole fraction measurements from the three

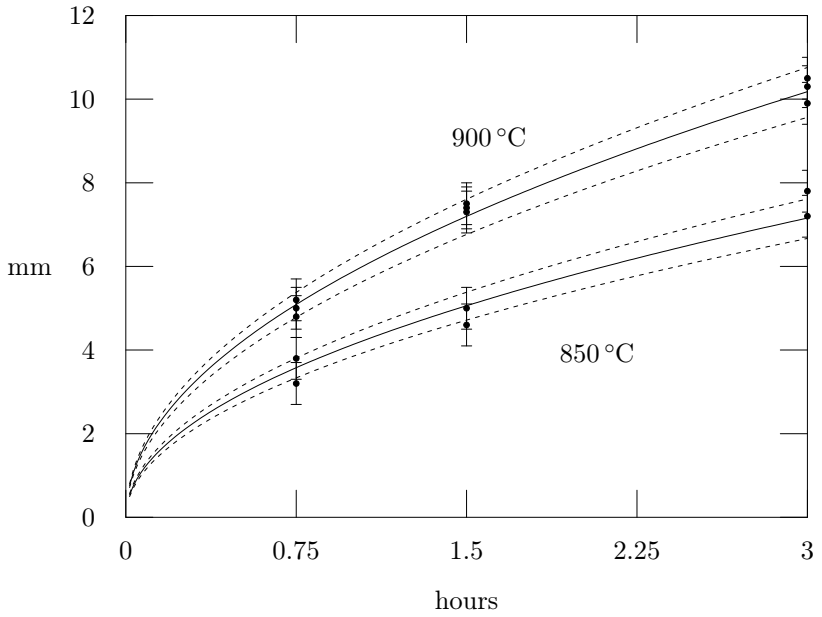

Figure 4.14: Predicted interface displacement (solid lines) after fitting the diffusivity to the experimental data. Dashed lines indicate the effect of increasing or decreasing D by $0.001\,\mathrm{mm}^2/\mathrm{s}$.

samples, and compares the EDS measurements to the predicted results. The height of each error bar indicates the uncertainty in its measurement (1.5% CdTe). Although segregation clearly produced strong additional variation, it is clear that transport in the liquid was diffusive and that the analytical model corresponds well to the experiments.

Experiments were also attempted with the compound at the top of the solution, but in this configuration transport was advective and too fast to produce meaningful results. Axisymmetric simulations indicated very strong convective flow due to the

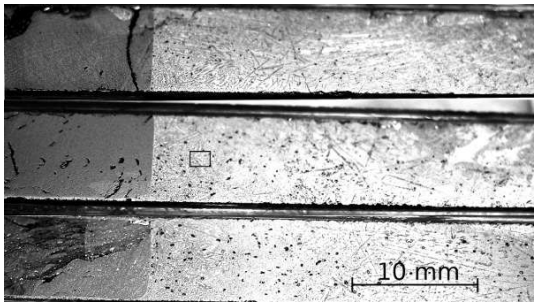

Figure 4.15: Solution zones after 45, 90 and 180 min at 900 °C. Rectangle is a representative EDS view frame.

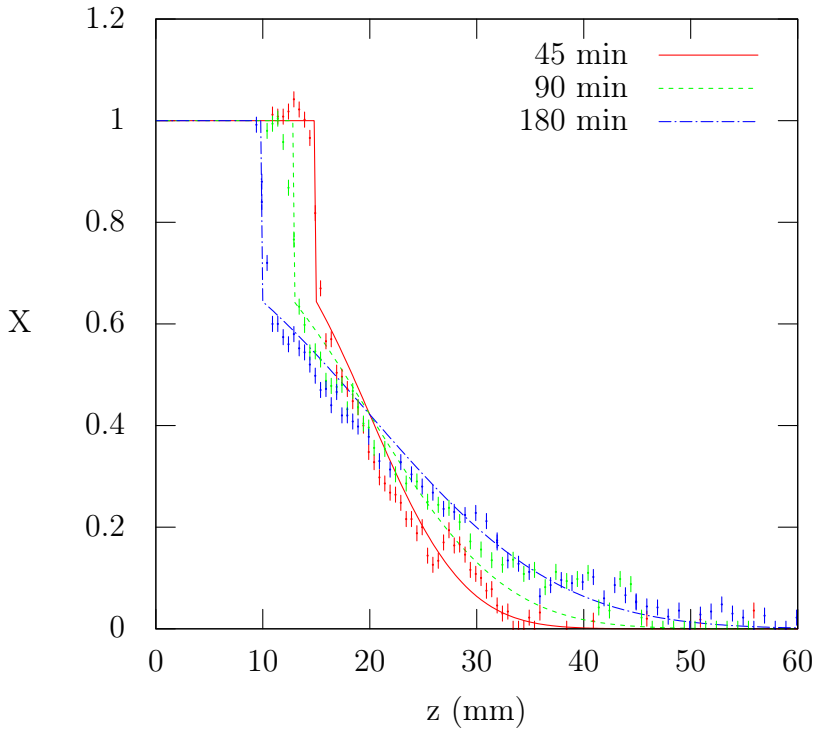

Figure 4.16: Calculated and measured mole fraction profiles after 45, 90 and 180 min of dissolution at $T = 900\,^{\circ}\mathrm{C}$, $D = 0.009\,\mathrm{mm}^2/\mathrm{s}$.

strong solutal expansion and low viscosity of liquid Te. The resulting flow had a Grashof number near 10^6 and a Reynolds number near 10^2, which are similar to values reported by Ghaddar in simulations of the traveling heater method [19]. Dissolution experiments in the silicon-germanium system have also reported strong dependence of the transport regime on the configuration of the experiment [37].

Most authors who simulate solution growth processes with Te solutions of CdTe report assumed diffusion coefficients of $0.004 - 0.005\,\mathrm{mm}^2/\mathrm{s}$ [38, 19]. Ko et al. calculated the diffusivity ab initio for solutions with $X = 0.4$. Figure 4.17 compares our measurements to their calculated values. The results indicate a linear dependence of D on temperature with a sensitivity of $0.0002\,\mathrm{mm}^2/\mathrm{sK}$.

Although the diffusivity depends on temperature, the rate of dissolution is influenced much more strongly by the temperature dependence of the interface composition. The mole fraction of CdTe on the liquid side of an interface at equilibrium is 0.53 at $850\,^{\circ}\mathrm{C}$ and 0.65 at $900\,^{\circ}\mathrm{C}$ [9]. At the lower temperature, 35 percent more compound must diffuse away from the interface for the same dissolution distance.

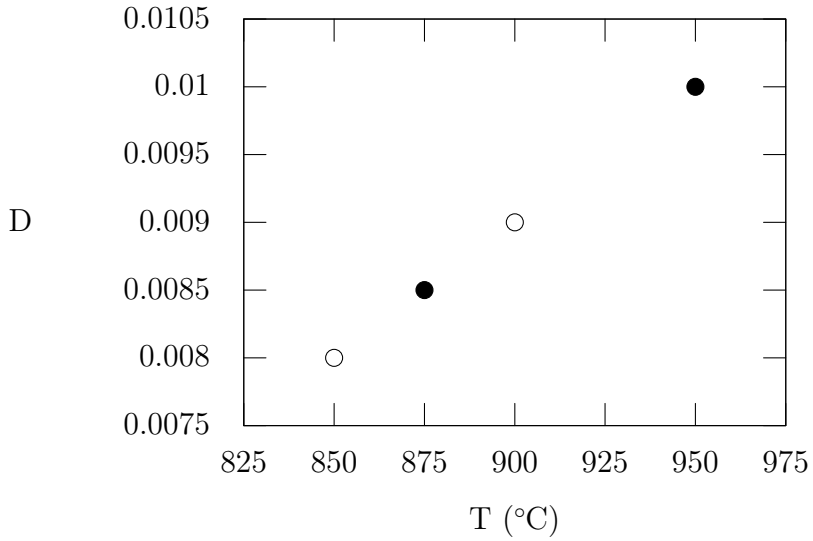

Figure 4.17: Diffusivities (mm^2/s) measured in this work (white), and calculated by Ko et al. (black)[39].

4.5.6 Conclusions

Diffusion experiments conducted at 850 °C and 900 °C indicate a diffusivity for CdTe in liquid Te of $0.008\,mm^2/s$ and $0.009\,mm^2/s$ respectively. Dissolution in the experiments occurred under diffusive conditions as expected from the solutal expansivity of the system and confirmed through EDS measurements.

Chapter 5

Experimental THM Growth of CdTe and CdZnTe

5.1 THM Growth Experiments

THM growth experiments were the core focus of this study. In previous work, GaSb had been grown by 25 mm diameter THM using 10 mm diameter seeds, and this project extended that work to CdTe and CdZnTe. In an effort to replicate the success of the GaSb growth experiments, CdTe and CdZnTe were grown repeatedly over a four year period to demonstrate the production of large single crystals from small diameter seeds. The course of the experimental study began with a long period of technical development toward a working 25 mm THM growth process for CdTe. These experiments are labeled sequentially as CdTe-1 to CdTe-22. After tapered growth was demonstrated for CdTe at 25 mm diameter, further development was undertaken toward the tapered growth of CdZnTe at 25 mm diameter (CdZnTe-0 to CdZnTe-8) and CdTe at 65 mm diameter (CdTe65-0 to CdTe65-8). These studies produced material with large, oriented grains, but single crystals could not be demonstrated. Their results do, however, appear to agree with simulation results that suggest that favourable growth conditions can be achieved.

5.2 Overview of the THM Experimental Study

The growth of 25 mm CdTe progressed steadily over the course of twenty-two experiments. CdTe-1 to CdTe-5 consisted of two quenching experiments to verify the length

Table 5.1: Summary of THM experiments

Experiments	Notes
25 mm	
CdTe-1 - CdTe-2	Thermal profiling, air quenched
CdTe-3 - CdTe-4	Unseeded, round bottom THM growth
CdTe-5 - CdTe-12	Tapered, seeded THM growth, no surface treatment
CdTe-13 - CdTe-15	Tapered, seeded THM, spray coatings
CdTe-16 - CdTe-22	Tapered, seeded THM growth, sand-blasted quartz
CdZnTe-1 - CdZnTe-2	Unseeded THM, conical tip with graphite coating
CdZnTe-3 - CdZnTe-7	Tapered, seeded THM growth, graphite coating
65 mm	
CdTe65-1, CdZnTe65-2	Unseeded synthesis from Cd, Te, ZnTe
CdTe65-3 - CdTe65-6	Unseeded THM, conical tip with graphite coating
CdTe65-7 - CdTe65-8	Tapered, seeded THM growth, graphite coating

and position of the tellurium solution, two unseeded growth experiments aimed at producing seed material, and seeded growth from a 25 mm polycrystalline pseudo-seed. Tapered, seeded growth began with CdTe-6 using a 10 mm diamater seed. CdTe-9 was the first experiment to show single crystal growth beyond the original seed region, and CdTe-12 showed largely single-crystal growth throughout its length, but with secondary grains appearing to nucleate at the wall. Spray coatings of graphite and boron-nitride were applied to the ampoule walls in CdTe-13 to CdTe-15, which reduced the incidence of secondary grains but resulted in many twin defects. A new series of experiments followed using a sand-blasted quartz surface to prevent wetting of the ampoule wall without risking contamination from a coating. The redesigned, sand blasted ampoules were used for CdTe-16 to CdTe-22, and in these experiments solid pre-cast source material was also replaced by crushed source material. This development process culminated in CdTe-20 and CdTe-22 which each showed substantial single crystal tapered growth with occasional secondary grains.

THM growth experiments were interrupted by a program of six experiments to cast precompounded $Cd_{.95}Zn_{.05}Te$ into 32 mm diameter ingots with uniform composition for space-based growth experiments. For these fast THM experiments, the small THM furnace was installed in a new, enclosed frame and ampoules coated with pyrolized graphite became available.

Because large grains were observed in the unseeded fast THM experiments, un-

seeded growth was attempted when the growth study resumed. The new furnace configuration and ampoule coating were kept for these CdZnTe experiments, which began with two unseeded experiments in ampoules with conical bases. Seeded growth followed, with 25 mm diameter CdZnTe grown on 10 mm seeds. In these final four experiments the seeds appear to have dissolved completely prior to growth.

Experiments at 65 mm diameter began much later than those at 25 mm diameter. Two synthesis experiments were first carried out, using elemental source material to test the new furnace, and then unseeded growth in conical, graphite-coated ampoules was attempted in the 25 mm and 65 mm THM furnaces simultaneously. During these unseeded experiments, the temperature conditions in the 65 mm furnace were varied to observe the effect on grain size in the tip and in the later growth of the CdTe ingots. Finally, two CdTe ingots were grown at 65 mm using 25 mm diameter seeds. These experiments resulted in large, oriented grains rather than in single crystals.

The THM experiments are organized in three series: 25 mm growth of CdTe, 25 mm growth of CdZnTe, and 65 mm growth of CdTe. Together, these experiments suggest that tapered THM growth may be possible from small seeds. They did not, however, convincingly demonstrate that it can be achieved in practice.

5.3 Experimental Procedure

Prior to each THM experiment, the glassware was etched with aqua regia and rinsed and dried thoroughly as described in Section 4.1. Ampoules treated with a pyrolized graphite coating were not subsequently etched.

The seed crystal was core-drilled using a boron carbide slurry to a diameter 1 mm larger required and then etched rapidly with several batches of E solution to fit closely into the ampoule's seed pocket. In early experiments with solid source material, the source ingot was precast by rapid VGF or taken from crystals resulting from VGF or THM experiments. Each source ingot was etched in the same manner as the seeds until it fit loosely into the ampoule.

In a cleanroom, the seed, source and ampoule were rinsed thoroughly with high-purity methanol and the ampoule was dried by evacuation. Approximately 2 g of tellurium was placed in the bottom of the ampoule followed by the seed. After evacuation and purging, the seed was heated with a propane torch or baked in the THM furnace. During this procedure, the tellurium melted and partially dissolved the seed, forming an alloy of Te and CdTe and locking the seed in the bottom of the

ampoule.

In early experiments, this baking procedure took place overnight. In later experiments it was done in the course of a few minutes. Section 5.5.2 discusses the problem of lost seeds and the steps that were taken to address it.

With the seed returned to room temperature, the ampoule was opened in the cleanroom and source material and tellurium added to it. In experiments using solid source material, the source ingot and additional CdTe shards were etched with E solution and rinsed thoroughly with water and then with methanol. Te shot and CdTe shards were poured above the seed crystal, and the source ingot placed above these. Beginning with CdTe-14, the source ingot was replaced by CdTe or CdZnTe particles, less than 2 mm diameter, which were unsealed and poured immediately on top of the seed. Tellurium shot was then poured on top of the particles.

Following this loading procedure, the ampoule was repeatedly evacuated and purged with high-purity hydrogen, and then evacuated for several hours, finishing with a vacuum below 10^{-4} mbar. A flowing hydrogen atmosphere was then established and maintained for the duration of the experiment.

The furnace was heated over 12 h with the peak temperature located several centimeters higher than the desired initial position for the solution zone, and then the heater or ampoule travelled to the desired initial growth position at 10 mm/d. After a rest of 12 h or more to stabilize the solution zone, growth proceeded by lowering the ampoule or raising the furnace, usually at 2 mm/d.

At the end of growth, the ampoule was cooled to room temperature over 24 h and the crystal was removed from the ampoule. Crystals were cut transversely in order to evaluate the size and position of grains, and then cut along the axis unless material was selected for use in future experiments. The crystal structure of each ingot was observed and evaluated. In some cases, large grains were identified and mined for seed material for new experiments.

5.3.1 Equipment

THM experiments were carried out in two furnaces. An existing two zone, 38 mm diameter vertical furnace was used for 25 mm diameter experiments, and a purpose-built 75 mm diameter furnace was developed and used for 65 mm diameter experiments. In the absence of applied magnetic fields or accelerated ampoule rotation, the conditions inside a THM growth ampoule are controlled only through control of the boundary

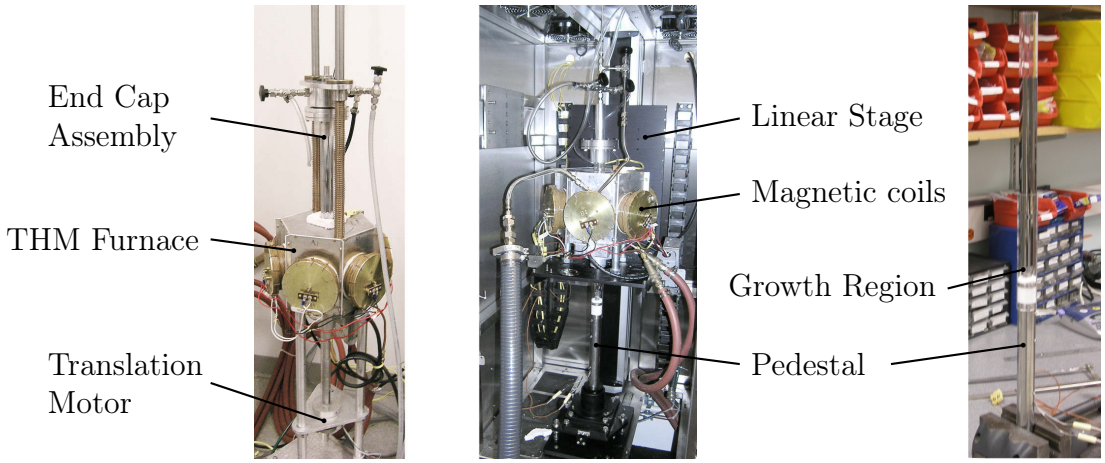

Figure 5.1: 25 mm THM furnace mounted on an open frame for CdTe experiments and enclosed prior to CdZnTe experiments. Right: Ampoule mounted on the final growth pedestal.

temperatures. In particular, the shape of the growth interface is sensitive to the rate of cooling applied to the base of the ampoule as well as the temperature profile along the ampoule wall. Most of the design choices with respect to the THM equipment were therefore focused on these two furnace properties.

The 25 mm furnace had been used previously for the tapered growth of GaSb, and the improvements implemented for that research were retained for the current work [24]. For the present study the furnace was originally mounted on a fixed aluminum frame, and the growth ampoule was translated by a stepper motor. This frame was capable of ampoule rotation and applied magnetic fields. Midway through the study, a steel enclosure was provided by 5N Plus, allowing the furnace to be translated without disturbing the ampoule and its contents. Accelerated rotation of the ampoule was implemented for the new system and applied in the final experiments. The original and new furnace frames and the final support configuration for 25 mm growth experiments can be found in Figure 5.1. Water cooling at the base of the furnace was used to generate an axial temperature gradient of 5 K/mm below the hot zone. The second heated zone was used occasionally to extend the molten zone, for example when consolidating source material. Otherwise the second zone was turned off, and the temperature gradient above the hot zone was measured to be 0.4 K/ mm. In addition to the furnace's axial temperature profile, heat extraction from the ampoule base was varied by adjusting the diameter and material of the support pedestal and by cooling the pedestal using a fan and removable cooling fins.

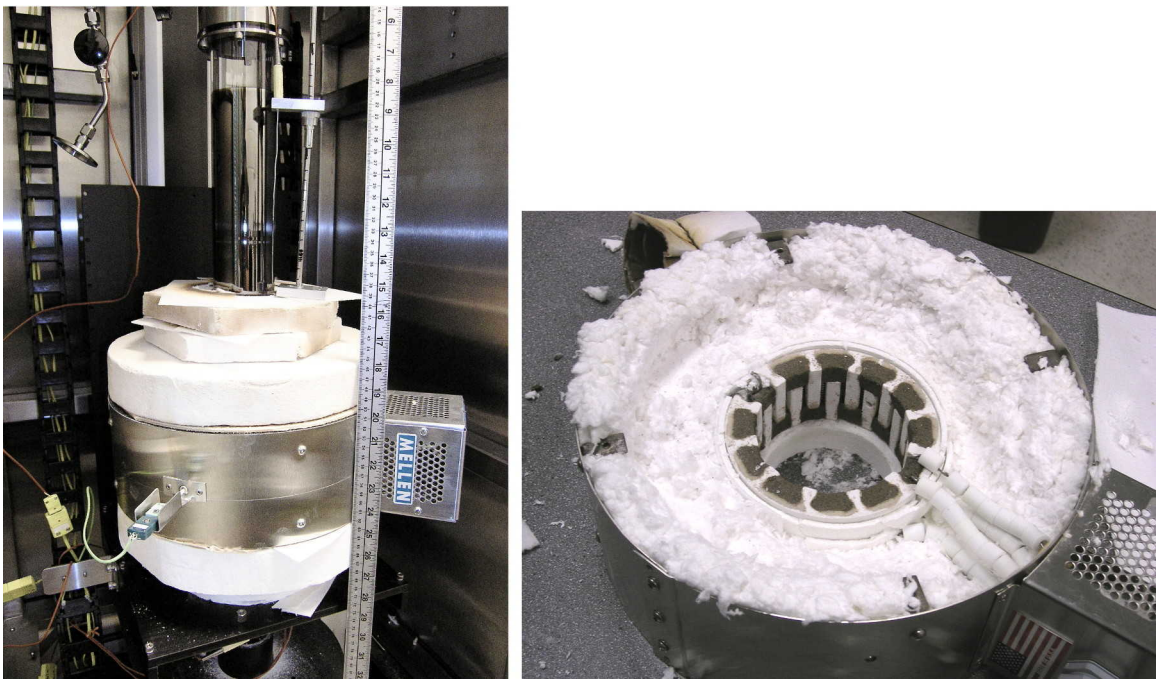

Figure 5.2: 65 mm THM furnace shown prior to CdTe65-6 and opened during replacement of the furnace core

The second furnace was designed for 65 mm diameter THM and built by Mellen Company. It was installed in a steel enclosure provided by 5N Plus. Translation of the furnace and rotation of the ampoule were implemented for this system. The furnace itself was designed to be as narrow as possible, with 600 W power output in a 50 mm zone length. This was accomplished by a pair of clamshell-style ceramic heaters enclosed above and below by 25 mm of rigid ceramic insulation. As shown in Figure 5.2, these heaters were wired separately and controlled independantly. Because there was only one control thermocouple in the furnace, the output of the second zone had to be tuned manually to achieve equal power output from the two clamshell heaters.

To adjust the furnace's temperature profile between experiments, additional rings of rigid insulation were added above and below the furnace. To accommodate this, all electrical connections to the furnace were mounted on the outside rather than the top or bottom. With minimal insulation, the furnace was capable of achieving only 1000 °C, and in experiments requiring large temperature gradients, the furnace had to operate near 90 percent of its rated power. This eventually led to failure of the furnace core and the replacement of the furnace with an identical unit for the final

two 65 mm diameter experiments. These were conducted with smaller temperature gradients which permitted more insulation above and below the furnace. The mullite liner was also replaced with quartz, and these changes allowed the furnace to operate at 65 percent of its power rating during the final experiments.

A key factor in the thermal conditions inside the growth environment is the rate of heat transfer through the base of the crystal. This was controlled in this study by varying the materials and form of the pedestal that supports the growth ampoule. In early untapered growth experiments at 25 mm diameter, the ampoule rested on a 10 mm copper finger surrounded by an insulating annulus in order to promote heat flow out of the centre of the ampoule base and produce a domed growth interface. This was retained for early tapered experiments, but in order to reduce the rate of cooling a stainless steel cap was later added above the copper. The initial pedestal in the 65 mm furnace consisted of a steel rod with 25 mm diameter surrounded by an insulating annulus. In both the 25 mm and 65 mm furnaces therefore, the ampoule seeds rested on heat conductors matching the seed diameters, and thermocouples were embedded in both in order to measure the axial temperature gradient and approximate the heat flux leaving the base of the ampoule.

Toward the end of the growth study, the ampoule support configuration was changed from top-mounted to bottom-mounted in order to allow ampoules to be rotated. This change was achieved largely through a change in the design of the support pedestal. The supports for both furnaces were replaced with stainless steel. In the 25 mm furnace a close-fitting quartz tube held the growth ampoule in line above the pedestal as shown on the right in Figure 5.2. 65 mm diameter ampoules rested upright on 25 mm diameter seed pockets without additional support. As seen in Figure 5.3 the new steel pedestals were equipped with offset thermocouples to measure the axial heat flow. The measurement region was reduced to a known diameter and then insulated to reduce parasitic heat leaks.

5.3.2 Ampoule Development for 25 mm CdTe Growth

The first phase of the THM growth study focused on the production of 25 mm CdTe crystals using 25 mm and then 10 mm seeds. Most of the development process for this study focused on the form and surface treatments for the growth ampoules.

Early tapered growth experiments used hand-formed ampoules with no surface treatment, but tellurium on the outside of several CdTe samples stuck slightly to the

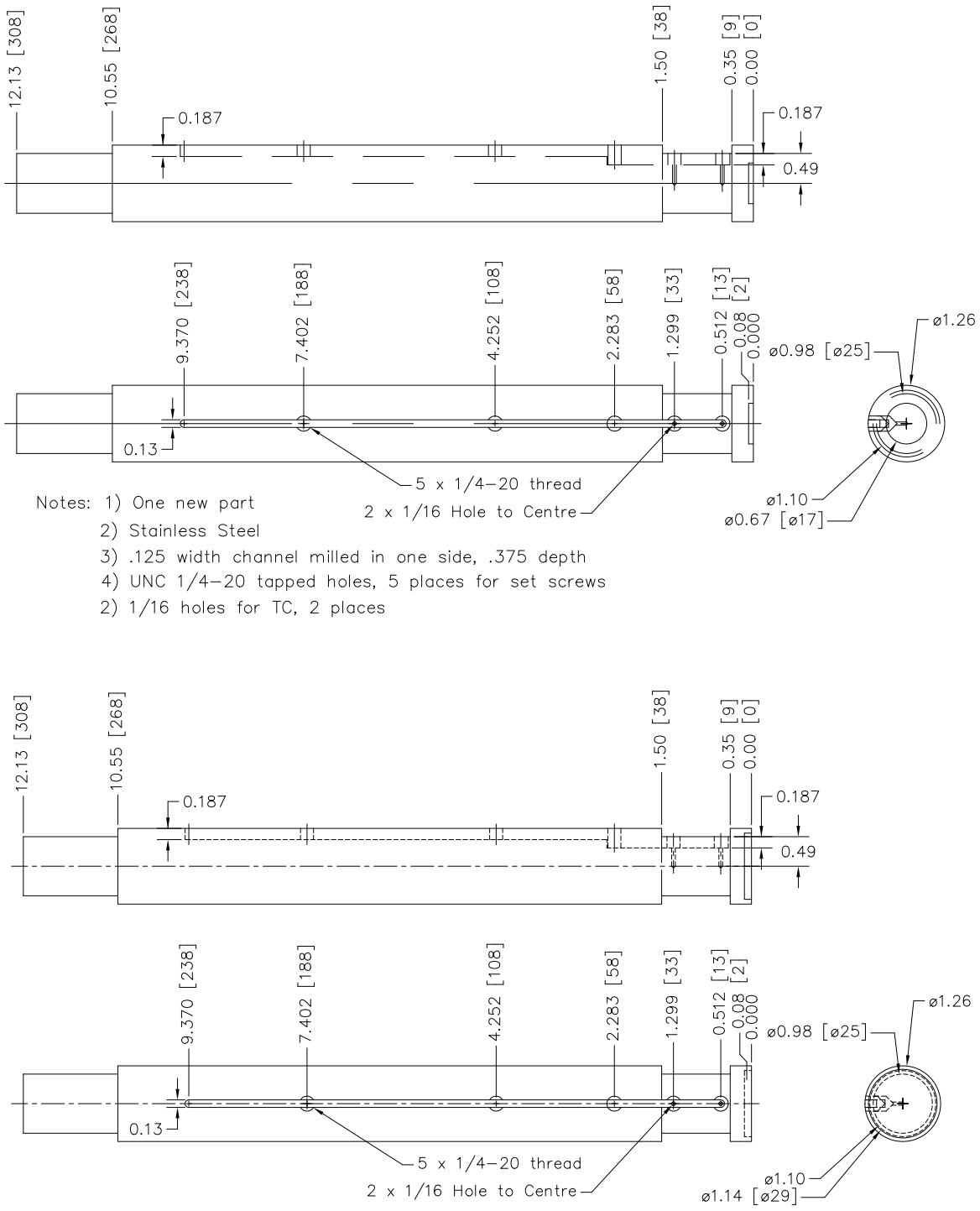

Figure 5.3: Final cold finger configurations for the 25 mm and 65 mm THM furnaces. Two thermocouples mounted at opposite ends of a reduced diameter, insulated length were used to approximately measure the heat flux out of the base of the ampoule.

Figure 5.4: CdTe12-0 was a typical experiment in untreated quartz ampoules.

untreated quartz. It could sometimes be freed with methanol and gentle tapping, but more often than not ampoules needed to be broken to retrieve their samples. It was also suspected that secondary grains were nucleating at the untreated wall as shown in Figure 5.4.

Four surface treatments were investigated in order to reduce interaction with the ampoule walls and ease the removal of the grown crystals. Following CdTe-12, sprayed coatings of graphite and boron nitride were used, followed by sand blasted quartz and then finally vapour-deposited graphite. In the three experiments that used spray coatings, the samples were largely single-crystal and were removed easily from the ampoules. Unfortunately, the crystals grown with spray coatings showed large numbers of twin plane defects, which can be seen in Figure 5.5. This is believed to have been caused by contamination of the charge material by the coating despite baking procedures intended to adhere the coatings to the ampoule walls.

A new ampoule design was next developed that allowed the 25 mm experiments to continue with sand-blasted quartz rather than spray coatings. A drafted crucible region was formed on a graphite mandrel and then sand-blasted and welded to an untreated upper tube with a slightly larger 25.4 mm diameter. Such an ampoule, assembled in two pieces, is shown in Figure 5.6. Crystals grown in these ampoules slid cleanly out of these drafted ampoules except CdTe-18, in which source material was left overlapping the welded joint. A great advantage of these ampoules was that

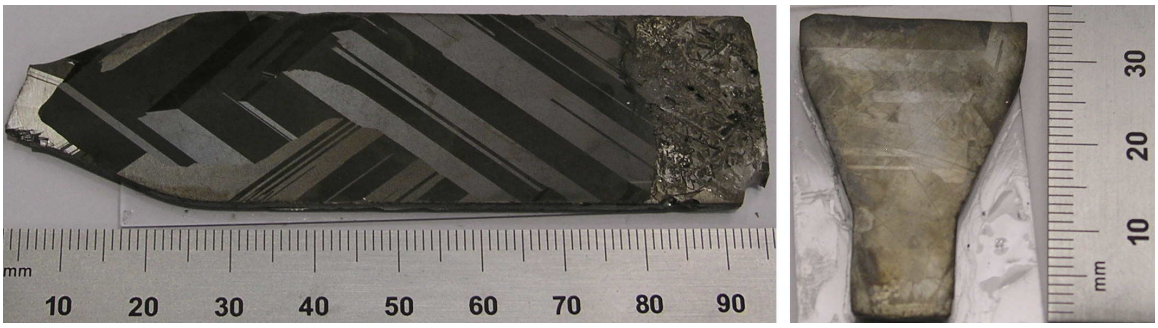

Figure 5.5: CdTe-13 (left) and CdTe-14, grown in ampoules treated with a sprayed boron nitride surface coating.

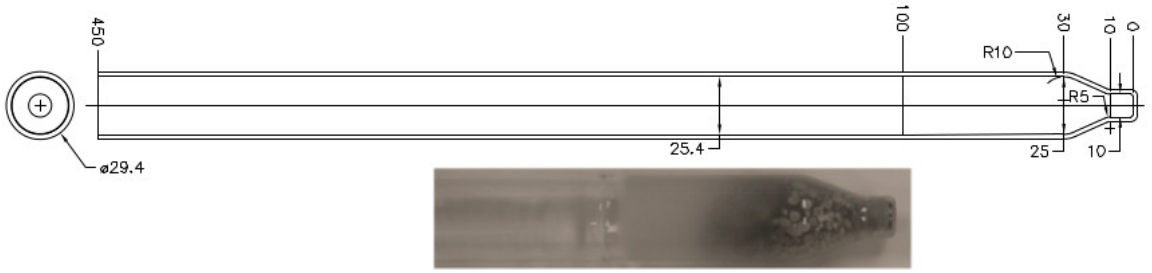

Figure 5.6: Sand blasted ampoule, as used in CdTe-17 - CdTe-22. Dimensions are in mm.

the pure quartz surface was amenable to chemical etching and cleaning. Because the ampoules were vacuum formed, a consistent and circular profile was also achieved which permitted cylindrical seed crystals to be matched closely to the inner ampoule diameter and prevented the slender seed regions of crystals from locking in place after growth.

The CdTe growth in sand blasted quartz ampoule appears to have remained detached from the ampoule wall. The best of these results was CdTe-22. In this, as in CdTe20 and CdTe21, the single crystal structure of the seed was carried through the first 10 mm of the tapered growth region, but in CdTe20 the structure was maintained until the diameter reached 25 mm except for a secondary grain that appeared after 15 mm of growth.

Vapour-deposited Pyrolized graphite coating became available during THM casting experiments and was used for seeded and unseeded 25 mm CdZnTe growth and 65 mm CdTe growth experiments. Graphite coating gave the best performance as far as the removal of grown crystals. It was, however, prone to being scratched during loading. The graphite coated ampoules were formed in one piece and included a

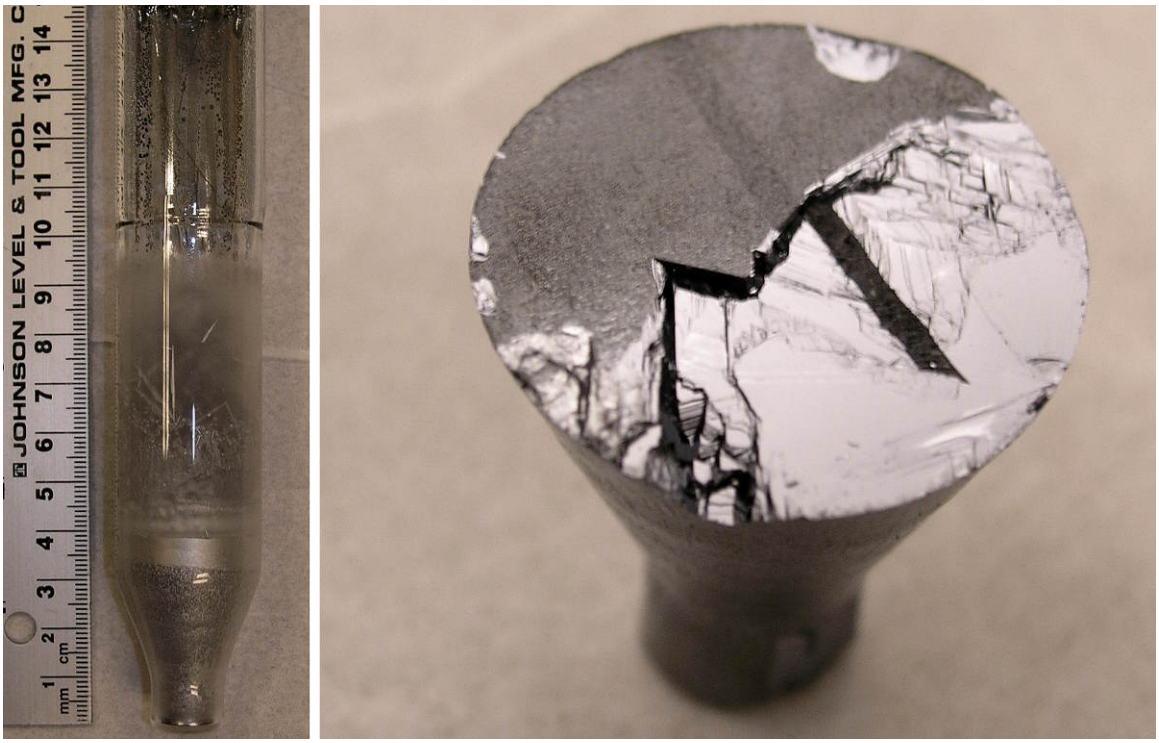

Figure 5.7: CdTe-22 exhibited nearly single-crystal growth expanding from 10 mm diameter to 25 mm

drafted lower crucible region. These were formed onto graphite mandrels to ensure consistent geometry and then coated inside with a 2.5 µm pyrolized graphite coating. Unlike the sand blasting process, carbon coating was readily applied to the entire interior of the ampoules without requiring that they be assembled in two parts. As expected, crystals grown with the graphite coating showed fewer secondary grains along the ampoule walls and they were removed much more easily from their ampoules compared to untreated quartz ampoules. Unfortunately the graphite coating appears to have been associated with the complete dissolution of seed crystals, particularly in the later CdZnTe experiments. The efforts to address this problem are described below in Section 5.5.2.

5.4 Unseeded Growth

Unseeded growth was attempted in the first experiments of the 25 mm diameter CdZnTe and the 65 mm diameter CdTe growth studies. These were motivated by the successful nucleation of single crystal material in the unseeded VGF experiments

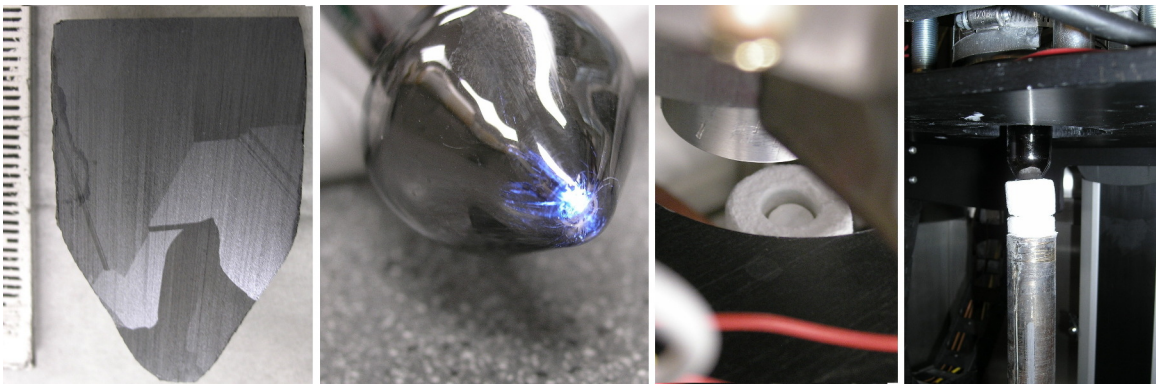

Figure 5.8: Left to right: CdZnTe-1 showed large grains after a fine-grain tip region. In an effort to reduce supercooling at the tip, the carbon coating was scratched away in the tip of CdZnTe-2. Both experiments rested on 5 mm of boron nitride on top of a copper pedestal. Insulation surrounded the ampoule tip to a height of 5 mm.

as well as large grains observed in several prior THM studies.

As described in Section 4.3, unseeded synthesis experiments were conducted during commissioning of the 65 mm THM growth furnace. In CdTe65-1, cadmium and tellurium were reacted using a travelling tellurium solution and formed an ingot with a spherical bottom. Large grains were rapidly established in the tip of the ampoule and propagated linearly along the length of the ingot. This experiment was repeated in CdZnTe65-2, with ZnTe added to the cadmium and tellurium reagants to form a solid CdZnTe ingot with large vertical grains. Both of these growth experiments produced grains 15 mm in diameter on average. These were too small to provide useful seed material, but the nucleation of large grains in the first-to-freeze region implied that unseeded growth might be possible.

Similarly, during the THM casting experiments described in Section 4.3.1, large grains were observed in the first-to-freeze regions of CdZnTe ingots. These were also seen in the seed region of THM growth experiments in which the seeds were lost. As discussed above in Section 5.5.2, the CdTe that replaced the lost seeds in the bottoms of the growth ampoules had had one or two large grains.

With large grains observed in the first-to-freeze regions of VGF, synthesis and casting experiments, unseeded growth experiments were attempted using conical ampoules in an effort to produce CdZnTe ingots with very large grains or single crystals. Graphite coated ampoules with conical tips were used for CdZnTe-1 and CdZnTe-2 at 25 mm diameter and for CdTe65-3 to CdTe65-6 at 65 mm diameter.

In all unseeded experiments, a short fine-grained region was observed for the first 4

Figure 5.9: Clockwise from top left: CdTe65-3,4,6 and 5. From CdTe65-3 to CdTe65-5 progressively more heat extraction yielded larger grains in the bulk but poorer initial nucleation. CdTe65-6 attempted to vary the heat extraction during growth, but it was curtailed by failure of the furnace core.

to 10 mm of growth. Larger grains tended to follow immediately and become larger as growth proceeded. The fine grain tip is believed to be caused by supercooling, which is a known problem in unseeded melt growth. When liquid CdZnTe is heated above its melting temperature by more than 10 °C, it has been observed to then cool below the melting temperature by up to 30 °C before solidifying suddenly [7]. When the melt is heated less than 10 °C supercooling is avoided. It is believed that the different behaviour is caused by the degree of dissociation of the CdTe molecules in the melt. In the unseeded THM experiments, the solution appears to supersaturate and then solidify rapidly. This behaviour is like the supercooling observed in superheated, highly dissociated CdTe melts.

It was hoped that the lower temperatures of THM would promote a higher degree

of association within the liquid solution and prevent supercooling. Unfortunately, evidence of supersaturation was found in all unseeded THM experiments. Efforts to promote nucleation such as scratching the ampoule surface were unsuccessful.

After the initial pair of synthesis experiments, the 65 mm diameter growth study continued with four experiments CdTe65-3 to CdTe65-6 using solid ingots of CdTe source material and ampoules with conical tips. The resulting ingots are shown together in Figure 5.9. The rate of heat extraction was increased progressively in the first three experiments, and increased heat extraction was associated with larger grains in later growth but poorer initial nucleation. CdTe65-3 was characterized by a large grain in the tip region which split quickly into many large grains as growth progressed. CdTe65-4 and CdTe65-5 showed fine grains in the tip which might have been caused by supercooling and sudden solidification in the tip region. A solid mass (2 g) of tellurium was found solidified in the tip of CdTe65-5, however, which suggests that the cooling of the ampoule base was so severe as to prevent the tip region from being heated to a sufficient temperature to establish a saturated solution. The fine grains in experiments with strong cooling of the tip may therefore result from low temperature rather than from supercooling.

It seems likely that a balance can be achieved between the large initial grain nucleation of CdTe65-3 and the large grains developed later in the growth of CdTe65-5. This was the goal of CdTe65-6, which began with a layer of insulation below the ampoule to achieve the higher nucleation temperature of CdTe65-3. After 30 mm of growth, the insulation was removed, increasing the heat extracted by the cold finger to match the conditions that produced favourable grains in CdTe65-5. This approach of changing the growth conditions after the initial nucleation of a pseudo-seed was used successfully in the production of seed crystals by VGF. Unfortunately, in this case an electrical failure in the THM furnace caused an early termination of CdZnTe-6. The strong heat extraction used in this series of experiments required very large heater powers which ultimately caused the furnace to fail. The sudden cooling of CdTe65-6 did allow some observation of the growth conditions. The growth interface is strongly convex toward the liquid indicating strong heat extraction from the ampoule base and favourable conditions for outward grain propogation. Unfortunately, small grains throughout the grown ingot suggest that a large grain was never established in the tip, but the furnace malfunction and subsequent burnout prevent any conclusions from being drawn from the experiment.

5.5 Seeded Growth of CdZnTe

Seeded growth experiments were first conducted for CdTe at 25 mm diameter using 10 mm diameter seeds, and these experiments were described in the preceding sections. They were characterized first by preliminary results (CdTe-5 - CdTe12), then by growth in spray-coated quartz ampoules (CdTe-13 - CdTe-15), and then by single crystals with occasional inset grains grown in sand blasted quartz ampoules (CdTe-16 - CdTe-22).

Seeded experiments were interrupted by casting experiments for a space-based THM study and then by unseeded THM experiments using CdZnTe source material. Following these, seeded growth experiments resumed using CdZnTe source material at 25 mm diameter with 10 mm CdTe seed crystals. As described in Section 5.5.2, the seeds in CdZnTe-3, CdZnTe-4 and CdZnTe-5 appear to have been completely dissolved with large grains established in their place at the bottom of each ingot. CdZnTe-6 and CdZnTe-7 were more successful.

Growth in CdZnTe-6 progressed as a single crystal containing small twins up to a height of 25 mm, near the top of the tapered growth region. After this, large grains were established and continued throughout the remainder of the ingot. A large enough grain was identified in CdZnTe-6 to provide a ternary seed crystal for CdZnTe-7. This cylindrical seed is shown on the right in Figure 5.10. Twin planes were used to identify (111) crystal planes for cutting the seed, and its orientation was confirmed using a Nakagawa etch. The 5 mm thick layer in the centre of the seed was the target seed-on location for the beginning of growth in CdZnTe-7.

The result of CdZnTe-7 is shown on the right in Figure 5.11. Large grains were established very early and progressed throughout the length of the ingot with off-grains and twin planes occurring from time to time. As in many other experiments, fine grains are visible in the seed region suggesting that perhaps the seed was dissolved completely before growth, but the large grains established in the seed region imply that the seed was intact when growth began.

5.5.1 Ampoule Rotation

CdZnTe-3 to CdZnTe-7 were grown at 25 mm diameter using 10 mm diameter seeds, but the earlier experiments exhibited highly asymmetric growth interfaces such as that shown in the left of Figure 5.11. Similar asymmetry was observed in the larger diameter experiments such as CdTe65-7, which is shown on the left of Figure 5.12.

Figure 5.10: Left: Ingot resulting from CdZnTe-6. Right: 10 mm diameter CdZnTe seed recovered from the centre of CdZnTe-6.

Figure 5.11: Left: CdZnTe-3 showed a highly asymmetric solution zone and growth interface (marked in white for illustration). Right: Accelerated ampoule rotation in CdZnTe-7 resulted in a more uniform interface and a more axisymmetric system.

The 25 mm THM furnace equipment was modified during the preliminary GaSb growth study in order to allow ampoules to be rotated during growth, but the system was unreliable. Ampoule rotation was not used in the 25 mm diameter CdTe growth study in the present work, and it was not fully implemented until after the furnace was remounted from its original open aluminum frame to the newer steel frame for CdZnTe growth experiments. The new frame allowed more precise vertical mounting of the ampoules which were suspended from their end caps and could be rotated by a top-mounted stepper motor. Unfortunately this arrangement continued to suffer from misalignment between the ampoule and the cooling pedestal, held from below in contact with the base of the ampoule. Ampoule rotation was therefore not used in 25 mm experiments until quite late in the study.

THM experiments rotated for 1 revolution in alternating directions with 2 minutes for each revolution. Experiments in which the ampoules were rotated showed significantly improved axisymmetry of their growth interfaces, as shown in Figure 5.11 and Figure 5.12.

Symmetry appears to have been a particular problem in this project because of the use of particulate rather than monolithic source material. The porosity of the source lead to a void observed outside the solution zones of nearly all experiments. In experiments without ampoule rotation, the void remained on one side of the ingot and contributed to significant asymmetry in the thermal conditions. This can be seen for example on the right side of Figure 5.11 where the side of the solution zone that has the void appears to have been significantly colder with a narrower solution zone and less dissolved solute. By contrast, the equivalent void in CdZnTe-7, on the right of Figure 5.11, surrounds the entire ingot symmetrically.

5.5.2 Fixture of Seed Crystals

In many experiments, the seed crystals appear to have been lost completely. This was most frequently the case in CdZnTe-3 to CdZnTe-8 in which graphite-coated ampoules were used. The graphite coating posed two challenges. First, it reduced the adhesion of the seed and its surrounding tellurium to the base of the ampoule. This was, after all, the purpose of the coating. Unfortunately, it appears to have caused the seeds in several experiments to be lost prior to the onset of growth. The second problem arising from the graphite coating was the inability to observe the seed from outside the ampoule. In earlier experiments, visual inspection was used

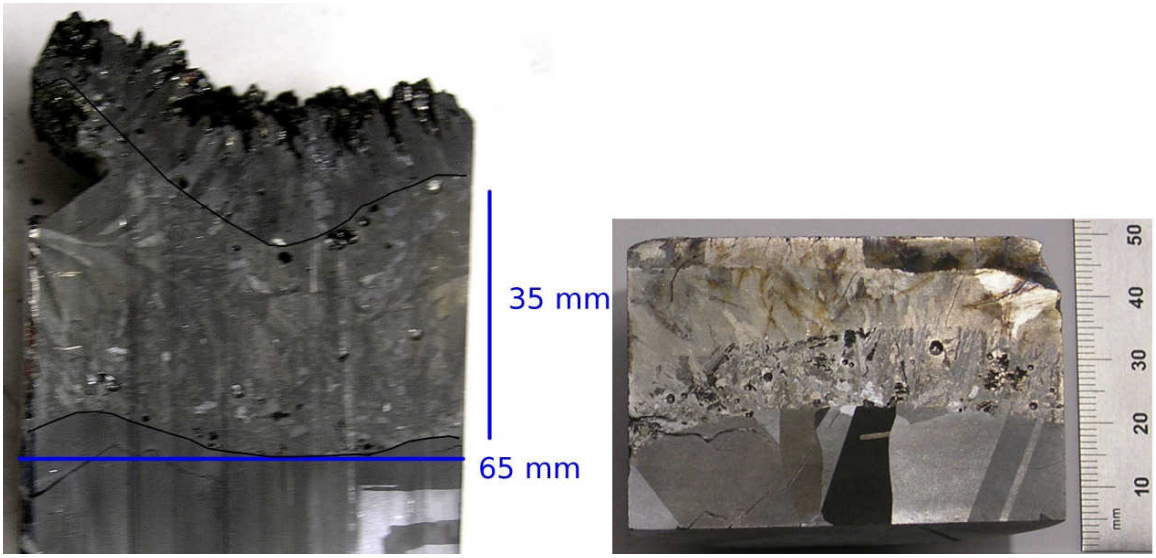

Figure 5.12: Left: Concave, asymmetric growth interface in CdTe65-7. Right: Accelerated ampoule rotation resulted in a more symmetric growth interface shape in CdTe65-8.

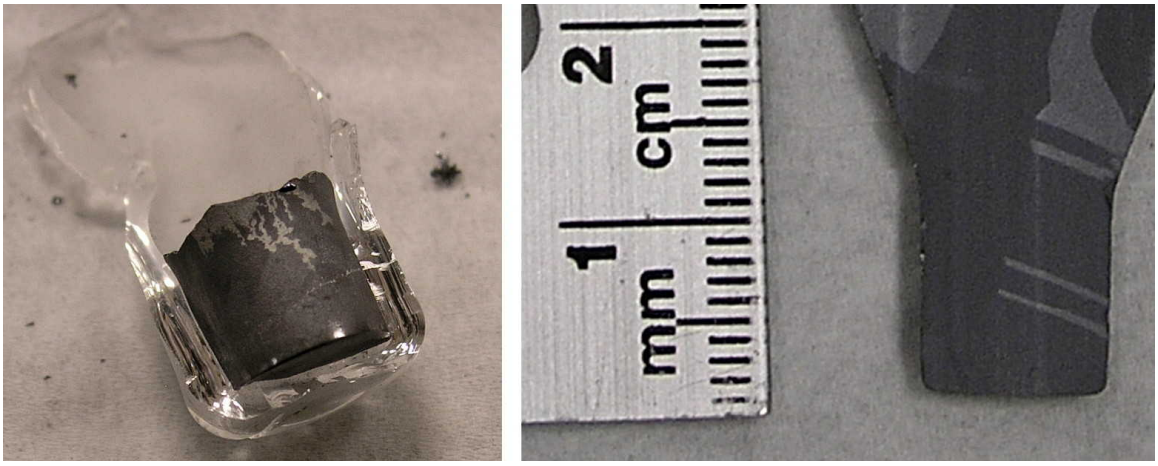

Figure 5.13: Left: Slight ridge around the base of CdTe-18 which locked the seed in place. Right: A deliberate 0.5 mm radius was added at the base of CdZnTe-3 in order to allow crystals to be removed intact.

to verify the location of the growth interface prior to growth. The ampoule would be removed briefly from the furnace, observed, and replaced. The change to coated ampoules made this more difficult, and the experiments may therefore have dissolved too much of their seed crystals.

Several mechanisms are possible for the loss of seed crystals. The first is that liquid tellurium from the solution zone may have infiltrated the space around the seed. Because solid telluride compounds are less dense than liquid tellurium, the seed may have been partially dissolved and then floated upward into the solution zone and been lost. This process is possible no matter how small the gap around the seed crystal because liquid tellurium wets both CdTe and the quartz ampoule walls. Even very small gaps are vulnerable to capillary action or vapour transport over the long duration of a THM experiment. One argument in favour of this mechanism for seed loss is that experiments in sand-blasted quartz ampoules, which the tellurium does not appear to have wetted, were the most successful at preserving their seed crystals.

It is also possible, however, that the lost seed crystals are a result of thermal conditions rather than liquid infiltration or floating. During the torching procedure, the seed rarely adhered to the base of the ampoule. Although some tellurium was placed below the seed, the result after heating with a propane torch was generally a mass of mixed tellurium and CdTe on the bottom of the seed and point contact with the ampoule base. When the ampoule was heated to the experimental temperature, the seed crystal was therefore in full, wetted thermal contact with the hot liquid solution zone and did not have an adequate thermal contact with the base of the ampoule and the cooling support pedestal. Immediate dissolution of the seed may have been followed by rapid deposition of CdTe onto the cold ampoule base.

A final possibility is that too much tellurium was added below the seed crystal in some experiments, and that this tellurium migrated upward during growth destroying the seed and depositing polycrystalline CdTe behind it.

Although most seeds were preserved during experiments in sand-blasted ampoules, after the shift to graphite-coated ampoules most seeds appear to have been lost. In addition to the graphite coating, a small change to the wall profile also made the new ampoules more subject to lost seeds. The previous sand-blasted ampoules had a sharp corner at the base of the seed pocket, and the process of pressing the quartz against the graphite mandrel during fabrication actually resulted in a slight recess. After growth, several seeds were locked firmly in place by a slight ridge that formed in this recess in the quartz. Such a ridge can be seen in the left of Figure 5.13. The

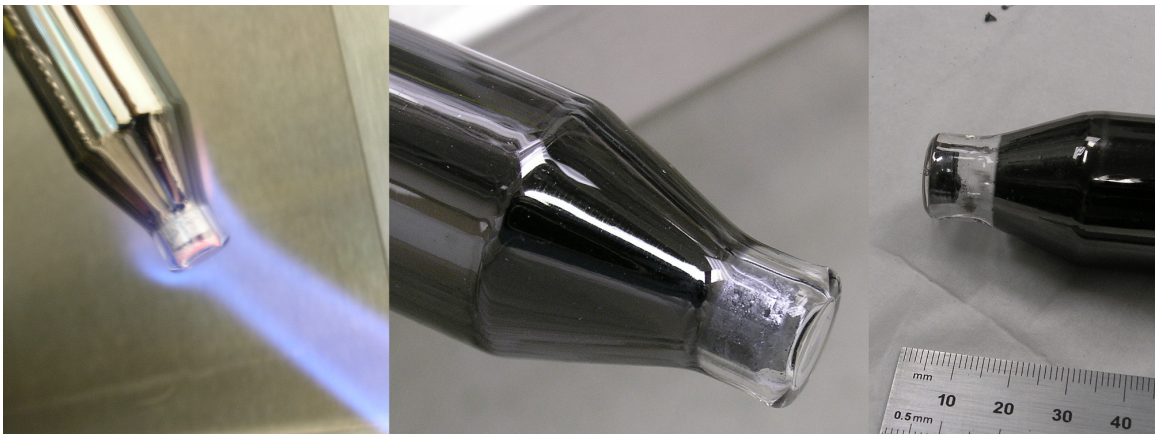

Figure 5.14: Left to right: CdZnTe-7 during and after the torching procedure to secure the seed crystal, and the bottom 4 mm of seed locked in place after the remainder of CdZnTe-6 was removed from the ampoule.

new, graphite-coated ampoules were fabricated with a 0.5 mm radius, which ensured that crystals slid easily out of their ampoules. Unfortunately, seeds were also less likely to lock in place at the start of the experiments. For the final experiments a new recess was deliberately added to the seed pocket as shown in Figure 5.13. This recess succeeded in locking the seed in place, but unfortunately, it prevented the crystals from being removed from the system without breaking either the ampoule or the seed region of the crystal. This is acceptable, however, as the small seed crystal has very little value when its experiment has ended.

For the final experiments CdZnTe-6 and CdZnTe-7, the graphite coating was burned away from the ampoule tip region with a torch. A new change was also made to the torching procedure. Out of fear that too much tellurium was being used to secure the seed and was subsequently dissolving it, the pure tellurium which had been placed below the seed was replaced with a mixture of crushed tellurium and CdTe. During torching, once the liquid was observed to wet both the seed and the ampoule, the hydrogen atmosphere was partially evacuated, causing tellurium to evaporate from the seed region and leave behind a CdTe-rich solid solution bonded to the seed. The combination of the bare quartz walls around the seed and this new torching procedure, shown in Figure 5.14, appears to have preserved the seeds in these final two experiments.

Figure 5.15: In CdTe65-7 The seed appears intact with nearly single-crystal growth in the first 20 mm of growth followed by large grains with [111] orientation.

5.5.3 Seeded 65 mm Diameter Growth

The seeded experiments at 65 mm diameter showed the same partial success as the CdZnTe experiments at 25 mm diameter. CdTe65-7 was grown from a 25 mm diameter seed crystal, which was found largely intact at the end of the experiment. Above the seed, a single crystal structure was established, but with several twin planes. This grew for 20 mm before several large grains were established, several of which continued to grow with the [111] crystal direction oriented upward. These grains continued for the remainder of the grown ingot. The last-to-freeze region of CdZnTe65-7 is shown on the left of Figure 5.12. The growth interface appears to have been concave in the centre, which may be related to the grain that can be seen growing up the centre of the ingot in the left of Figure 5.15.

For CdTe65-8, the heat extraction out of the bottom of the ampoule was reduced, but the axial temperature gradient in the furnace was increased. As desired, these changes allowed a single crystal structure to be established at the seed and growth progressed with an interface shape that appears to have been convex, judging from the shape of the original crystal and the locations where new grains were established. After 15 mm of growth, however, large grains were established once again and grew through the remainder of the experiment.

Unlike any other experiment, CdTe65-8 contains a large number of small voids in the first-to-freeze region. The cause of these voids is not known, but they likely

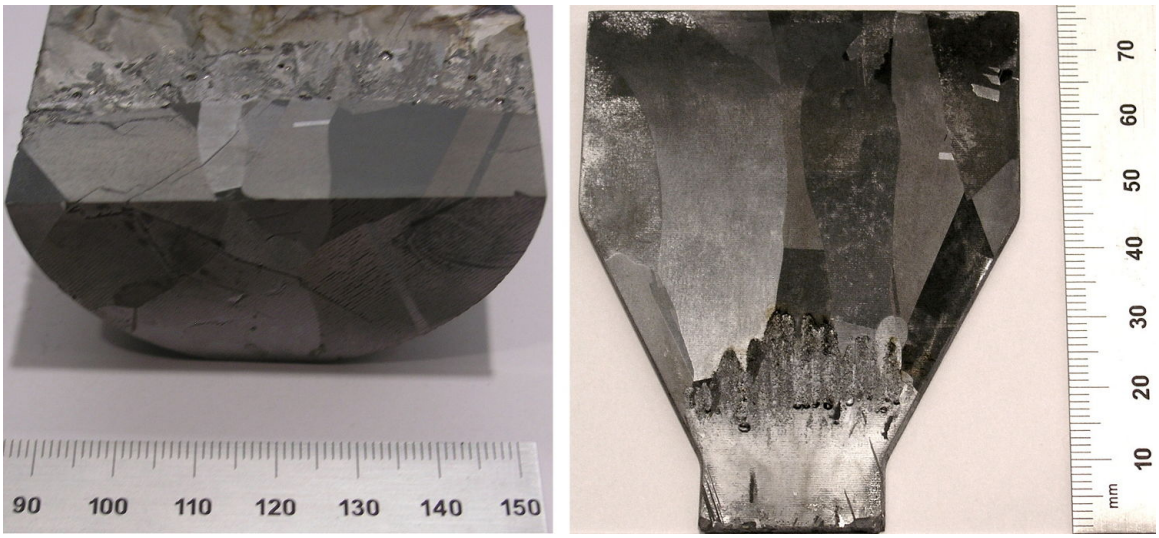

Figure 5.16: Left: The last to freeze region and final growth interface of CdTe65-8. Right: Single crystal growth was established at the seed and progressed for 15 mm before large grains appeared.

indicate large amounts of included tellurium which appears to have been trapped at the growth interface, possibly by an uneven interface surface shape. The reduced heat extraction through the ampoule base and the associated weaker temperature gradient at the growth interface appears to have caused the interface to lose integrity.

5.6 Discussion

Seeded growth experiments at 25 mm and 65 mm diamater suggest that tapered THM growth should be achievable, but it has not been demonstrated in this work.

In some experiments using CdTe, including CdTe-22, CdTe65-7 and CdTe65-8, growth has been established on a single seed crystal and progressed at least part way up the tapered region of the ampoule. Even this outward growth, though, has been accompanied by twin defects and the formation of secondary grains. These problems were made worse when experiments were attempted using CdZnTe.

Although convincing single crystals were not grown from narrow seeds, the development process offers insights into what might be required to achieve such growth. In particular the effect of the reduced seed diameter on the thermal conditions in the growth region is an important question which can be partially answered. Several other aspects of the growth technology such as surface treatments and ampoule

rotation can also be evaluated.

A flat or slightly convex growth interface is considered desireable for growth. This is generally attributed to the accumulation of impurities in depressions and outward grain propagation, but it is also related to the balance between advection and diffusion at the interface where depressions are associated with lower velocity, a thicker diffusive boundary layer, and impeded growth. Two approaches are generally suggested to reduce the occurence of a depression in the centre of the growth interface. The first is to cool the centre of the base of the ampoule as described by Dost and Liu in [38, 40]. This method was useful in the GaSb growth study that preceded the current work, and it formed the basis of attempts in the current work to extract large amounts of heat through the tapered region of the THM growth experiments. The other approach, which is to suppress convection through the use of applied magnetic fields, accelerated ampoule rotation or microgravity was not explored in this work due to time and equipment constraints. Had more successful growth been demonstrated earlier in the work, rotating magnetic fields could have been employed in an effort to grow more quickly.

The most important problem facing tapered growth is the drastic change to the thermal conditions in the ampoule during the growth process. In the present work, cooling at the base of tapered THM experiments had a similar effect to cooling at the centre of an un-tapered experiment. Unfortunately, although the rate of cooling can be chosen to achieve a suitable interface shape at the outset of growth, as the low-resistivity crystal grows thicker it becomes increasingly difficult to remove heat from the growth interface and the local temperature gradient becomes smaller. The heat flux in the support pedestals was measured during growth experiments and thermal profiling. Figure 5.17 shows that in 25 mm profiling tests the pedestal heat flux dropped by 50 percent during the first 25 mm of growth. The problem is compounded by the increasing area of the growth interface. In order to achieve a consistent temperature gradient at the interface while the diameter is increasing linearly, the total rate of heat flow through the interface would need to increase quadratically.

This drastic change in the thermal conditions can be clearly seen in the 65 mm diameter unseeded experiments shown in Figure 5.9, in which increasing heat extraction resulted in better growth in the later stages of experiments but much poorer growth at the beginning. The extreme curvature of the interface in CdTe65-6 at the point of failure indicates that all of these experiments likely suffered from very strong convection and that heat extraction was too strong rather than not strong enough.

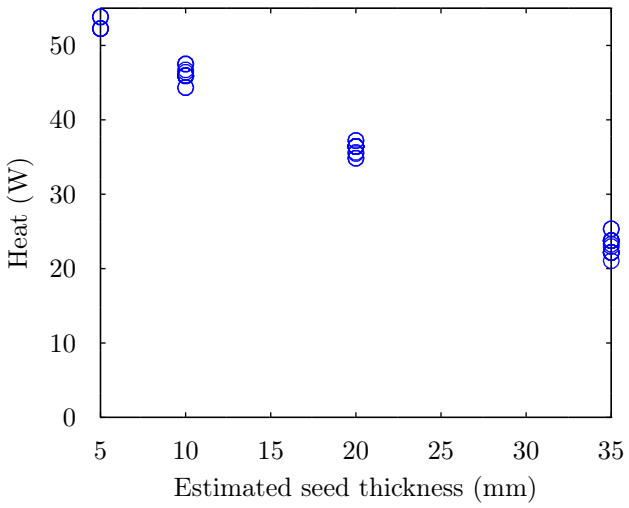

Figure 5.17: Heat flow measured in the support pedestal during thermal profiling of 25 mm experiments.

Roy, Weiler and Stein have published results of unseeded THM growth in conical ampoules at 50 mm diameter [41]. They also find a strong relationship between the thermal conditions of growth, the presence or absence of depressions in the growth interface, and the number and size of grains in the resulting ingots. A small depression in the centre of their sample is associated with a cluster of small grains extending upward through the ingot. This result is very similar to the result of CdTe65-7 in the present study.

Temperature measurements taken along the axis of a 25 mm diameter tapered THM system are shown in Figure 5.18. To take the measurements, a quartz tube was welded to the base of the ampoule and then CdTe and tellurium were placed around the tube as normal. A thermocouple was inserted and raised up and down along the axis of the ampoule, while a second thermocouple measured the temperature of the furnace wall. The measurements show a 25 K temperature span within the liquid zone and a 10 K/mm gradient within the seed crystal. The scale at right indicates the position of each reading with respect to the centre of the heat zone, and this profile was taken when the seed was approximately 10 mm thick. The extremely strong heat transfer shown in this profile was reduced as the heater was raised, with a weaker temperature gradient in the seed and a smaller range of temperatures in the solution zone.

Growth in the 65 mm furnace was more successful after seeds were added. This is likely due to the insulating effect of the seed crystal and the weaker variation of

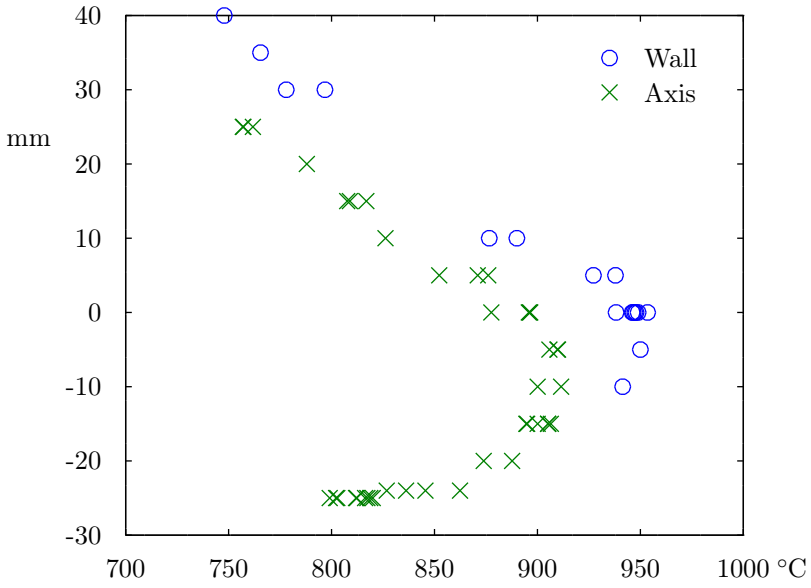

Figure 5.18: Measured wall and axis temperatures during profiling of the 25 mm THM furnace

the interfacial heat flux later in the growth process. The most successful growth experiment at this diameter was CdTe65-7, which used a very large rate of heat extraction through the seed but which suffered from a concave growth interface in the later stages. In CdTe65-8, the heat flux in the seed was reduced somewhat and quite successful outward growth was achieved for a few millimeters, but then growth broke down. Massive inclusion of tellurium in the crystal appears to have resulted from an uneven growth interface possibly due to the reduced heat flux. For this experiment the temperature gradient along the furnace wall was increased in order to cool the forming crystal during later growth, but this will not have had very much impact at the point at which the breakdown occurred. Instead it appears that large grains re-established themselves under conditions comparable to the unseeded experiments and similarly sized grains were produced.

Tapered growth at 65 mm diameter therefore proceeds in two stages. At the outset, the interface condition is sensitive to heat extracted through the seed crystal, and some outward growth of the seeds has been achieved. Within 20 mm however heat flux through the support cannot be relied upon to produce the desired interface shape and heat must be removed through the outside face of the grown crystal. This becomes increasingly difficult as the crystal diameter increases. If full tapered growth is to be achieved very careful furnace design and active control of the heat fluxes

will be required. With sufficient care, the cooling of the seed base could be increased progressively until the tapered region has been grown and sufficient thermal contact is established with the furnace walls. Growth could then proceed under conditions similar to those of the unseeded experiments. A great deal more simulation and development would be required to achieve this in practice.

At 25 mm diameter, things are slightly easier, but the results are largely the same as those at 65 mm diameter. Seeded growth proceeds for several millimetres under conditions comparable to untapered THM with cooling at the base of the seed. As the growth interface becomes larger two things happen. The temperature gradient falls sharply because of the growing seed and convection in the liquid becomes stronger due to the larger diameter. In experiments such as CdZnTe-3 this was shown to produce a badly concave growth interface, and even in the more successful experiments it generally led to failure of single-crystal growth within the first 20 mm. Nonetheless, the smaller diameter of these experiments and the associated reduced convection allowed outward growth with few additional grains in CdTe-14 and CdTe-22, and even significant growth in CdZnTe-6 and the later stages of CdZnTe-7.

This work did not significantly consider ways to suppress convection in the solution zone. Nevertheless, some accelerated ampoule rotation was used in the later experiments in an attempt to reduce asymmetry and curvature of the growth interfaces. Although intended mainly to promote axisymmetry, the rotation appears to have had a very positive effect on the overall interface shapes in CdTe65-8, CdZnTe-6 and CdZnTe-7.

Due to the limitations of the current project early seeded CdZnTe growth experiments used CdTe seeds, which were lost during the initial stages of most experiments. It is not clear what quality of crystal could have been grown on these seeds in any case due to the 0.2 percent difference in their lattice parameters, but observation of the grain structure and compositional analysis using EDS confirm that the seeds were lost. The only exception was CdZnTe-6 in which growth appears to have progressed normally in a similar fashion to the more successful seeded CdTe experiments. The small grains later in CdZnTe-6 were likely due at least in part to the lattice mismatch with the original seed, but a large enough grain was recovered to allow CdZnTe-7 to be attempted with a ternary seed crystal. The combination of ampoule rotation and a more favourable seed composition seem to have helped produce large grains in CdZnTe-7, but the result is not conclusive enough to show that tapered growth is achievable even at smaller diameters.

Both sand-blasting and carbon coating were effective at preventing wetting of CdTe experiments to the ampoules. Sand blasting was more effective for these development experiments because it allowed observation of the ampoule contents before and during growth and because it is not susceptible to scratching or flaking. Sand-blasted ampoules were most effective at retaining their seed crystals, and they were easily reusable after etching with aqua regia. In contrast, ampoules fully coated with pyrolized graphite were vulnerable to scratching during loading procedures. They were also opaque, which prevented verification that the seed crystal had been sufficiently wetted by the solution zone. This is not a problem in production-scale THM growth, but for development experiments in which parameters change significantly from trial to trial it makes things more difficult. Graphite coatings also had to be re-applied between experiments. For these reasons, sand blasting is recommended as a surface treatment for future research experiments, particularly for CdTe growth.

Seeds were lost in many growth experiments, especially in the 25 mm seeded CdZnTe growth study with carbon-coated ampoules. 10 mm thick seeds were too thin to reliably establish growth. More success was achieved in experiments with sand-blasted or untreated quartz in the seed pocket and when taller seeds were used in late experiments such as CdTe65-7 and CdTe65-8. In these seeded 65 mm diameter experiments, the 25 mm diameter seeds were retained, and growth was established at least for a short distance before multiple grains appeared.

5.7 Conclusion

Tapered single crystal growth has been attempted for CdTe at 25 mm and 65 mm diameter and for CdZnTe at 25 mm diameter. Unfortunately, despite successful GaSb growth of single crystals from small seeds in the preliminary studies, this success was not replicated with tellurides except in very limited cases. The best crystals grown at 25 mm diameter from both materials are dominated by a single grain structure, but with large secondary grains and twin defects. Seeded growth at 65 mm diameter showed outward growth that broke down after less than 20 mm.

The experimental study does suggest that such growth is possible under ideal conditions. This would, require active control of the heat transfer out of the bottom of the seed to ensure stable conditions during growth through the tapered region. A lengthy optimization process would be required to implement this process, and this was not possible within the time frame of the current work.

Growth from 10 mm seeds was most successful when sand-blasted ampoules were used. This surface finish prevented wetting of the tellurium and CdTe while allowing observation of the ampoule contents. Fewer seed crystals were lost in experiments processed in sand-blasted ampoules compared to carbon-coated ampoules.

The use of crushed source material does not appear to have affected the effectiveness of the THM growth. The most successful growth experiments were conducted with crushed source material and resulted in void-free crystals. There is a risk that the downward consolidating pass of the tellurium solution may sweep impurities toward the seed crystal, but this was not observed in this work.

Ampoule rotation greatly improved the uniformity of the growth interface and also reduced its curvature.

Nucleation of large grains could not be achieved in unseeded experiments due to supersaturation of the tellurium solution. The behaviour of the first to freeze material in THM experiments appears to be similar to that of superheated (fully dissociated) CdTe melts in VGF. Larger cooling rates at the base of unseeded experiments were associated with poorer initial growth but larger grains later.

Chapter 6

Finite Element Simulation of THM Growth Experiments

6.1 Introduction

THM experiments are very time-consuming and very expensive. A typical growth experiment with 65 mm diameter might require one week of preparation, four weeks of growth, and two weeks or more for cutting and analysis. In addition to the time and equipment required, the polycrystalline source, single crystal seed, quartz ampoule and lab chemicals can easily cost over $5000 for a single experiment. It makes sense, therefore, to learn as much as possible from each growth experiment, and to choose experimental parameters that maximize the chances of successful growth.

In order to inform and improve the experimental study, a model has been developed to simulate the environment inside the THM growth ampoule. The purpose of the model is to predict the conditions at the growth interface based on the temperatures measured outside the ampoule. Knowing this relationship, the temperature gradients inside the furnace can be adjusted and cooling can be applied to the ampoule base so as to produce the most favourable growth conditions possible.

During the experimental study, the temperature field in the THM system was first simulated using ANSYS CFX. This model suggested that the interface might be favourable, but it was simplistic and attempts to integrate explicit interface tracking and thermosolutal convection failed. A finite element model was therefore developed from first principles and implemented first in Matlab and then later in C++ using the Deal.II library. This model took several years to develop to the point where it could

make predictions about the THM growth system. Unfortunately, it could therefore be used only to analyze past experiments and not to make anything more than very rough predictions before experiments could be carried out. Nonetheless, the model described here is a significant component of the overall study. Using new approaches to model the interface motion and the ternary phase diagram, it shows that tapered ampoules generally lead to the same growth structures as non-tapered ampoules with the same attendant challenges due to heat transfer and convection.

The model developed in this study is unique to the best of the author's knowledge. It is an axisymmetric finite element approximation to the temperature, velocity, composition, and phase in the combined liquid and solid domains occupied by the ternary mixture. The level set method is used to track sharp planar boundaries between solid and liquid. The approach used in this work to model the moving interfaces using a fixed grid is referred to in this report as enrichment by virtual interface elimination (EVIE). It is based upon work by others to model the solidification of pure metals, and this model adapts their technique and extends it to dissolution problems where the rate of dissolution or solidification is limited by mass transport rather than heat flux. By containing the total behaviour of the solid and liquid ternary solution within a single finite element, this model offers a way to integrate such materials seamlessly into global finite element models with no need for moving meshes or explicit front-tracking. It also makes adaptive meshing very simple to implement. Although the model came too late to reliably inform the experimental study, it nonetheless represents a valuable tool for modelling solution processes in the future.

In this chapter, the EVIE model will first be presented in detail. Simulation results will then be presented for the dissolution experiments of Section 4.5 and for THM growth. Although the model was completed too late to significantly inform the experimental study, recommendations are made for future experiments.

6.2 The Enriched Finite Element Model

6.2.1 Governing Equations for the Stefan-Type Problem

The dissolution and solidification of ternary mixtures is a complex problem with many variables. It may, however, be viewed as a superposition of two simpler problems. In short, temperature and velocities are related by a model of quasi-steady incompressible flow driven by thermosolutal convection. Meanwhile, the interface position and solution composition are related through a Stefan-type transient mass transport model. The convection model and the mass transport model are coupled and must be solved concurrently. In this work, the two models are solved in the same domain using the same computational mesh and finite element interpolation functions.

The essential relationships of the variables and equations at play in this model are summarized in Figure 6.1. In brief, the quasi-steady state temperature and velocity fields are calculated based on the initial condition in the domain. The composition and interface positions are calculated using the level set method (LSM) and integrated in time using fully implicit backwards-Euler time stepping. Occasionally, the temperature field is recalculated from the applied wall temperatures, accounting for the motion of the interfaces and the energy transported by advection. The temperature and mole fraction fields are then used to update the velocity field. Time integration of the mass transport model then resumes with the new velocity and temperatures. Although the temperature and velocity fields are referred to as quasi-steady, their evolution is acually implemented using implicit time integration, with less frequent updating than the mass transport model. It was originally hoped that a steady state model for temperature and velocity could be used, but the sensitivity of the velocity field to the solutal body force made implicit time stepping necessary.

The domain, Ω, for the model includes the entire volume containing the ternary mixture of Te, CdTe, and ZnTe. It is bounded by a closed boundary Γ_W and an axis of symmetry Γ_S. The domain volume is divided into any number of solid or liquid subdomains Ω_s and Ω_l, which are separated by sharp interfaces Γ_I. Examples of such domains and their boundaries can be seen in Figure 6.6.

The velocity in the solid regions is assumed to be zero. That is, solid does not float about inside the solution, but rather it forms or recedes on the walls of the liquid domain. Consider therefore the liquid in a single subdomain Ω_l, which has a

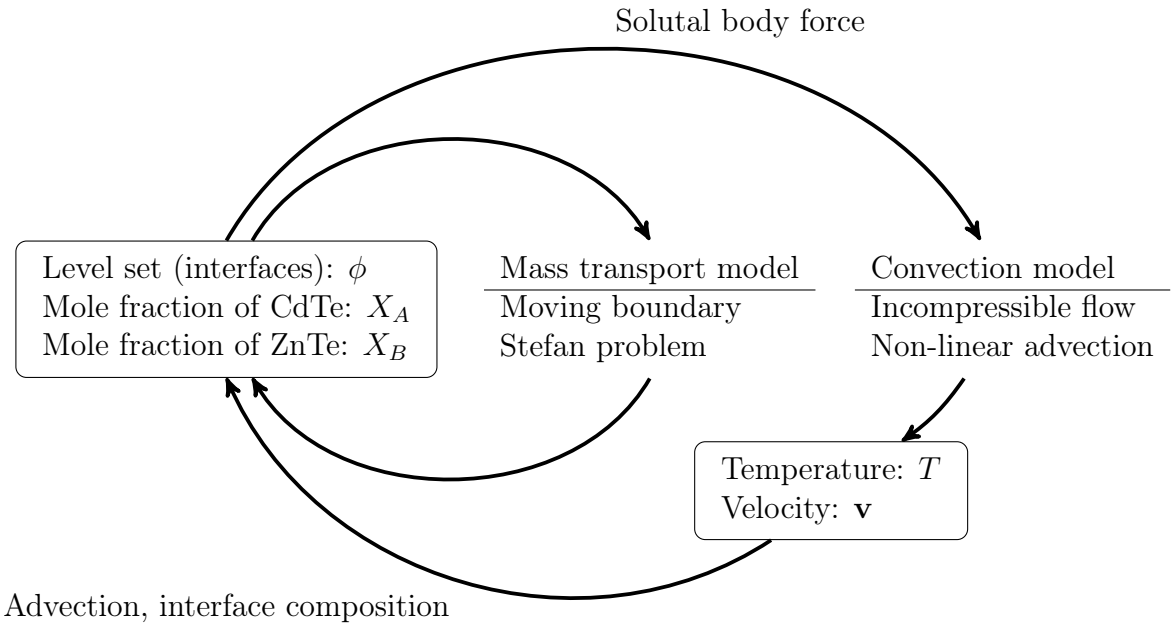

Figure 6.1: Relationship of the steady thermo-solutal convection model and the transient mass transport model.

symmetry-type boundary Γ_s and a no-slip boundary Γ_v such that

$$\Omega_l \in \Omega \qquad \Gamma_v \in (\Gamma_I \cup \Gamma_W) \qquad \Gamma_s \in \Gamma_S. \tag{6.1}$$

The velocity in the liquid subdomain will be governed by the balance of linear momentum, expressed first in its stress-divergence form.

$$\frac{D\rho\boldsymbol{v}}{Dt} = \operatorname{div}\sigma + \rho\boldsymbol{f} \qquad \text{in } \Omega_l \tag{6.2}$$

Here ρ is the fluid density, $\boldsymbol{v}$ is the velocity, σ is the internal stress, and $\boldsymbol{f}$ is a volumetric body force. We begin by assuming that the fluid is incompressible and Newtonian so that the stress tensor is composed of a normal pressure, p, and a shear part which is proportional to the symmetric deformation rate tensor, d, with the kinematic viscosity ν. Then we apply the well-known Boussinesq approximation and consider density to be constant except where it affects the strength of the body force.

$$\frac{D\boldsymbol{v}}{Dt} = \operatorname{div}\left(2\nu d - \frac{1}{\rho}pI\right) + \boldsymbol{f} \tag{6.3}$$

The left hand side of the momentum equation represents the material derivative of the velocity vector. It is composed of a partial time derivative and an advection term.

$$\frac{D\boldsymbol{v}}{Dt} = \dot{\boldsymbol{v}} + \operatorname{grad}(\boldsymbol{v})\boldsymbol{v} \tag{6.4}$$

The right hand side can be regrouped after expanding the deformation rate tensor.

$$\operatorname{div}\left(\nu\left(\operatorname{grad}(\boldsymbol{v}) + \operatorname{grad}(\boldsymbol{v})^T\right) - \frac{1}{\rho}pI\right) = \nu \operatorname{div}\operatorname{grad}\boldsymbol{v} + \operatorname{grad}\left(\nu \operatorname{div}\boldsymbol{v} - \frac{1}{\rho}p\right) \tag{6.5}$$

The body force results from density changes due to temperature and composition variation.

$$\boldsymbol{f} = (\beta_T(T - T_0) + \beta_A(C_A - C_{A0}) + \beta^B(C_B - C_{Bo}))g\boldsymbol{e_z} \tag{6.6}$$

The solutal expansivities are defined in terms of mass concentration, so these must be calculated from the mole fraction using the relevant atomic masses.

$$C_A = \frac{m_A}{m} = \frac{M_A X_A}{M_A X_B + M_B X_B + M_{\mathrm{Te}}(1 - X_A - X_B)} \tag{6.7}$$

$$C_B = \frac{m_B}{m} = \frac{M_A X_B}{M_A X_B + M_B X_B + M_{\mathrm{Te}}(1 - X_A - X_B)} \tag{6.8}$$

The momentum equation relates the three velocity components as well as the pressure. The system requires an additional constraint to be solvable. This is the continuity condition which completes the incompressible Navier Stokes equations.

$$\operatorname{div}\boldsymbol{v} = 0 \tag{6.9}$$

There are several formulations that can be used to solve the momentum equation under the constraint of incompressibility. In the p-v formulation, for example, the momentum and continuity equations are simply discretized together and solved concurrently for the four variables. Frequently, however, the pressure field is not of interest, and it can be eliminated from the system by means of a penalty formulation. Such a formulation begins by choosing pressure to be a Lagrange multiplier for the continuity constraint. Eq. 6.9 is therefore modified to allow slight compressibility.

$$\operatorname{div}\boldsymbol{v} = -\frac{p}{\rho\lambda} \tag{6.10}$$

The penalty parameter λ is chosen to be arbitrarily large. As it becomes larger, the continuity condition is enforced more strictly and the fluid motion is driven to be isochoric. At very large values, however, the equations become ill-conditioned. A variation of this formulation is the recursive penalty method, in which the pressure is first estimated from a previous velocity state using Eq. 6.9, and then corrected using the penalty parameter.

$$p = p^{n-1} - \rho\lambda \operatorname{div} \boldsymbol{v} \tag{6.11}$$

This formulation requires that the pressure be approximated along with the velocity field, but the approximation is a posteriori and the momentum equations can be solved using smaller values of λ. For the purpose of developing the model, the recursive penalty formulation also has the advantage that it retains all of the terms for both the p-v method and the penalty formulation so that either model can be obtained simply by dropping terms from the final equations.

Including the recursive penalty terms and expanding the deformation rate tensor and the material derivative, the final form of the momentum equation can be written for the liquid volume. For clarity, it is repeated using Cartesian indices, although this model will be developed in cylindrical coordinates.

$$\dot{\boldsymbol{v}} + \operatorname{grad}(\boldsymbol{v})\boldsymbol{v} = (\lambda + \nu) \operatorname{grad} \operatorname{div} \boldsymbol{v} - \frac{1}{\rho} \operatorname{grad} p^{n-1} + \nu \operatorname{div} \operatorname{grad} \boldsymbol{v} + \boldsymbol{f} \quad \text{in } \Omega_l \tag{6.12}$$

$$\dot{v}_i + v_{i,j} v_j = (\lambda + \nu) v_{j,ji} - \frac{1}{\rho} p^{n-1}_{,i} + \nu v_{i,jj} + f_i$$

The liquid domain is fully enclosed by no-slip walls, so the boundary conditions of the momentum equation are Dirichlet. The motion of the solid-liquid interfaces is assumed to be negligible compared to the fluid velocity.

$$\boldsymbol{v} = \boldsymbol{0} \qquad \text{on } \Gamma_v \tag{6.13}$$

The temperature field is governed by the energy equation, which balances the change in internal energy, ϵ, with the internal stress work, the heat flux $\boldsymbol{q}$, and a volumetric heat source $\dot{q}$.

$$\rho \frac{D\epsilon}{Dt} = \sigma : \operatorname{grad} \boldsymbol{v} + \operatorname{div} \boldsymbol{q} + \rho\dot{q} \tag{6.14}$$

The flow field, driven by natural convection, is not strong enough to produce significant viscous heating, and there is no volumetric heat source in this system. Neglecting the Dufour effect, we assume that the heat flux is governed as usual by Fourier's law of conduction and the internal energy is proportional to temperature. These assumptions give the advection-diffusion energy equation for the liquid domain. The equivalent equation for the solid is obtained simply by eliminating the advection term.

$$\dot{T} + \boldsymbol{v} \cdot \operatorname{grad} T + \frac{k}{\rho c_p} \operatorname{div}(\operatorname{grad} T) = 0 \qquad \text{in } \Omega_l \tag{6.15}$$

$$\dot{T} + \frac{k_s}{\rho_s c_{p,s}} \operatorname{div}(\operatorname{grad} T) = 0 \qquad \text{in } \Omega_s \tag{6.16}$$

On the solid-liquid interfaces heat is generated when the solid dissolves or solidifies. The effect of this latent heat on temperature is accounted for through the energy equation's jump condition, which is written for a boundary with velocity $\boldsymbol{u}$ and a normal vector, $\boldsymbol{n}$ directed into the liquid.

$$[\![(\rho\epsilon + \tfrac{1}{2}\boldsymbol{v} \cdot \boldsymbol{v})(\boldsymbol{v} - \boldsymbol{u}) - \sigma\boldsymbol{v} - \boldsymbol{q}]\!] \cdot \boldsymbol{n} = 0 \tag{6.17}$$

At the solid-liquid interfaces, we again neglect stress work and kinetic energy. The interfacial liquid is at rest, and the solid is growing or dissolving so that the interface moves toward the liquid with normal velocity $u_n = \boldsymbol{u} \cdot \boldsymbol{n}$. The normal heat fluxes from the liquid into the interface and from the interface into the solid are again proportional to the respective normal temperature gradients and the solid and liquid thermal conductivities, and the jump in internal energy is the latent heat h_L. The energy balance for the interface can now be written from Eq. 6.17.

$$h_L u_n = k_s \operatorname{grad}_n(T)^s - k_l \operatorname{grad}_n(T)^l \qquad \text{on } \Gamma_I \tag{6.18}$$

This relation is commonly referred to as the energy Stefan condition. That is, the latent heat released by dissolved solid at the interface is balanced by a jump in the normal heat flux. When modelling solidification or melting problems, this heat absorbtion is the effect that limits the rate of the phase change. A common solution technique, therefore, is to calculate the normal interface velocity from the temperature field using Eq. 6.18, advance the interface, and then recalculate the temperature field. In this model, by contrast, the interface velocity is determined not by the heat flux but from the flux of solute to and from the interface. Eq. 6.18 is used in this model

to determine the interface temperature rather than the dissolution velocity.

Following the approach used by Dost and Liu, the boundary condition for the ampoule walls Γ_W is assumed to have a convective form [40].

$$\boldsymbol{q} \cdot \boldsymbol{n} = -k \operatorname{grad} T \cdot \boldsymbol{n} = h(T - T_\infty) \qquad \text{on } \Gamma_W \tag{6.19}$$

The heat transfer coefficient, h, must be chosen to best account for convection, conduction and radiation. Different portions of the wall will have different values for both h and T_∞, and these must be measured in the experimental system or adjusted to fit the experimental results.

The mass transport equations for the two solutes CdTe and ZnTe are solved only in the liquid subdomains. The transport equation is a conservation law for the number of solute molecules. We assume the solution mole density $\bar{\rho}$ to be constant. The time rate of change of the mole fraction of CdTe, X_A, is then proportional to the divergence in its solute flux.

$$\frac{D\bar{\rho}X_A}{Dt} = \operatorname{div} \boldsymbol{i_A} \qquad \text{in } \Omega_l \tag{6.20}$$

We neglect the Soret effect and assume that the solute flux is proportional to the mole fraction gradient, with diffusion coefficient D_A. Then, expanding the material derivative we get the advection-diffusion transport equation for the liquid domain. The same equation holds for either solute species.

$$\dot{X}_\gamma + \operatorname{grad} X_\gamma \cdot \boldsymbol{v} + D_\gamma \operatorname{div}(\operatorname{grad} X_\gamma) = 0 \qquad \gamma = A, B \tag{6.21}$$

The motion of the solid-liquid interface is determined through the jump condition for the mass transport equations.

$$[\![\bar{\rho}(\boldsymbol{v} - \boldsymbol{u}) - \boldsymbol{i}]\!] \cdot \boldsymbol{n} = 0 \qquad \text{on } \Gamma_I \tag{6.22}$$

As for the energy equation, neglecting the fluid velocity yields a Stefan condition relating the interface velocity to the solute mass transport in the liquid.

$$(X_\gamma^s - X_\gamma^l)u_n = D_\gamma \operatorname{grad}_n X_\gamma \qquad \gamma = A, B \tag{6.23}$$

The solid and liquid mole fractions are obtained from logistic and polynomial

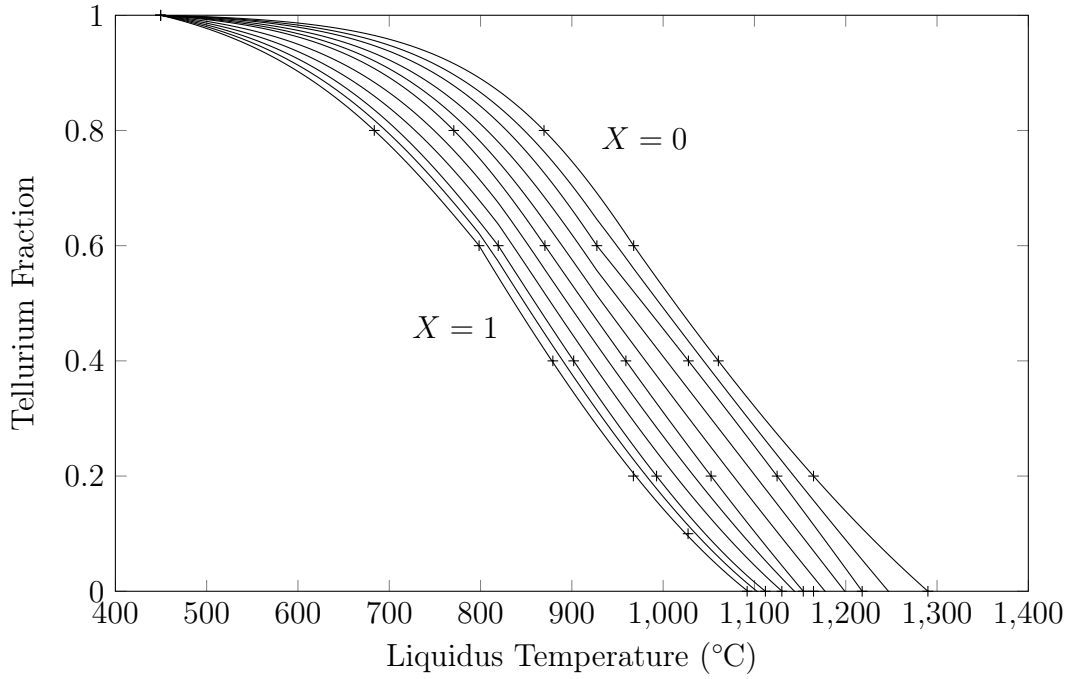

Figure 6.2: Liquidus tellurium content of a Te - $Cd_XZn_{1-X}Te$ mixture as a function of interface temperature and X. Curves are approximated by least-squares to data from [9].

approximations fit to the equilibrium phase diagram data published by Steininger et. al. [9]. The tellurium content of the interfacial liquid is expressed as a function of temperature for several ratios of CdTe to ZnTe. The resulting function is plotted in Figure 6.2, and linear interpolatian is used for compositions that fall between the curves. This function gives the X_γ^l values required by Eq. 6.23. X_γ^s is either known from the previous time step or determined based on the relative solute fluxes depending on whether the solid is growing or shrinking at the interface.

To track the position of the solid-liquid interfaces, the LSM is used. A scalar field is therefore defined which represents the signed normal distance of any point from the interface.

$$\phi(\boldsymbol{x}, t) = \min_{\bar{\boldsymbol{x}} \in \Gamma_I} \|\boldsymbol{x} - \bar{\boldsymbol{x}}\| \operatorname{sgn}[\boldsymbol{n} \cdot (\boldsymbol{x} - \bar{\boldsymbol{x}})] \tag{6.24}$$

The value of the level set therefore demarcates the liquid and solid subdomains.

$$\phi > 0 \ \text{ in } \Omega_s \qquad \phi = 0 \ \text{ on } \Gamma_I \qquad \phi < 0 \ \text{ in } \Omega_l \tag{6.25}$$

Finally, the level set evolves based on the motion of the interface. Because ϕ represents the signed normal distance of any point from the interface itself, the normal projection of its gradient must always be unitary and the interface velocity is equivalent to the local time derivative of ϕ.

$$u_n |\operatorname{grad} \phi| = -\dot{\phi} \tag{6.26}$$

The interface velocity itself is obtained from the solute transport model through Eq. 6.23.

6.2.2 Material Properties

Material properties relevant to THM growth of tellurides are generally well established and are adopted from the values used by other authors. The exception is the diffusivity, which was measured experimentally as described in Section 4.5. The measured diffusivity is twice as large as the value reported in other simulation work.

Table 6.1: Material properties used in THM simulations

Parameter	Symbol	Values
Density of liquid	ρ	$5.62\,\mathrm{g/cm^3}$
Density of solid CdTe	ρ_s	$6.4\,\mathrm{g/cm^3}$
Thermal Conductivity of liquid	k	$5.7\,\mathrm{W/mK}$
Thermal Conductivity of solid	k_s	$3.8\,\mathrm{W/mK}$
Specific heat capacity of liquid	c_p	$0.372\,\mathrm{J/gK}$
Specific heat capacity of solid	$c_{p,s}$	$0.16\,\mathrm{J/gK}$
Kinematic viscosity	ν	$0.16\,\mathrm{mm^2/s}$
Thermal expansion coefficient	β_T	$8.0 \times 10^{-5}\,\mathrm{K^{-1}}$
Solutal expansion coefficient	β_C	0.056
Thermal Diffusivity of liquid	α	$2.73\,\mathrm{mm^2/s}$
Diffusivity of CdTe, ZnTe	D	$0.008\,\mathrm{mm^2/s}$
Prandtl Number	Pr	0.06
Latent Heat	h_L	$209.0\,\mathrm{J/g}$
Ampoule radius	R	$25,65\,\mathrm{mm}$
Solution zone height	H	$20,50\,\mathrm{mm}$

6.2.3 Discretization by Weighted Residuals

The continuum equations presented in Section 6.2.1 cannot be solved analytically for the general case. A general discretization process will be presented here using weighted residuals, and then the particular assumptions will be discussed that lead to the final Bubnov-Galerkin finite element discretization.

In all discretizations, the continuous functions must be approximated by linear combination of N basis functions. The problem then becomes to choose the coefficients of the approximation so as to satisfy the governing equation as closely as possible in an integral sense. These coefficients become the vertices of the computational grid. They may or may not correspond to specific points in space.

$$\begin{aligned}
\hat{\boldsymbol{v}} &= \sum_{i=1}^{N} \boldsymbol{v}_i N_i \approx \boldsymbol{v} \\
\hat{T} &= \sum_{i=1}^{N} T_i N_i \approx T \\
\hat{\phi} &= \sum_{i=1}^{N} \phi_i N_i \approx \phi \\
\hat{X}_A &= \sum_{i=1}^{N} X_{Ai} N_i \approx X_A \\
\hat{X}_B &= \sum_{i=1}^{N} X_{Bi} N_i \approx X_B
\end{aligned} \tag{6.27}$$

The basis functions, N_i, control the way the global approximations depend on the vertex values. It is typical to choose shape functions which each have value 1 at one spatial vertex and value 0 at all other vertices. In such a case, the value of each computational vertex represents the global approximation's value at the corresponding point in space.

Following the method of weighted residuals, we recognize that the approximation functions cannot be made to satisfy the governing equations exactly unless the basis functions themselves solve them. Since the purpose of discretization is to avoid having to solve the governing equations analytically, we instead choose generic shape functions and weaken the requirements of the governing equations. The equations are put in a weak form through the introduction of test functions.

The remainder of this development will focus on the approximation functions,

and the hats will be dropped for the sake of clarity. To further simplify notation, the following bilinear form will be used to represent the integration of a product of fields over a volume. When the arguments are vectors, the scalar product is implied.

$$(a,b)_\Omega \equiv \int_\Omega ab\,\mathrm{d}V \qquad\qquad (\boldsymbol{a},\boldsymbol{b})_\Omega \equiv \int_\Omega \boldsymbol{a}\cdot\boldsymbol{b}\,\mathrm{d}V \tag{6.28}$$

Using this notation, we form a residual by applying Eq. 6.12 to the velocity approximation function. We then multiply the residual by a scalar-valued test function, w, and integrate the product over the liquid domain.

$$\left(\frac{D\boldsymbol{v}}{Dt} - \operatorname{grad}\left((\lambda+\nu)\operatorname{div}\boldsymbol{v} - \frac{1}{\rho}p^{n-1}\right) - \nu\operatorname{div}\operatorname{grad}\boldsymbol{v} - \boldsymbol{f}, w\right)_{\Omega_l} = \boldsymbol{0} \tag{6.29}$$

The strong form of the momentum equation demands that the velocity field conserves momentum locally. This weak form, by contrast, insists that the approximation function conserves momentum only in an integral sense over the entire domain.

Integration by parts can now be used to reduce the order of the differential equation.

$$\begin{aligned}\left(\frac{D\boldsymbol{v}}{Dt}, w\right)_{\Omega_l} &- \int_{\Omega_l} \operatorname{grad}\left(w\left((\lambda+\nu)\operatorname{div}\boldsymbol{v} - \frac{1}{\rho}p^{n-1}\right)\right) + \operatorname{div}\left(\nu w\operatorname{grad}\boldsymbol{v}\right)\mathrm{d}V \\ &+ \left((\lambda+\nu)\operatorname{div}\boldsymbol{v} - \frac{1}{\rho}p^{n-1}, \operatorname{grad} w\right)_{\Omega_l} \\ &+ \left(\nu\operatorname{grad}\boldsymbol{v}, \operatorname{grad} w\right)_{\Omega_l} - \left(\boldsymbol{f}, w\right)_{\Omega_l} = \boldsymbol{0}\end{aligned} \tag{6.30}$$

Finally, divergence theorem is applied to move terms to the boundary, giving the final weak form of the momentum equation.

$$\begin{aligned}&\left(\dot{\boldsymbol{v}} + \operatorname{grad}(\boldsymbol{v})\boldsymbol{v} - \boldsymbol{f}, w\right)_{\Omega_l} + \left((\lambda+\nu)\operatorname{div}\boldsymbol{v} - \frac{1}{\rho}p^{n-1}, \operatorname{grad} w\right)_{\Omega_l} \\ &\quad + \nu\left(\operatorname{grad}\boldsymbol{v}, \operatorname{grad} w\right)_{\Omega_l} - \int_{\Gamma_s} w\left(\left((\lambda+\nu)\operatorname{div}\boldsymbol{v} - \frac{1}{\rho}p^{n-1}\right)I + \nu\operatorname{grad}\boldsymbol{v}\right)\mathrm{d}\boldsymbol{A} \\ &\quad = \boldsymbol{0}\end{aligned} \tag{6.31}$$

Eqs. 6.16, 6.21 and 6.26 are similarly put into weak form, the heat and mass flux boundary conditions are applied.

$$\left(\dot{T} + \operatorname{grad} T\cdot\boldsymbol{v}, w\right)_\Omega + \alpha\left(\operatorname{grad} T, \operatorname{grad} w\right)_\Omega + \int_{\Gamma_W} \frac{wh}{\rho c_p}(T - T_\infty)\,\mathrm{d}A = 0 \tag{6.32}$$

$$\Big(\dot{X}_\gamma + \operatorname{grad} X_\gamma \boldsymbol{v}, w\Big)_{\Omega_l} + D_\gamma \Big(\operatorname{grad} X_\gamma, \operatorname{grad} w\Big)_{\Omega_l} = 0 \tag{6.33}$$

$$\Big(u_n |\operatorname{grad} \phi| + \dot{\phi}, w\Big)_{\Omega} = 0 \tag{6.34}$$

The boundary terms are simply weighted integrals of the heat, mass and momentum fluxes out of the domain.

Comparing Weighted-Residual Discretizations

The use of approximation functions and weighted residuals can lead to a broad family of discretization schemes. The difference between the methods comes from the choice of the basis functions and the test functions. Spectral methods such as Fourier series use basis functions and test functions that are defined continuously throughout the domain. The volume and boundary integrals therefore must be carried out globally for all of the basis functions. Most methods, however, limit the domain of each basis function so that the volume integrals are carried out over smaller regions and boundary integrals are necessary only for the few functions that are non-zero at the domain boundary. Several weighted residuals methods are listed briefly in Table 6.2.

Table 6.2: Basis and test functions used for several weighted residuals formulations.

Method	Basis Functions	Test Functions	Integration
Fourier Series	Sinusoidal	1	Global
Collocation Method	Global polynomial	$\delta(x - x_i)$	Point-wise
Least Squares Method	Local Polynomial	1	Point-wise
Finite Volume Method	Piecewise Constant	1	Sub-volumes
Finite Element Method	Local polynomial	Local polynomial	Sub-volumes

Two methods are of particular interest in the context of transport modelling. These are the finite volume method (FVM) and the finite element method (FEM). Either method can be derived from Galerkin weighted residuals or from other physical arguments. Generally, to mathematicians both methods are special cases of the weighted residual method for approximating the solutions to partial differential equations. To engineers, on the other hand, weighted residuals formulations form a subset of finite element and finite volume methods for modelling physical systems. The position of this model from the perspective of mathematics or of engineering is summarized in Figure 6.3.

The finite element model developed here is based on the Galerkin approach to

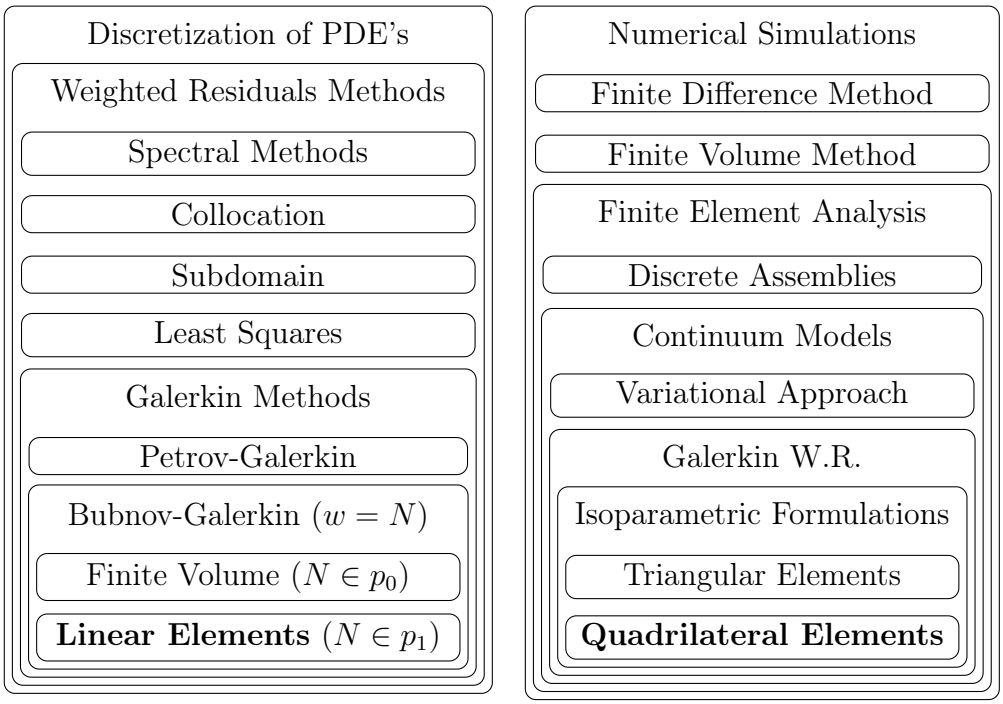

Figure 6.3: Within applied mathematics (left), linear finite elements form a subset of Bubnov-Galerkin weighted residuals methods for approximating the solutions of partial differential equations. Within engineering (right), weighted-residuals formulations are often presented as a branch within finite element analysis. Numerical simulations can also be developed through physical arguments from assemblies of simple bodies or by applying balance laws directly to small volumes.

weighted residuals. In Galerkin methods, the basis functions and the test functions are of the same type (polynomials of the same degree). Further, this model is a Bubnov-Galerkin model because the basis functions themselves are used as the test functions.

Finite Volume Method

When the finite volume method is derived from weighted residuals, the approximation function is piecewise-constant. The domain is divided into cells, each of which contains a single unitary basis function.

$$N^{(e)}(\boldsymbol{x}) = \begin{cases} 1 & \boldsymbol{x} \in \Omega^{(e)} \\ 0 & \text{else} \end{cases} \tag{6.35}$$

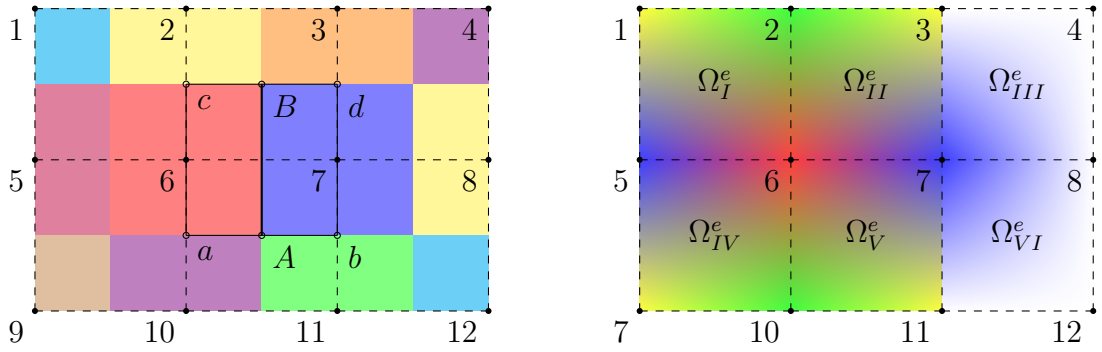

Figure 6.4: Piecewise-constant shape functions for the finite volume method, and linear shape functions for the finite element method

The coefficients of the temperature approximation, say, are then the values $T^{(e)}$, each of which represents the temperature in the volume cell $\Omega^{(e)}$.

$$\hat{T}(\boldsymbol{x}) = \sum_{e=1}^{N_e} T^{(e)} \delta(\boldsymbol{x} \in \Omega^{(e)}) \tag{6.36}$$

Following the Galerkin approach, the same shape functions are used as the test functions, and the weak governing equation is integrated over each volume. Because the basis functions are constant over each volume, the system is simplified considerably. For example, the energy equation has only two integral terms.

$$\sum_{e=1}^{N^{(e)}} \int_{\Omega^{(e)}} \dot{T}^{(e)} \, \mathrm{d}V + \sum_{e=1}^{N^{(e)}} \int_{\Gamma^{(e)}} (\alpha \operatorname{grad} T^{(e)} + T^{(e)} \boldsymbol{v}) \cdot \mathrm{d}\boldsymbol{A} = 0 \tag{6.37}$$

The piecewise-constant shape values of the finite volume method are illustrated in Figure 6.4, as well as the way by which function gradients can be estimated along the boundaries of the subdomains. Taking a volume that overlaps two subdomains, such as the rectangle $\underline{abcd}$, the function value and outward normal vector are integrated together around this volume's boundary. The average gradient inside the volume can then be obtained from the divergence theorem, and this is used for the boundary AB. For a rectangular grid, the finite volume gradient approximations reduce to finite differences between the neighbouring vertices.

In curvilinear or distorted grids the integrals are more involved, but the problem remains purely geometric. A major advantage of the FVM is that geometric transformations can be applied algebraically to standard cell templates, and therefore the

equations do not need to be integrated explicitly in software. This means that cell-for-cell, the FVM is much faster than higher order Galerkin FEM. The penalty, however, is that some derivative terms are lost due to the piecewise-constant shape functions. More cells are therefore required to achieve the same error with a FVM discretization than with a higher order methods.

Bilinear Finite Elements

This model uses bilinear elements, which are one degree higher than the FVM and better able to approximate the behaviour of the second order governing PDE's. Constructing the weak forms of the governing equations reduces them to first order differential equations. It therefore makes intuitive sense to chose approximation functions with non-zero first derivatives. These bilinear shape functions are illustrated in Figure 6.4.

As before, the basis functions N_i are used as the test functions. The integrals in the weak equations can then be expanded using cylindrical coordinates. In doing so we recall that the derivatives of the cylindrical basis vectors are non-zero. Some select terms for vectors and scalars are defined below.

$$\mathbf{v} = v_i \mathbf{e}_i = v_r \mathbf{e}_\varphi + v_\varphi \mathbf{e}_\varphi + v_z \mathbf{e}_z \tag{6.38}$$

$$\operatorname{grad} \phi = \phi_{,r} \mathbf{e}_r + \tfrac{1}{r} \phi_{,\varphi} \mathbf{e}_\varphi + \phi_{,z} \mathbf{e}_z \tag{6.39}$$

$$\operatorname{grad} \mathbf{v} = (v_i \mathbf{e}_i)_{,j} \otimes \mathbf{e}_j \tag{6.40}$$

$$\begin{aligned} &v_{r,r}\mathbf{e}_r \otimes \mathbf{e}_r + \tfrac{1}{r}(v_{r,\varphi} - v_\varphi)\mathbf{e}_r \otimes \mathbf{e}_\varphi + v_{r,z}\mathbf{e}_r \otimes \mathbf{e}_z + \\ = &v_{\varphi,r}\mathbf{e}_\varphi \otimes \mathbf{e}_r + \tfrac{1}{r}(v_{\varphi,\varphi} + v_r)\mathbf{e}_\varphi \otimes \mathbf{e}_\varphi + v_{\varphi,z}\mathbf{e}_\varphi \otimes \mathbf{e}_z + \\ &v_{z,r}\mathbf{e}_z \otimes \mathbf{e}_r + \tfrac{1}{r} v_{z,\varphi}\mathbf{e}_z \otimes \mathbf{e}_\varphi + v_{z,z}\mathbf{e}_z \otimes \mathbf{e}_z \end{aligned}$$

$$\operatorname{div} \mathbf{v} = \operatorname{tr}(\operatorname{grad} \mathbf{v}) = v_{r,r} + \tfrac{1}{r}(v_{\varphi,\varphi} + v_r) + v_{z,z} \tag{6.41}$$

$$\begin{aligned} \operatorname{grad}(\mathbf{v})\mathbf{v} = &(v_{r,r}v_r + \tfrac{1}{r}(v_{r,\varphi} - v_\varphi)v_\varphi + v_{r,z}v_z)\mathbf{e}_r + \\ &(v_{\varphi,r}v_r + \tfrac{1}{r}(v_{\varphi,\varphi} + v_r)v_\varphi + v_{\varphi,z}v_z)\mathbf{e}_\varphi + \\ &(v_{z,r}v_r + v_{z,\varphi}v_\varphi + v_{z,z}v_z)\mathbf{e}_z \end{aligned} \tag{6.42}$$

$$\begin{aligned} \operatorname{grad}\mathbf{v} \operatorname{grad}\phi = &(\phi_{,r}v_{r,r} + \tfrac{\phi_{,\varphi}}{r^2}(v_{r,\varphi} - v_\varphi) + \phi_{,z}v_{r,z})\mathbf{e}_r + \\ &(\phi_{,r}v_{\varphi,r} + \tfrac{\phi_{,\varphi}}{r^2}(v_{\varphi,\varphi} + v_r) + \phi_{,z}v_{\varphi,z})\mathbf{e}_\varphi + \\ &(\phi_{,r}v_{z,r} + \tfrac{\phi_{,\varphi}}{r}\tfrac{v_{z,\varphi}}{r} + \phi_{,z}v_{z,z})\mathbf{e}_z \end{aligned} \tag{6.43}$$

Using these definitions, and applying the assumptions of axisymmetry, Eqs. 6.31 to 6.34 are expanded into the global discretized equations and expressed in block

form with generalized mass, non-linear advection, and linear diffusion matrices and a generalized forcing vector.

$$M\dot{\boldsymbol{x}} + (A(\boldsymbol{v}) + K)\,\boldsymbol{x} + = \boldsymbol{f} \tag{6.44}$$

$$\begin{bmatrix} M^r & 0 & 0 \\ 0 & M^\varphi & 0 \\ 0 & 0 & M^z \end{bmatrix} \begin{bmatrix} \dot{\boldsymbol{v}}_{\boldsymbol{r}} \\ \dot{\boldsymbol{v}}_{\boldsymbol{\varphi}} \\ \dot{\boldsymbol{v}}_{\boldsymbol{z}} \end{bmatrix} + \begin{bmatrix} A^r & A^{r\varphi} & \\ 0 & A^\varphi & 0 \\ 0 & 0 & A^z \end{bmatrix} \begin{bmatrix} \boldsymbol{v}_{\boldsymbol{r}} \\ \boldsymbol{v}_{\boldsymbol{\varphi}} \\ \boldsymbol{v}_{\boldsymbol{z}} \end{bmatrix}$$
$$+ \begin{bmatrix} K^r + \Lambda^r & 0 & K^{rz} + \Lambda^{rz} \\ 0 & K^\varphi & 0 \\ K^{zr} + \Lambda^{zr} & 0 & K^z + \Lambda^z \end{bmatrix} \begin{bmatrix} \boldsymbol{v}_{\boldsymbol{r}} \\ \boldsymbol{v}_{\boldsymbol{\varphi}} \\ \boldsymbol{v}_{\boldsymbol{z}} \end{bmatrix} = \begin{bmatrix} \boldsymbol{f}_{\boldsymbol{p}}^{\boldsymbol{r}} \\ \boldsymbol{0} \\ \boldsymbol{f}^{\boldsymbol{z}} + \boldsymbol{f}_{\boldsymbol{p}}^{\boldsymbol{z}} \end{bmatrix} \tag{6.45}$$

$$\left[M^\phi\right]\left[\dot{\boldsymbol{\phi}}\right] = \left[\boldsymbol{f}^{\boldsymbol{\phi}}\right] \tag{6.46}$$

$$\left[M^T\right]\left[\dot{\boldsymbol{T}}\right] + \left[A^T + K^T\right]\left[\boldsymbol{T}\right] = \left[\boldsymbol{q}_{\boldsymbol{\Gamma}}\right] \tag{6.47}$$

$$\left[M^A\right]\left[\dot{\boldsymbol{X}}_{\boldsymbol{A}}\right] + \left[A^A + K^A\right]\left[\boldsymbol{X}_{\boldsymbol{A}}\right] = \left[\boldsymbol{0}\right] \tag{6.48}$$

$$\left[M^B\right]\left[\dot{\boldsymbol{X}}_{\boldsymbol{B}}\right] + \left[A^B + K^B\right]\left[\boldsymbol{X}_{\boldsymbol{B}}\right] = \left[\boldsymbol{0}\right] \tag{6.49}$$

The block matrices contain integrals of the shape functions over the entire domain. Recalling the definition of the bilinear form and using indices to refer to the numerical vertices, we can express the blocks, beginning with the capacity terms and nonlinear advection terms.

$$M_{ij}^\alpha = (N_i, N_j)_\Omega \tag{6.50}$$

$$A^\alpha(\boldsymbol{v}) = (v_r N_i, N_{j,r})_\Omega + (v_z N_i, N_{j,z})_\Omega \qquad \alpha = r, z, T, A, B \tag{6.51}$$

$$A^\varphi(\boldsymbol{v}) = (v_r N_i, N_{j,r})_\Omega + (\tfrac{1}{r} v_r N_i, N_j)_\Omega + (v_z N_i, N_{j,z})_\Omega \tag{6.52}$$

$$A^{r\varphi}(\boldsymbol{v}) = (\tfrac{1}{r} v_\varphi N_i, N_j)_\Omega \tag{6.53}$$

The diffusive blocks contain the viscous terms of the momentum equation and the diffusive terms of the energy and mass transport.

$$K^r = \nu((\tfrac{1}{r} N_i, N_j)_\Omega + (N_i, N_{j,r})_\Omega) \tag{6.54}$$

$$K^{rz} = {K^{zr}}_T = \nu(N_{i,z}, N_{j,r})_\Omega \tag{6.55}$$

$$K^\varphi = \nu((N_i, N_{j,r})_\Omega + (N_{i,r}, N_j)_\Omega) \tag{6.56}$$

$$K^z = \nu(N_{i,z}, N_{j,z})_\Omega \tag{6.57}$$

$$K_T = \alpha((N_{i,r}, N_{j,r})_\Omega + (N_{i,z}, N_{j,z})_\Omega) + \delta_{ij}\frac{h}{\rho c_p}\int\limits_{\Gamma_I \cup \Gamma_W} N_i dA \tag{6.58}$$

$$K_\gamma = D_\gamma((N_{i,r}, N_{j,r})_\Omega + (N_{i,z}, N_{j,z})_\Omega) \tag{6.59}$$

$$K_B = D_B((N_{i,r}, N_{j,r})_\Omega + (N_{i,z}, N_{j,z})_\Omega) \tag{6.60}$$

The volumetric body force is integrated as well as the source term for the level set.

$$\boldsymbol{f^z} = (N_i, \beta_T(T - T_o) + \beta_A(C_A - C_{Ao}) + \beta_B(C_B - C_{Bo})) \tag{6.61}$$

$$\boldsymbol{f^\phi} = (N_i, u_n|\operatorname{grad}\phi|)_\Omega \tag{6.62}$$

The terms from the recursive penalty method are as follows.

$$\Lambda^r = (\lambda + \nu)((N_{i,r}, N_{j,r})_\Omega + (\tfrac{1}{r}N_{i,r}, N_j)_\Omega + (\tfrac{1}{r}N_i, N_{j,r})_\Omega + (\tfrac{1}{r}N_i, \tfrac{1}{r}N_j)_\Omega) \tag{6.63}$$

$$\Lambda^{rz} = \Lambda^{zr}{}_T = (\lambda + \nu)((N_{i,r}, N_{j,z})_\Omega + (\tfrac{1}{r}N_i, N_{j,z})_\Omega) \tag{6.64}$$

$$\Lambda^z = (\lambda + \nu)(N_{i,z}, N_{j,z})_\Omega \tag{6.65}$$

$$\boldsymbol{f_p^r} = \lambda(N_{i,r} + \tfrac{1}{r}N_i, p^{n-1})_\Omega \tag{6.66}$$

$$\boldsymbol{f_p^z} = \lambda(N_{i,z}, p^{n-1})_\Omega \tag{6.67}$$

Velocity and mass flux along the domain boundaries are zero, leaving only the boundary heat flux term to be integrated over the parts of the boundary that are not insulated.

$$\boldsymbol{q_\Gamma} = \int\limits_{\Gamma_I \cup \Gamma_W} N_i \frac{hT_\infty}{\rho c_p} dA \tag{6.68}$$

Time Stepping

When the equations are solved in their transient form, they must be discretized in time as well as space. There are many time integration schemes, but the three implemented for this model were forward and backward Euler time stepping and the trapezoidal method. In all of these, the time derivative is replaced by a finite difference. The methods differ by which state $\boldsymbol{x^x}$ is used to calculate the system's kinetics.

$$\tfrac{1}{\Delta t}M(\dot{\boldsymbol{x}}^{n+1} - \dot{\boldsymbol{x}}^n) + (A(v) + K)\boldsymbol{x^x} = \boldsymbol{f} \tag{6.69}$$

Table 6.3: Update equations for three time stepping schemes.

Term	Forward Euler	Backward Euler	Trapezoid
$\boldsymbol{x^x}$	$\boldsymbol{x^n}$	$\boldsymbol{x^{n+1}}$	$\frac{1}{2}(\boldsymbol{x^{n+1}} - \boldsymbol{x^n})$
K_t	$\frac{1}{\Delta t}M$	$\frac{1}{\Delta t}M + K + A$	$\frac{1}{\Delta t}M + \frac{1}{2}K + \frac{1}{2}A$
$\boldsymbol{f_t}$	$\boldsymbol{f} + (\frac{1}{\Delta t}M - K - A)\boldsymbol{x^n}$	$\boldsymbol{f} - \frac{1}{\Delta t}M\boldsymbol{x^n}$	$\boldsymbol{f} + (\frac{1}{\Delta t}M - \frac{1}{2}K - \frac{1}{2}A)\boldsymbol{x^n}$

This transient system is arranged into an update equation that can be solved at each time step. The definitions of the transient system matrix K_t and right hand side $\boldsymbol{f_t}$ vary for the three time stepping schemes, and they are summarized in Table 6.3.

$$K_t \boldsymbol{x^{n+1}} = \boldsymbol{f}_t \tag{6.70}$$

Nonlinear Advection Solution by the Secant Method

The mass transport and energy equations depend on the velocity only through the nonlinear advection matrix A. The nonlinearity will be handled by solving the velocity, temperature, and composition fields alternately. These equations are therefore linear at the time of solution.

The momentum equation is nonlinear, however, and an iterative solution procedure is required. In this model, the secant method is used. Whether the steady or the transient equation is being solved, the equation has the same form with a system matrix that depends on the state variable. Consider the momentum equation on its own, and form a residual after m iterations.

$$\boldsymbol{\mathcal{R}^m} = (K + A(v^m))\boldsymbol{v^m} - \boldsymbol{f} \tag{6.71}$$

We can then seek an update vector that drives the residual to be zero after the next iteration.

$$\boldsymbol{\mathcal{R}^{m+1}} = (K + A(v^m))(\boldsymbol{v^m} + \boldsymbol{\delta v^{m+1}}) - \boldsymbol{f} = \boldsymbol{0} \tag{6.72}$$

This gives a linear system that can be solved for the update vector.

$$(K + A(v^m))\boldsymbol{\delta v^{m+1}} = \boldsymbol{f} - (K + A(v^m))\boldsymbol{v^m} \tag{6.73}$$

This system is constructed and solved repeatedly until the norm of the residual func-

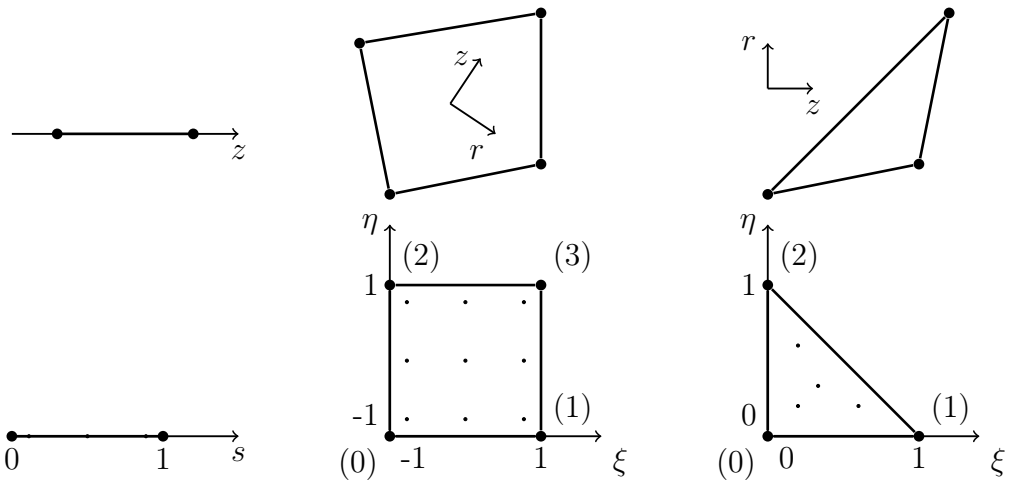

Figure 6.5: Normalized linear, quadrilateral and triangular elements with their canonical vertex numbering and typical quadrature points

tion falls below the desired threshold.

Isoparametric Formulation, Quadrature, and DEAL.II

In contrast to the FVM or the finite difference method, the Galerkin FEM relies on the explicit integration of the global equations. Whereas finite volumes or finite differences are assembled together from templates, and the finite elements of much engineering software are pre-integrated, the quadrature of each equation over the volume of each element is a characteristic of the Galerkin approach that makes it very flexible and very powerful.

This simulation was implemented using the deal.II C++ library. This library implements most of the methods described in this section. The software itself will be described later, but the fundamentals of isoparametric finite elements are presented briefly here for completeness.

In isoparametric formulations the spatial coordinates r,z are represented by the same shape functions as the global approximation functions, and all of these are parameterized within each element by natural coordinates. For the mixed elements of the interface regions, both quadrilateral and triangular elements will be required, and the parameterized forms of these elements are shown in Figure 6.5.

Each basis function in the global model spans several elements. The global integration of the governing equations is carried out element-by-element, and the contribution of each element is assembled into the global system of discretized equations.

At the most fundamental level, each element is mapped to a normalized canonical square or triangle and the quadrature is carried out making use of the Jacobian of the mapping.

$$(A,B)_{\Omega} = \sum_{e=1}^{N^e} (A,B)_{\Omega_e} \tag{6.74}$$

$$(A,B)_{\Omega_e} = \iint\limits_{\Omega_e} A(\zeta,\eta)B(\zeta,\eta)r(\zeta,\eta)\left|\frac{\partial(r,z)}{\partial(\zeta,\eta)}\right| \mathrm{d}\zeta\,\mathrm{d}\eta \tag{6.75}$$

Gaussian quadrature transforms the continuous integral into a weighted algebraic sum over the N^q quadrature points. The terms in this model are quadratic polynomials, and so three-point quadrature (in each direction) is exact.

$$(A,B)_{\Omega_e} = \sum_{q=1}^{N^q} W_q A(r_q,z_q)B(r_q,z_q)r_q \left|\frac{\partial(r,z)}{\partial(\zeta,\eta)}\right|_q \tag{6.76}$$

The boundary integrals are carried out the same way with quadrature points located along boundary segments.

$$\iint\limits_{\Gamma_I} N_i q_j n_j dA = \sum_{e=1}^{N^e}\sum_{q=1}^{N^q} W_q r_q N_i q_j n_j \,\mathrm{d}s \tag{6.77}$$

In the deal.II C++ library, the mapping Jacobian and weight functions are calculated together along with shape function values and gradients at the quadrature points. A typical quadrature loop therefore looks as follows in the simulation code:

```
for(int i=0 ; i<data.vertices_per_cell ; ++i)
for(int j=0 ; j<data.vertices_per_cell ; ++j)
for(int q=0 ; q<data.n_q_points ; ++q )
  local.M(i,j) += fe_values.value(i,q)
                * fe_values.value(j,q)
                * fe_values.JxW(q)
                * fe_values.quadrature_point(q)[1]);
```

The local vectors and matrices M^e, K^e, A^e, $\boldsymbol{f^e}$ are integrated this way, and then combined into the global matrices during the assembly process. The matrices do not represent balance laws over each element, as they would in the FVM. Rather, they

represent the element's contribution to the global balance laws.

Incompressible Flow Model and LBB Stability

The solution of advective incompressible flows using finite elements is well established and understood, including the penalty method used here to enforce the incompressibility condition. Nonetheless, the associated numerical challenges need to be addressed and handled correctly in order to simulate incompressible flows.

The FEM incompressible flow model used here is discussed in many articles and textbooks, and thorough discussion of the topic can be found in the work of Hughes, Brooks, Reddy, Sani and many others [42, 43, 44, 45]. Fundamentally, the penalty parameter λ is a Lagrange multiplier for the continuity constraint, and the advantage of the penalty method is to allow the velocity field to be obtained without calculating the associated pressure field. The use of the penalty method does not, however, entirely evade the stability challenges associated with mixed formulations.

In this work, some numerical challenges were unavoidable. In particular, the magnitude of the velocity solution depended on the choice of λ. Several approaches were investigated to resolve the problem including reduced-order quadrature, element-scale averaging, and streamline upwind Petrov-Galerkin methods. None of these resolved the problem entirely, but they are described here briefly.

In mixed formulations, which solve the momentum equation and continuity condition together in terms of $\boldsymbol{v}$ and p, the finite element method is only known to be stable if the well-known Ladyzhenskaya-Babu$\boldsymbol{s}$ka-Brezzi (LBB) condition is satisfied. In short, this condition requires that a lower order of interpolation be used for the pressure field than for the velocity field. For example, when linear basis functions are used to approximate the velocity field then the pressure approximation should be piecewise-constant. This is inconvenient, often requiring a second computational mesh, and several approaches have been developed in an effort to circumvent this requirement such as Petrov-Galerkin methods [46].

The penalty method appears to evade the inconvenience of a separate pressure mesh by avoiding having to store or calculate the pressure field at all. But in practise, penalty formulations suffer from their own stability problems that are closely related to the equivalent mixed formulations. Most importantly, it is widely accepted that the penalty terms must be integrated using a lower order of Gaussian quadrature than the other terms in the global stiffness matrix so that the penalty matrix is singular

and does not force $\boldsymbol{v} \to \mathbf{0}$ as $\lambda \to \infty$ [42]. Heinrich and Marshall, for example discuss a penalty method solution using bilinear elements with 2×2 Gaussian quadrature for viscous terms and 1×1 for the penalty terms [44].

In this work, the velocity field was found to depend on the choice of λ regardless of the order of integration that was used. In most standard solutions presented in the literature the velocity solution approaches the exact solution monatonically is λ increases, but this is not universal. Reddy, Reddy and Akay for example present a solution for incompressible pipe flow in which the axial velocity profile approaches the exact solution as λ approaches 10^4, but then changes form dramatically as λ increases to 10^6 [45]. The difference may arise from the additional complexity of the terms required by axisymmetric flow problems.

Oscillation in the velocity and concentration results also lead to investigation of streamwise-upwind Petrov-Galerkin such as those described by Brooks and Hughes [43]. These introduce artificial diffusivity in the the upstream direction to smooth oscillations that appeared upstream of boundaries. In the end, this turned out to be helpful only in simulations that were far from equilibrium such as the rapid initial dissolution of CdTe into pure tellurium. The diffusive terms were turned off for THM simulations.

6.2.4 Enrichment by Virtual Interface Elimination

The temperature, flow and composition models apply differently in the solid and liquid regions, and several methods exist for distinguishing the subdomains and assembling their equations either together or separately. A new method has been developed for this solubility system that incorporates all of the solid and liquid equations into a single system. The method is based on mixed-phase boundary elements that are enriched to capture the behaviour of the interface. We refer to the process as enrichment by virtual interface elimination (EVIE). In brief, each element that spans the interface is subdivided into single-phase subelements, and the element-level integration is carried out using the same assembly process otherwise used for the global system. The interface terms are then eliminated algebraically from the augmented element matrices prior to assembly into the global system. As an example, a simple domain containing two phases is shown in Figure 6.6.

A very similar approach based on the LSM is presented by Skrzypczak and Węgrzyn-Skrzypzak for the solidification of pure metals [47]. This model varies from

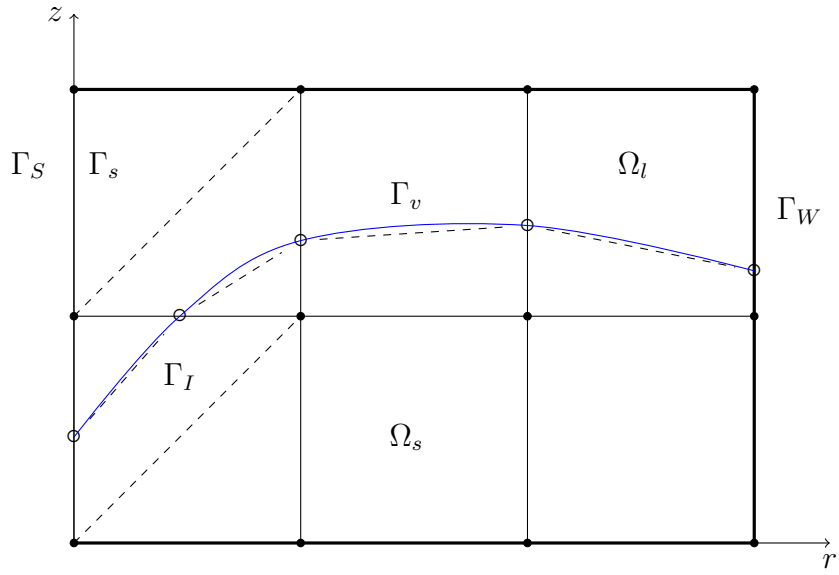

Figure 6.6: A six-patch of elements divided into liquid and solid subdomains Ω_l and Ω_s. Mixed-phase elements are subdivided into patches of single-phase elements.

theirs in several ways, however. First, it includes convection and mass transport, while their model includes only temperature and the level set. Second, this model is based on quadrilateral elements rather than triangles, which allows it to be used with common finite element formulations but which leads to some challenges with element topology. Third, the motion of the interface in this model arises from mass transport rather than energy flux. This leads to a slightly different solution procedure although the level set and energy equations are substantially the same.

The EVIE process is readily applicable to 1D and 2D simulations. Both have been carried out, and they are described together below.

As in all finite element simulations, the solution process takes place in four basic stages. In preprocessing the problem geometry and initial condition are represented by a computational mesh and associated data structures. Then, during assembly the system matrices are compiled by processing each element in turn. In the solution phase the assembled equations are solved numerically either by direct Gaussian elimination or by an iterative solution process. Finally, during postprocessing the results are saved and analyzed. In this model assembly, solution, and postprocessing are repeated at least in part for every time step.

The EVIE approach to interface-handling is carried out during the assembly phase of the finite element process. As in all finite element models, assembly proceeds

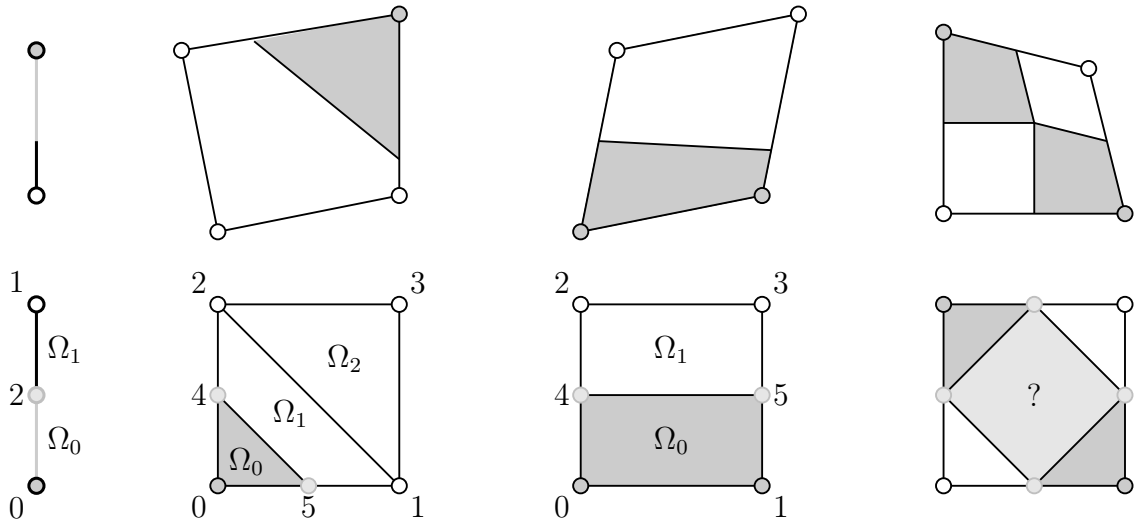

Figure 6.7: Canonical vertex numbering for 1D and axisymmetric mixed phase elements. With quadrilateral elements, two topologies are permitted. Diagonal elements, shown at right, are ambiguous and not allowed.

element-by-element. In this case, when each element is processed, the phase of each vertex is determined from the value of the level set, and the element's topology is identified. A vertex is liquid if its current level set value is positive and solid otherwise. The level set is prevented during the solution phase from being exacly zero at a vertex.

An element that is entirely solid or entirely liquid is processed normally, with the governing equations integrated by Gaussian quadrature. If the element contains both liquid and solid vertices, it must be enriched by adding vertices that lie on the interface itself. The state of the interface is determined based on the state of the overall element, and then the element is subdivided into two or three subelements as shown in Figure 6.7. The matrices for each subelement are determined using the same method as other single-phase elements, and these are combined using an assembly process very similar to the global assembly method.

Modelling the Interface

The key to the EVIE approach to enrichment is to capture the interface behaviour within mixed cells during the FEM assembly process, and then eliminate its terms from the global algebraic equations. To this end, the state of the interface within a mixed cell is determined in three steps. The process is the same for 1D simulations

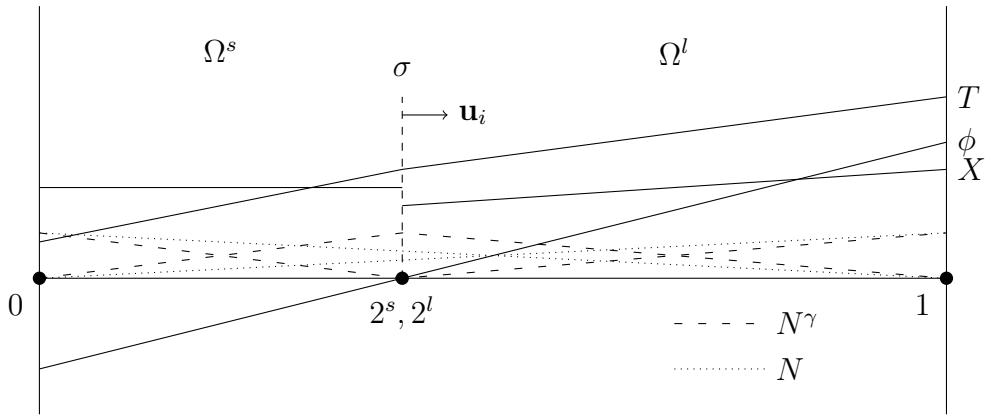

Figure 6.8: Subdivision of a mixed element into regions with positive and negative level set values. The process is identical for a 1D element or along the edge of a 2D element.

or for each mixed edge of a 2D element, so both cases are illustrated together in Figure 6.8.

Consider two vertices labelled 0 and 1 with different phases. Their level set values ϕ_0 and ϕ_1 represent the signed normal distance of each vertex from the interface. The location of a third vertex on the interface between these two is obtained by interpolation.

$$\boldsymbol{x}_2 = \boldsymbol{x}_0 + \frac{\phi_0}{\phi_0 - \phi_1}(\boldsymbol{x}_1 - \boldsymbol{x}_0) \tag{6.78}$$

Once the interface position is determined, its temperature is estimated. We can then assume that near the interface the normal fluid velocity is small, and therefore the energy equation at the interface is simply a balance of normal heat fluxes. Eq. 6.18 then reduces to a finite difference relation for the temperatures, which are used to express the temperature at the interface as a linear combination of the temperatures at vertices 0 and 1.

$$T_2 = b_{20}T_0 + b_{21}T_1 - b_{22}u_n \tag{6.79}$$

$$\dot{T}_2 = b_0\dot{T}_0 - b_1\dot{T}_1 \tag{6.80}$$

Here u_n is the rate of dissolution expressed as the normal velocity of the interface, and b_n are coefficients that depend on the thermal conductivities of the solid and liquid volumes as well as the latent heat absorbed by dissolution. These coefficients and the

interface velocity are assumed to be constant over the duration of a time step.

$$b_{20} = \frac{k_1\phi_1}{k_1\phi_1 - k_0\phi_0} \qquad b_{21} = \frac{-k_0\phi_0}{k_1\phi_1 - k_0\phi_0} \qquad b_{22} = \frac{h_L\phi_0\phi_1}{k_1\phi_1 - k_0\phi_0} \tag{6.81}$$

Finally, the interface composition and motion must be determined. The composition of the interfacial liquid depends on temperature through the phase diagram, so the interface temperature must be estimated by neglecting the effect of latent heat and determining T_2 from Eq. 6.79. The composition of the liquid at the interface is then calculated from the phase diagram. A new correlation was developed for this purpose, which was plotted in Figure 6.2. Finally the Stefan condition, Eq. 6.23, is used to calculate u_n. If necessary, the interface temperature can be recalculated with latent heat accounted for, but the slow motion of THM interfaces generally makes this unnecessary. At the end of these steps the position, velocity, temperature and composition of the interface are known, and they are ready to be assembled into the original element system.

Element Assembly and Elimination of Interface Terms

The assembly and elimination process for 2D mixed elements is somewhat involved, but we describe it here for the most complicated case. Consider therefore a mixed element with a single solid vertex, which is numbered 0, and three liquid vertices labelled 1, 2 and 3. Such an element is shown on the left in Figure 6.7. We enrich the element by adding vertex 4 between 0 and 2, and vertex 5 between 0 and 1. We then divide the element into two triangular and one quadrilateral subelement. The subelement matrices are generated by exactly the same means that handle single phase elements in the global system, and the subelements are assembled into an enriched system of element matrices, which we further augment by writing the temperature interpolation Eqs. 6.79 and 6.80 in matrix form.

$$\begin{bmatrix} M^0_{00} & 0 & 0 & 0 & M^0_{04} & M^0_{05} \\ 0 & M^1_{11}+M^2_{11} & M^1_{12}+M^2_{12} & M^2_{13} & M^1_{14} & M^1_{15} \\ 0 & M^1_{21}+M^2_{21} & M^1_{22}+M^2_{22} & M^2_{23} & M^1_{24} & M^1_{25} \\ 0 & M^2_{31} & M^2_{32} & M^2_{33} & 0 & 0 \\ M^0_{40} & M^1_{41} & M^1_{42} & 0 & M^0_{44}+M^1_{44} & M^0_{45}+M^0_{45} \\ M^0_{50} & M^1_{51} & M^1_{52} & 0 & M^0_{54}+M^1_{54} & M^0_{55}+M^0_{55} \end{bmatrix} \begin{bmatrix} \dot{T}_0 \\ \dot{T}_1 \\ \dot{T}_2 \\ \dot{T}_3 \\ \dot{T}_4 \\ \dot{T}_5 \end{bmatrix} \tag{6.82}$$

$$+\begin{bmatrix} K_{00}^0 & 0 & 0 & 0 & K_{04}^0 & K_{05}^0 \\ 0 & K_{11}^1+K_{11}^2 & K_{12}^1+K_{12}^2 & K_{13}^2 & K_{14}^1 & K_{15}^1 \\ 0 & K_{21}^1+K_{21}^2 & K_{22}^1+K_{22}^2 & K_{23}^2 & K_{24}^1 & K_{25}^1 \\ 0 & K_{31}^2 & K_{32}^2 & K_{33}^2 & 0 & 0 \\ K_{40}^0 & K_{41}^1 & K_{42}^1 & 0 & K_{44}^0+K_{44}^1 & K_{45}^0+K_{45}^0 \\ K_{50}^0 & K_{51}^1 & K_{52}^1 & 0 & K_{54}^0+K_{54}^1 & K_{55}^0+K_{55}^0 \end{bmatrix} \begin{bmatrix} T_0 \\ T_1 \\ T_2 \\ T_3 \\ T_4 \\ T_5 \end{bmatrix} = \begin{bmatrix} f_0^0 \\ f_1^1+f_1^2 \\ f_2^1+f_2^2 \\ f_3^2 \\ f_4^0+f_4^1 \\ f_5^0+f_5^1 \end{bmatrix}$$

$$\begin{bmatrix} b_{40} & 0 & b_{42} & 0 & -1 & 0 \\ 0 & 0 & 0 & 0 & 0 & 0 \\ b_{50} & b_{51} & 0 & 0 & 0 & -1 \\ 0 & 0 & 0 & 0 & 0 & 0 \end{bmatrix} \begin{bmatrix} \dot{T}_0 \\ \dot{T}_1 \\ \dot{T}_2 \\ \dot{T}_3 \\ \dot{T}_4 \\ \dot{T}_5 \end{bmatrix} + \begin{bmatrix} 0 & 0 & 0 & 0 & 0 & 0 \\ b_{40} & 0 & b_{42} & 0 & -1 & 0 \\ 0 & 0 & 0 & 0 & 0 & 0 \\ b_{50} & b_{51} & 0 & 0 & 0 & -1 \end{bmatrix} \begin{bmatrix} T_0 \\ T_1 \\ T_2 \\ T_3 \\ T_4 \\ T_5 \end{bmatrix} = \begin{bmatrix} 0 \\ b_{44}u_n \\ 0 \\ b_{55}u_n \end{bmatrix}$$

Using row elimination, the following assembled element matrices are obtained.

$$M_T^e = \begin{bmatrix} M_{00}^0+b_{40}M_{04}^0+b_{50}M_{05}^0 & b_{51}M_{05}^0 & b_{42}M_{04}^0 & 0 \\ b_{40}M_{14}^1+b_{50}M_{15}^1 & M_{11}^1+M_{11}^2+b_{51}M_{51}^1 & M_{12}^1+M_{12}^2+b_{42}M_{14}^1 & M_{13}^2 \\ b_{40}M_{24}^1+b_{50}M_{25}^1 & M_{21}^1+M_{21}^2+b_{51}M_{25}^1 & M_{22}^1+M_{22}^2+b_{41}M_{24}^1 & M_{23}^2 \\ 0 & M_{31}^2 & M_{32}^2 & M_{33}^2 \end{bmatrix}$$

$$K_T^e = \begin{bmatrix} K_{00}^0+b_{40}K_{04}^0+b_{50}K_{05}^0 & b_{51}K_{05}^0 & b_{42}K_{04}^0 & 0 \\ b_{40}K_{14}^1+b_{50}K_{15}^1 & K_{11}^1+K_{11}^2+b_{51}K_{51}^1 & K_{12}^1+K_{12}^2+b_{42}K_{14}^1 & K_{13}^2 \\ b_{40}K_{24}^1+b_{50}K_{25}^1 & K_{21}^1+K_{21}^2+b_{51}K_{25}^1 & K_{22}^1+K_{22}^2+b_{41}K_{24}^1 & K_{23}^2 \\ 0 & K_{31}^2 & K_{32}^2 & K_{33}^2 \end{bmatrix}$$

$$\boldsymbol{F_T^e} = \begin{bmatrix} f_0^0+(b_{44}K_{04}^1+b_{55}K_{05}^2)u_n \\ f_1^1+f_1^2+(b_{44}K_{14}^1+b_{55}K_{15}^1)u_n \\ f_2^1+f_2^2+(b_{55}K_{24}^1+b_{55}K_{25}^1)u_n \\ f_3^2 \end{bmatrix} \tag{6.83}$$

The interfacial mole fractions are eliminated from the mass transport equations in a similar way. The liquid mole fraction at the interface has been calculated already, and we assume that the interface remains in equilibrium throughout the time step. This constant mole fraction is therefore carried to the right hand side as a fixed flux

into the liquid vertices.

$$
\begin{aligned}
M^e_{X_\gamma} &= \begin{bmatrix} M^0_{00} & 0 & 0 & 0 \\ 0 & M^1_{11}+M^2_{11} & M^1_{12}+M^2_{12} & M^2_{13} \\ 0 & M^1_{21}+M^2_{21} & M^1_{22}+M^2_{22} & M^2_{23} \\ 0 & M^2_{31} & M^2_{32} & M^2_{33} \end{bmatrix} \\
K^e_{X_\gamma} &= \begin{bmatrix} K^0_{00} & 0 & 0 & 0 \\ 0 & K^1_{11}+K^2_{11} & K^1_{12}+K^2_{12} & K^2_{13} \\ 0 & K^1_{21}+K^2_{21} & K^1_{22}+K^2_{22} & K^2_{23} \\ 0 & K^2_{31} & K^2_{32} & K^2_{33} \end{bmatrix} \\
\boldsymbol{F^e_{x_\gamma}} &= \begin{bmatrix} f^0_0 - K^0_{04}X_{\gamma 4} - K^1_{05}X_{\gamma 5} \\ f^1_1 + f^2_1 - K^1_{14}X_{\gamma 4} - K^1_{15}X_{\gamma 5} \\ f^1_2 + f^2_2 - K^1_{14}X_{\gamma 4} - K^1_{15}X_{\gamma 5} \\ f^2_3 \end{bmatrix}
\end{aligned}
\tag{6.84}
$$

The momentum equation for the liquid portion of the mixed cell is similarly expressed in terms of the boundary vertices. Because of the no slip condition, eliminating the velocities at the interface vertices is trivial.

These matrices are assembled from each subelement using the following pseudocode.

```
for(int vi=0 ; vi<subEl.dofs_per_cell ; vi+=dofs_per_vert)
for(int vj=0 ; vj<subEl.dofs_per_cell ; vj+=dofs_per_vert){
  if( vertex(vi).not_on_interface() ){
  if( vertex(vj).not_on_interface() ){
    // Assemble the matrix entries for all variables
    for(int di=0; di<dofs_per_vertex; ++di)
    for(int dj=0; dj<dofs_per_vertex; ++dj){

      El.M( El_index(vi+di), El_index(vj+dj) )
        += subEl.M(vi+di, vj+dj);
      El.N( El_index(vi+di), El_index(vj+dj) )
        += subEl.M(vi+di, vj+dj);
      El.K( El_index(vi+di), El_index(vj+dj) )
        += subEl.M(vi+di, vj+dj);
    }
```

```
  }else{ // j is on interface, carry interfacial X to rhs
    for( int d=XA; d <= XB; ++d ){
      El.f( El_index(vi+d) )
        -= subEl.K(vi + d, vj+d, ) * subEl.solution( vj+d);
  } }
  }else{ // i is on interface, distribute interfacial T terms
    for(int vk=0; vk<subEl.dofs_per_cell; vk+=dofs_per_vert){
      if( vertex(vj).not_on_interfac() ){
        El.M( El_index(vi+T), El_index(vk+T) )
          += subEl.M(vj+T, vi+T) * b[vi][vk];
        El.K( El_index(vi+T), El_index(vk+T) )
          += subEl.K(vj+T, vi+T) * b[vi][vk];
    } }
    El.F(El_index(vj+T))
      -= subEl.K( vj+T, vi+T) * b[vj][vj];
} }
```

Alternative Fixed-Grid Discretizations

The original intent of the transport model was to incorporate it into a global thermal model of a THM furnace. The goal would then be to observe the effect of furnace design on the transport conditions in the liquid zone throughout the growth process. Because of the changing geometry of the liquid zone in tapered THM growth, a model was desired that could track the growth process in the long term through significant motion of the growth interface. THM simulations traditionally use three different computational domains for the seed, solution and source zones. This is a natural approach, but it requires that the mesh be moved during growth. If the simulated growth process is long, then new vertices and computational elements or cells must be added to avoid significant distortions of the mesh. Fixed-grid algorithms overcome this challenge by using the same elements to model multiple domains in a simulation. The result is a single mesh that remains static while the domain boundaries evolve. In the context of crystal growth, fixed grid algorithms can be useful if they allow a single mesh to represent the solid and liquid phases in a growth process. With these simulations the goal was to produce a single finite element that could be used to represent the entire growth region inside a THM experiment of arbitrary shape

without needing to explicitly define the solid and liquid domains.

The LSM is one of several algorithms that can be used to track moving domains using a fixed grid. It is widely used to track free-surfaces and fluid-fluid interfaces in multiphase flows as well as any application that involves tracking a sharp continuous interface. It is less widely used in crystal growth however than phase-field or volume of fluid methods such as the enthalpy-porosity method. These methods are considerably easier to implement, especially in 3D, but it is argued here that the LSM has distinct advantages for simulating THM.

In enthalpy-porosity and similar methods, the same elements are used to simulate solid, liquid or mixed computational cells. The phase of each element is represented by a field, generally described as porosity or volume of fluid which scales the momentum equation to eliminate the velocity in the solid. In the most common formulation, the momentum equation is written as follows [48].

$$\frac{D\boldsymbol{v}}{Dt} = \operatorname{div}(\nu \operatorname{grad} \boldsymbol{v}) - \frac{1}{\rho} \operatorname{grad} p + a\boldsymbol{v} \tag{6.85}$$

Where the parameter a is chosen to mimic the equations for flow in a porous medium. The key difference between these methods and the LSM is that the level set tracks the explicit interface location while phase fields merely indicate the average state of the elements. Phase field methods therefore result in a numerical mushy zone, composed of elements in a transitional state, whose thickness depends, for example, on the temperature range over which solidification is assume to take place. In solidification processes involving alloys or molten solutions, this numerical mushy zone can be thought of as analogous to an actual physical mushy zone caused by microsegregation. In the planar solidification of pure metals, however, it represents a numerical blurring of the solidification front. In THM, where both energy and mass must be absorbed at a sharp, planar interface it is preferable to track the interface exactly using a level set.

The particular LSM used in this work is superficially very similar to the extended finite element method (XFEM) developed by Belytschko and applied to Stefan-type problems by Chessa in order to address the shortcomings of both moving-grid models and enthalpy methods for problems with isothermal interfaces [49, 50]. In XFEM, finite elements containing discontinuities are enriched through additional terms in their shape and test functions which become piecewise-differentiable and which vanish on the discontinuous interface. Under this scheme, the temperature approximation

function can be written, for example as

$$T(\boldsymbol{x},t) = \sum_{l=1}^{n} N_l(\boldsymbol{x})T_l(t) + \sum_{J=1}^{n} N_J(\boldsymbol{x})(|\phi(\boldsymbol{x},t)| - |\phi_J(t)|)a_J(t), \tag{6.86}$$

where N_I and N_J are the standard and enrichment shape functions, a_J are the enrichment degrees of freedom and ϕ_J are the nodal values of the level set. For single-phase elements, the enrichment shape functions have no contribution, but in mixed elements they allow the interface conditions to be written in terms of the enriched discontinuous shape functions. This approach elegantly allows the discontinuous equations of the solid-liquid system to be written as a single system of approximation functions on a single fixed numerical grid. Unfortunately, the need for new, discontinuous shape functions requires particular care during their numerical integration. Quadrature over the mixed elements must be carried out piecewise. This complicates the implementation of XFEM within the framework of existing software for which quadrature and assembly are already automated. The LSM approach put forward for solidification by Skrzypczak and Węgrzyn-Skrzypczak and extended here for solution crystal growth replaces discontinuous enriched shape functions with a sub-assembly of conventional shape functions that are integrated using existing routines for Gaussian quadrature [47]. This approach was adopted in the current work rather than the admittedly more elegant XFEM largely to minimize the amount of existing code within the Deal.II library that would need to be re-written, and also to avoid adding additional terms to the FEM energy, momentum and mass-transport equations which are already unavoidably complicated to model axisymmetric THM growth.

Compared to enthalpy-porosity models, the solid and liquid domains within the THM growth region remain clearly differentiated by the LSM. Their interaction via energy and mass transport through the interface is explicitly modelled, and the instantaneous interface velocity is determined explicitly in each time step. Also, because the mixed elements are subdivided during assembly, larger mixed elements can be used without producing a more diffuse estimate of the interface location. Unlike the XFEM method, however, the current EVIE process confines the enrichment to the element assembly process without changing the essential finite element equations. This simplifies the implementation required to model the entire THM growth region of arbitrary geometry with a single class of finite elements.

Solution Procedure

Simulations consist of time evolution of the combined mass-transport and level-set Stefan model. At each time step, the temperature and velocity fields are updated if sufficient time has passed and then the position of the interfaces and the composition of the liquid zone is stepped. All variables, including the temperature and velocity fields are integrated using fully implicit backwards-Euler time stepping. The energy, momentum and mass transport equations are assembled as needed together in one pass over all the elements. During the secant-method solution of the momentum equation only the nonlinear advection term is recalculated.

Mesh Refinement

The EVIE algorithm is well suited for unstructured meshes, which is beneficial for modelling the changing radius of the current THM ampoules. Proper handling of hanging nodes has also been implemented, which means that adaptive meshing and local refinement is possible with the existing code. True adaptive meshing has not been used, but in some simulations the mesh has been refined close to the axis and the interfaces. This is particularly helpful in the current study because numerical artifacts such as checkerboarding are observed most often where interfaces intersect with the axis. Some sample meshes from this work are shown in Figure 6.9. None of the simulation results reported here included hanging nodes within the liquid domain, but full adaptive meshing could be attempted in future work if desired.

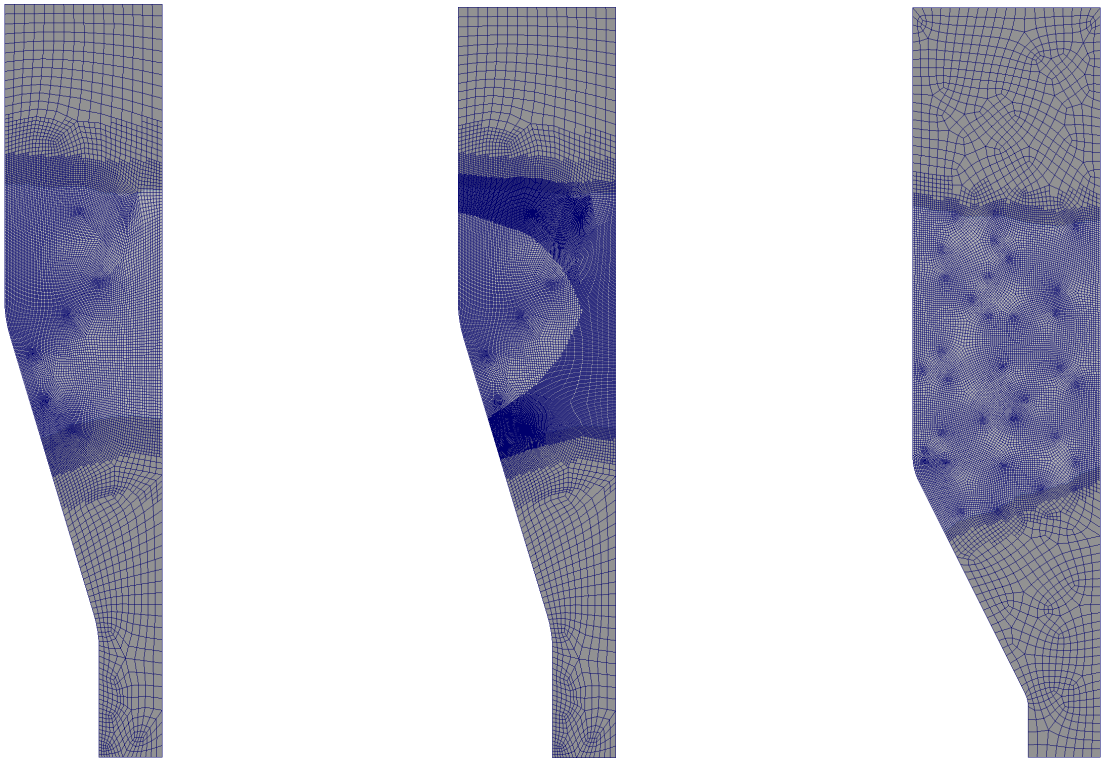

Figure 6.9: Meshes used for the 25 mm (left) and 65 mm diameter simulations. Centre: Refined mesh to resolve boundary layers near interfaces and the axis.

Table 6.4: Workflow and software for the simulations

Stage	Software	License
Mesh Generation	Gmsh [51]	GNU GPL
Preprocessing	C++ application using Deal.II [52]	GNU LGPL
Solution	Deal.ii methods, UMFPACK [53]	GNU LGPL, GPL
Visualization	Gnuplot (1D), Paraview (2D) [54]	BSD 3-Clause
Publication	pdfTeX [55] via Gnuplot PGF/TikZ	GNU GPL

6.3 Details of the Simulation Software

6.3.1 Open Source Workflow

To maximize the flexibility of the simulations, a workflow has been developed based entirely on open-source software. This has allowed all details of the simulation process to be controlled at the lowest levels, and it demonstrates what is now possible using software that is distributed free of charge. Unfortunately, the immense control comes at a cost of increased complexity. This work flow is not nearly as fluid as, say, the integrated Workbench now provided by ANSYS for its CFX and Fluent software.

Table 6.4 summarizes the workflow. Gmsh was used to generate the problem geometry from a script file. This software can be used to generate meshes from CAD files; however, the relatively simple geometry of the THM system is easily parameterized and defined explicitly. The new software developed for this project was written in C++ using the Kdevelop integrated developing environment. Standard library functions were included from the Differential Equations Analysis Library (deal.II). Deal.II provides data structures such as sparse matrices, routines for storing and retrieving data, standard classes for managing finite elements, numerical meshes, quadrature formulas, and implementations of standard numerical solvers. The library is very powerful, and full documentation is available along with many tutorial sample programs. Even with the examples, however, developing a new application required dozens of hours reviewing the documentation and searching for the best way to implement ideas.

Deal.II provides implementations of several iterative numerical solvers, and it includes a distribution of UMFPACK from SuiteSparse. UMFPACK uses LU decomposition to solve linear systems, and it is the standard direct solver used in MATLAB. In practice, this direct solver was much faster for this simulation than the iterative solvers that were tested. Deal.II includes routines for exporting data in various formats. For this work Gnuplot was used for 1D data, and Paraview was used for 2D data. The Gnuplot Lua-Tikz terminal was used to plot results directly into LaTeXcode for inclusion in PDF files. Paraview has better tools for visualizing large datasets and 2D data, and it generated jpeg images for inclusion in documentation.

A very impressive range of open-source software now exists for carrying out simulations. A workflow built around deal.II was originally chosen over commercial alternatives because of the flexibility of implementing a fixed-grid solubility model

at the most fundamental levels of the finite element analysis. Although the process of writing, debugging, testing and analysing simulations written in raw C++ turned out to be enormously time-consuming, it permitted total control over all aspects of the model and allowed insights into the causes of numerical challenges and erroneous results.

6.3.2 Structure of the Deal.II Simulation Application

The simulation software is written as a C++ application. Following the deal.II structure, the application is heavily templated, with template instantiations that allow the same code to be used for either 1D or axisymmetric analysis. Several key class templates are summarized in Table 6.5.

Parallelization

The piecewise integration required for the finite element assembly process lends itself well to parallel processing. This application uses multiple processors with shared memory to construct the global equations. Using a standard implementation from deal.II, two classes are defined. eMatrices stores the element matrices, and eScratch contains the data structures and methods required to process an element and fill its associated eMatrices object. The deal.II function Workstream::run() creates one eScratch object and a queue of N^{em} eMatrices objects for each of the N^{pr} processors.

Simultaneously, each processor uses its eScratch object to populate its queue of eMatrices. Once this is complete, it copies the element data into the global matrices. Although all of the processes can process elements simultaneously, only one at a time has access to the global equations.

In addition to the assembly, several of the numerical solvers make use of parallel processing. This is handled natively in the deal.II code, and it is not implemented explicitly in the application.

Renormalization

The level set method for tracking domain boundaries requires a renormalization procedure to ensure that the level set function, ϕ continues to represent the signed distance of each vertex from the interface. In this simulation, renormalization was carried out after every five time steps or whenever a vertex changed phase. Longer periods were

Table 6.5: Key components of the simulation application

Namespaces	
EVIE	Global project namespace for EVIE simulations
EVIE::parameters	Constants to define the application
EVIE::assembly	Methods and scratch data for assembling an element
EVIE::thm	Classes specific to THM simulations
EVIE::dissolution	Classes specific to dissolution experiments
properties	Classes defining material properties
triangles	Reimplementation of classes for triangular elements
Principle Classes	
EVIE::Simulation<D>	Overall class for the simulation with D dimensions
assembly::ElScratch<D>	Processes each element during assembly
assembly::ElMatrices<D>	Storage for element matrices
thm::boundary_values<D>	Boundary conditions for the THM simulations
thm::initial_conditions<D>	Initial conditions, when needed
EVIE::Postprocessor<D>	Processes the results
EVIE::Output<D>	Writes results in Gnuplot or Paraview formats
EVIE::Step<D>	Tracks simulation and execution times for one step
EVIE::Time<D>	Tracks overall simulation and execution times
EVIE::GlobalData<D>	Stores key results from each time step
properties::CZT<p>	Properties and phase diagram for CZT with phase p
triangles::T_Cell<V>	Defines a cell with V vertices
triangles::T_FESystem	Defines the degrees of freedom on a triangular cell
triangles::T_Quadrature	Quadrature formulas for triangular cells
triangles::T_Mapping	Normalization of triangular cells
triangles::T_FEValues	Calculates shape functions etc for triangular cells

found to distort the interface shape, while renormalization after each step could trap the interface by returning it exactly to its original state.

The renormalization process was carried out as follows. For each element which contained a portion of a solid-liquid interface, five points were constructed with equal spacing in a straight line on the enclosed interface. The distance of every vertex in the mesh was measured from each point and if a vertex was found to be closer than indicated by its currently recorded value of ϕ, the current ϕ solution was changed to the new distance, maintaining its sign. Although inefficient, this process was effective and took very little time compared to the assembly and solution processes.

Relaxation

Over-relaxation and under-relaxation are frequently used in iterative procedures to accelerate convergence. In this work under relaxation is used in the secant method solution of the non-linear momentum equation. During each iteration of the secant method, the update vector is first scaled by a global factor, $\omega = 0.8$.

$$\mathbf{v^{n+1}} = \mathbf{v^{n}} + \omega(\mathbf{v^{n+1}} - \mathbf{v^{n}}) \tag{6.87}$$

In addition to this global under-relaxation, several local relaxation schemes were implemented to improve the convergence of the non-linear velocity solution. At each vertex, the change in each velocity component was limited to a multiple of the current solution value. This multiple was further restricted if the component changed sign, to prevent oscillation of the iterative solution process. Finally, the velocity change was limited to a multiple of the maximum velocity in the solution, with allowance made for the case that the starting velocity is very small. The local relaxation schemes were motivated by very strong solutal convection in simulations of rapid dissolution. For the more moderate convection associated with THM simulations, global under-relaxation has been sufficient to obtain converged solutions to the non-linear momentum equation.

Pushing and Smoothing

The solute-transport model occasionally produces sudden changes in solution composition, especially near rapidly-moving interfaces. These sudden changes can destabilize the solution by creating, for example, negative solute mass fractions or very strong composition gradients. Such disruptions arise most often when a vertex is extremely close to the interface. When the normal distance from the interface is small, the heat and solute fluxes become very sensitive to variations in the interface condition. Minor variations lead to very large gradients and sudden changes.

These instabilities are addressed in two ways. First, after each time step the interface is pushed away from vertices to which it is too close. That is, the parameter $|\phi|_{min} = 1 \times 10^{-4}\,\mathrm{mm}$ is defined which represents the minimum absolute distance of any vertex from the solid-liquid interface. After each progression of the level set function, the function value at each vertex is checked and increased if necessary to maintain an absolute value larger than this minimum distance. This pushing

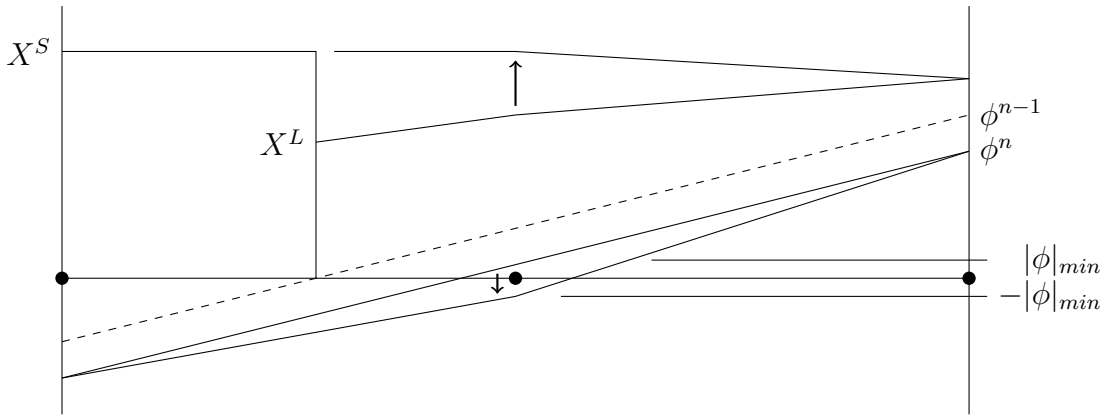

Figure 6.10: A liquid vertex solidifies when the level set, ϕ becomes smaller than $|\phi|_{min}$. The level set is pushed to $-|\phi|_{min}$ to prevent overly large gradients, and the solute fraction, X is set to the solid composition.

procedure takes into account the direction that the interface moved during the last time step so as to avoid locking the interface shape when the growth velocity is small. When $|\phi|_{min}$ is sufficiently large, sudden motions of the interface are nearly eliminated. In the first steps of a transient simulation, when quasi-equilibrium conditions have not been established, negative solute concentrations can arise even with a reasonable choice of $|\phi|_{min}$. A smoothing procedure is therefore employed which checks the composition at each liquid vertex after each time step and limits the solute mole fractions to values between 0 and 1. Vertices that are very close to the interface are also checked to ensure that their solute mole fractions will not lead to enormous interface velocities in the next time step. In practise, smoothing is never triggered after the first dozen steps of a simulation.

Phase Changes

The level set method must allow for vertices to change phase in order to simulate multiphase systems without moving the mesh. In this solute transport model, the phase change is particularly problematic because of the sharp change in composition and behaviour between the solid and liquid phases. After each time step, vertices that changed phase must be identified. Each vertex is checked to ensure that the magnitude of the level set remains larger than the interface tolerance. If not, then the vertex changed phase.

$$(\phi^{n-1} < 0)\ \&\ (\phi^n < -|\phi|_{min}) \Rightarrow \text{Solid vertex dissolved}$$

$$(\phi^{n-1} > 0)\ \&\ (\phi^{n} > \quad |\phi|_{min}) \Rightarrow \text{Liquid vertex solidified}$$

When a liquid vertex solidifies, the composition of the solid is assigned based on the relative fluxes of the solutes toward the interface, which is recorded during the assembly process. When a solid vertex dissolves, the interface condition is recalculated based on the current temperature, and the newly liquid vertex is set to the interface's equilibrium liquid composition.

More sophisticated methods were used to assign compositions to vertices after phase changes, but these ultimately failed. In particular, setting the liquid composition of newly dissolved vertices to preserve the interface velocity failed in two situations: first when renormalization caused the interface to move contrary to the direction predicted by the mass transport in the liquid, and second when sudden motion of the interface was caused by insufficient smoothing. In both cases, continuing an artificial motion of the interface lead to further instability and poorer resolution of the interface shape. Assigning newly dissolved vertices the composition of the liquid interface is an approximation that worked well, particularly when the solution zone as a whole was nearly saturated with solute.

Computing Hardware

Simulations were executed on a Dell Precision M4700 mobile workstation with 16 Gb of RAM. The Intel Core i7-3740QM cpu has four cores giving eight logical processing units.

On this hardware, simulations typically require one second of real time to simulate one second of THM growth at 25 mm diameter, but this is very sensitive to the mesh density and other parameters.

Table 6.6: Outline of the simulation software with key class methods

```
Simulation<D>::run(){
 Simulation<D>::createMesh();
 Simulation<D>::createEqns();
 do{ // Time steps
  Simulation<D>::assemble_equations<all>(){
   for(element){
    Simulation<D>::fill_eMatrices(eMatrices){
     Scratch::get_topology();
     if( element.is_single_phase )
      Scratch::calc_eMatrices(element,eMatrices);
     else
      Scratch::subDivideCell(){
       for(sub_element){
        Scratch::calc_eMatrices(sub_element,sub_eMatrices);
        Scratch::copy_to_global(sub_eMatrices, eMatrices);
   } }} // fill_eMatrices()
    Simulation<D>::copy_to_global(eMatrices);
   }} // assemble_equations();
   Simulation::apply_diriclet_boundary_conditions();
   Simulation::solve_for_velocity(){
    do{
     Simulation<D>::solve_newton_step(newton_update);
     solution += secant_update;
     Simulation<D>::assemble_equations<nonlinear_terms>();
    }while(not_converged)
   } // solve_for_velocity()
   Simulation::solve_for_temperature();
   Simulation::set_time_step();
   Simulation::update_mol_fraction();
   Simulation::update_level_set();
   Simulation::apply_relaxation();
   Simulation::renormalize_level_set();
   Simulation::push_interface_off_vertices();
   Simulation::handle_phase_changes();
   Output::current_solution<postprocessor>();
  }while(time.not_elapsed)
} // run()
```

6.4 1D Simulation of Dissolution and THM

Simulations were carried out first in 1D in order to test the ability of the level set method and the EVIE approach to correctly track interface motion. This was possible because the EVIE code and the underlying deal.II C++ library make use of class and function templates to allow much of the same code to be used for 1D and axisymmetric simulations.

The subdivision of mixed elements and determination of interface conditions was much easier to implement in 1D than for the axisymmetric case, and the absence of fluid velocity made the mass transport problem easier to solve. 1D simulations were therefore used frequently to test the software's ability to accurately model interface motions using the level set method, and models for binary and ternary THM or VGF growth were prepared first in 1D and then for the axisymmetric case.

The dissolution experiments described in Section 4.5 were used to measure the diffusivities of CdTe and ZnTe in liquid tellurium zones similar to those in THM growth experiments. In addition to providing a suitable diffusivity value for use in simulations, these experiments were important test cases for the EVIE approach to simulating the interface motion. Because of the diffusive conditions achieved during the experiments, the system was readily simulated in 1D.

In 1D simulations, the calculated displacement of the dissolution interface matches the analytical and experimental results very well for both temperatures considered in the experimental study. Averaging of the solute flux over the time step was needed to achieve this agreement.

A mesh refinement study confirms that as the grid spacing gets smaller the results approach the exact solution, but this is only true if care is taken to ensure that the limits such as the interface tolerance remain much smaller than the mesh spacing. As the grid spacing gets very small, so does the time step and the simulations become slow, but good results are achieved with a grid spacing of 0.25 mm. The converging results for dissolution in a 130 mm tall domain are shown in Figure 6.12.

Several parameters in the EVIE code are intended to ensure that the simulation remains stable in the face of sharp changes and rapid transient conditions such as initial conditions consisting of non-saturated tellurium solutions. These parameters put limits on the time step based on rapid changes in interface position or local liquid composition. The impact of these limits on the results of 1D dissolution simulations was investigated, and the results are shown in Figure 6.13 and Figure 6.14. Limiting

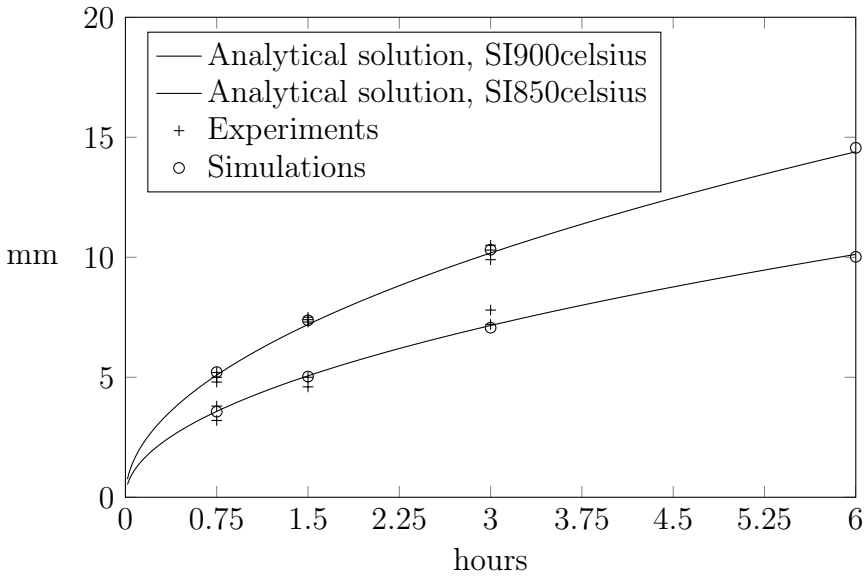

Figure 6.11: Dissolved distance under diffusive conditions as determined by the analytical solution, experiments and the EVIE simulations.

the local change in liquid composition has negligible effect on the simulation result, as this limit affects only a handful of time steps at the beginning of the simulation. Allowing the interface to travel further than half of one element length in a single step does affect the simulation results. Like the limitation on composition change, this limit is only needed at the outset of the simulation when the liquid is not nearly saturated. Allowing very rapid interface motion at this stage does however significantly poison the interface position throughout the remainder of the simulation.

During most of the simulation, the time step was limited by an arbitrary global choice of 60 s. Varying this time step between 5 and 300 s did not significantly change the simulation results.

In addition to dissolution experiments, THM experiments were simulated in 1D to verify that the dissolution and growth of ternary materials could be modelled using the EVIE approach. Figure 6.15 and Figure 6.16 show the calculated mole fractions when THM growth of $Cd_{.96}Zn_{.04}Te$ proceeds at 2 mm/d and at 10 mm/d. In each case a temperature peak corresponding to the measured wall temperature profile of 25 mm diameter THM experiments was imposed on a 1D length of CdZnTe containing a pure tellurium liquid zone 10 mm tall. As observed in experiments, the solution dissolves compound from above and below until becoming saturated with CdTe (species A) and ZnTe (species B). As the temperature profile translates, growth and dissolution

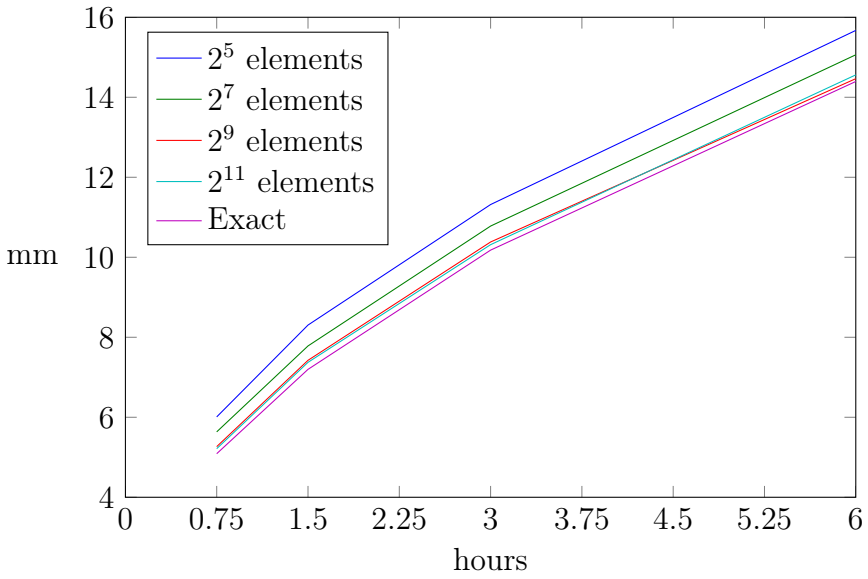

Figure 6.12: Interface displacement in 1D simulations using increasing mesh density.

proceed, and vertices dissolve and solidify as needed based on the motion of the level set.

The 1D simulations cannot account for velocity in the solution zone, so they represent a hypothetical THM process under diffusive conditions such as might be achieved under microgravity in space. The first hours of the THM simulations show the saturation of the liquid zone. The composition profiles after 45 and 90 minutes have the same form as those observed in dissolution experiments. Once the solution zone is saturated and growth proceeds, a composition gradient drives diffusion from the dissolution interface to the growth interface. As expected, the gradient is proportional to the rate of translation.

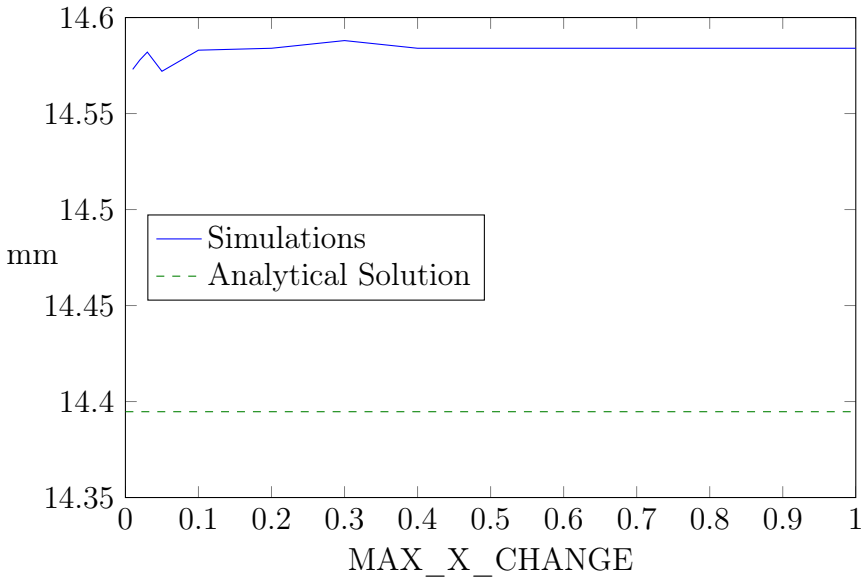

Figure 6.13: Effect of the maximum allowable change in the liquid mole fraction per time step on the calculated interface position after three hours of simulated dissolution using 2^{11} elements.

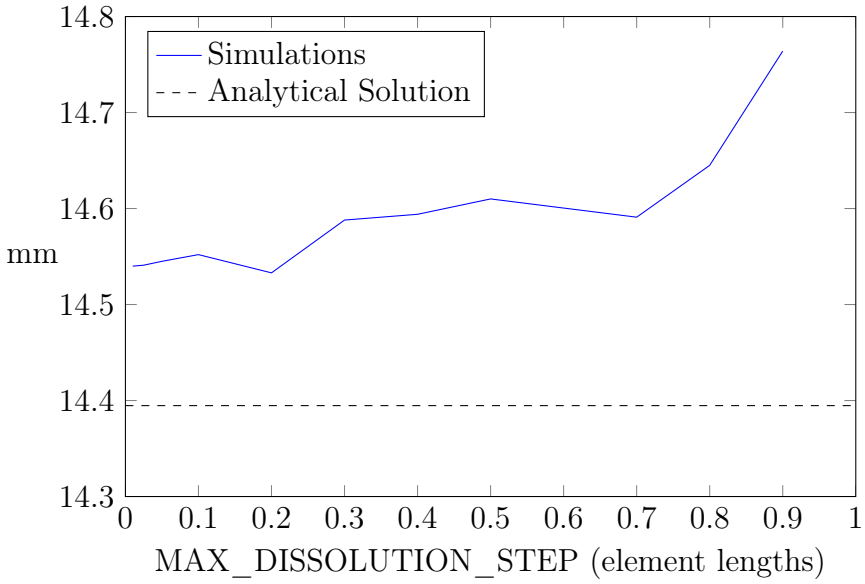

Figure 6.14: Effect of the maximum allowable interface motion per time step on the calculated interface position after three hours of simulated dissolution using 2^{11} elements.

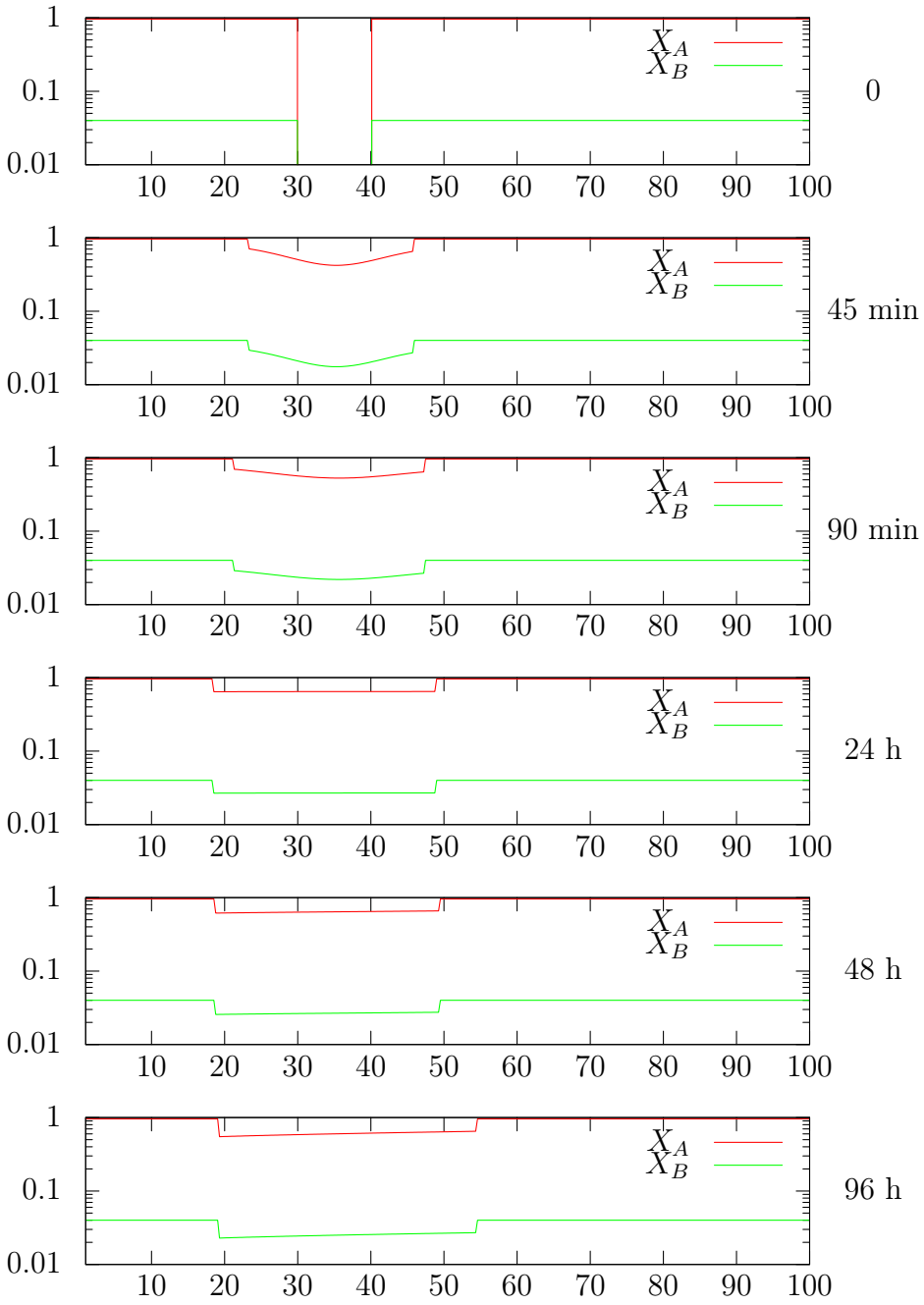

Figure 6.15: 1D simulation of ternary THM growth at 2 mm/d.

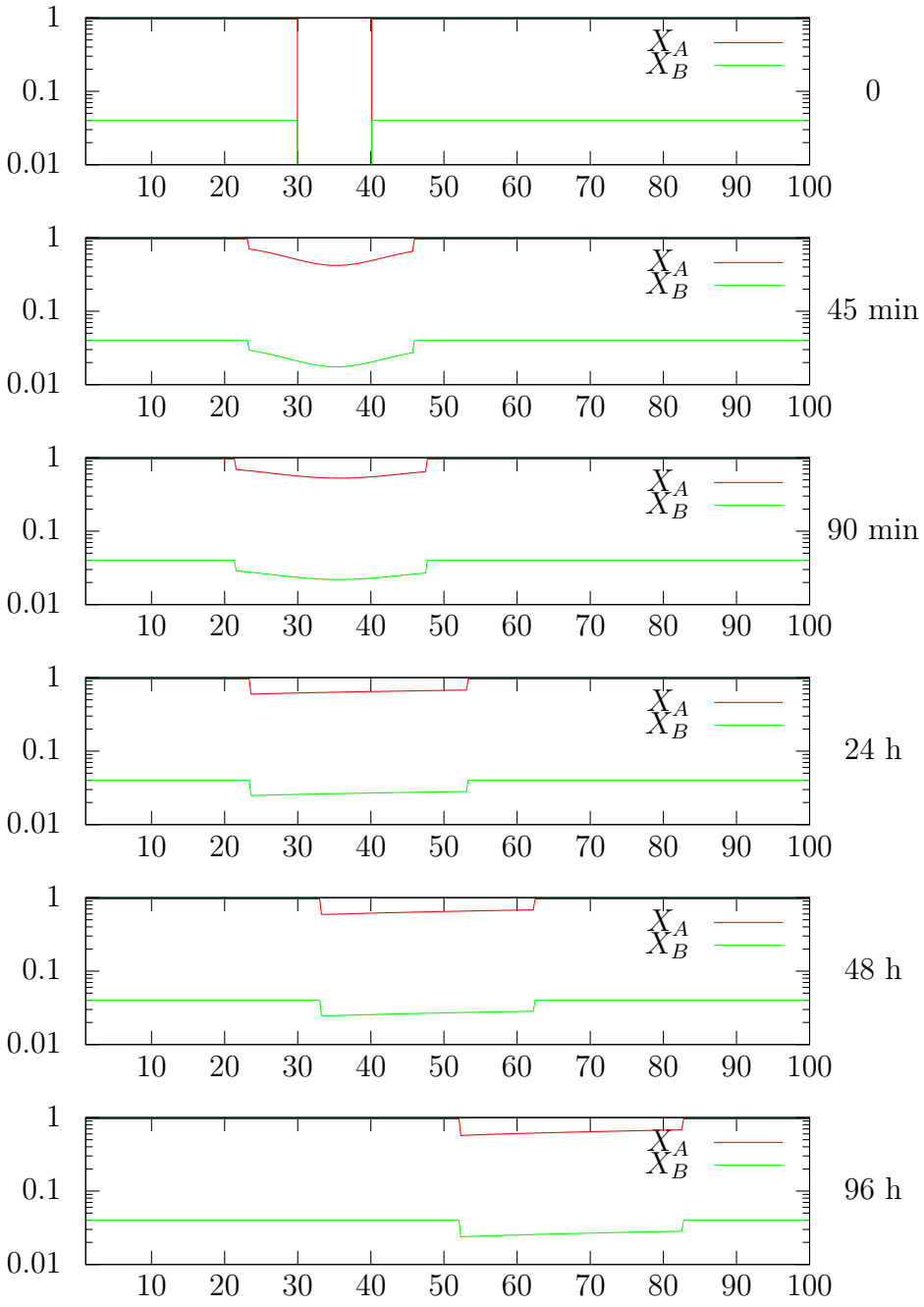

Figure 6.16: 1D simulation of ternary THM growth at 10 mm/d.

6.5 Axisymmetric Simulation of THM Growth

The purpose of THM simulations was to inform the design and operating parameters of the growth furnaces. In particular, the effect of temperature boundary conditions on the shape of the growth interface and the convection velocities was investigated.

The development of a finite element based model of the ampoule interior was originally intended to be integrated into global simulations and relate the furnace geometry to the shape of the growth interface, but this was not possible within the time of the project. Instead, simulations were restricted to the ampoule interior and related to the physical furnaces through temperature measurements taken outside and inside the ampoules in situ. Such temperature measurements are described briefly in Section 5.6.

The growth conditions within a THM ampoule are sensitive to the applied temperature profile, and the characteristics of the liquid tellurium zone require that not only the heat flux but also the convective velocity field be simulated in order to determine the shape of the growth interface. Although 1-D simulations confirmed that the EVIE software can track a moving interface in principle, the extension of the process to the axisymmetric case was a much more complex problem because of the presence of convection. Because velocity and composition cannot be observed in place during an experiment, simulation results were compared quantitatively to other published simulations under similar conditions and qualitatively to the final observed states of several experiments.

6.5.1 Velocity Field

Growth in the THM furnaces is characterized by very strong thermal and thermosolutal convection.

Prior to growth, as CdTe dissolves into pure tellurium, the concentration gradient generates extremely strong solutal convection, with Reynolds numbers briefly as high as 2500 in 25 mm diameter simulations and 50,000 at 65 mm diameter. This transient stage is characterized by multiple strong convection cells driven mainly by solutal convection. Once the solution becomes saturated and well mixed, convection is dominated by thermal effects with a weaker solutal contribution to the convective body force. The convection cells coalesce and reverse direction leaving one or two cells which generally rise at the heated wall and fall in the centre of the solution. Experiments were conducted with a growth rate of 2 mm/d. At this growth rate,

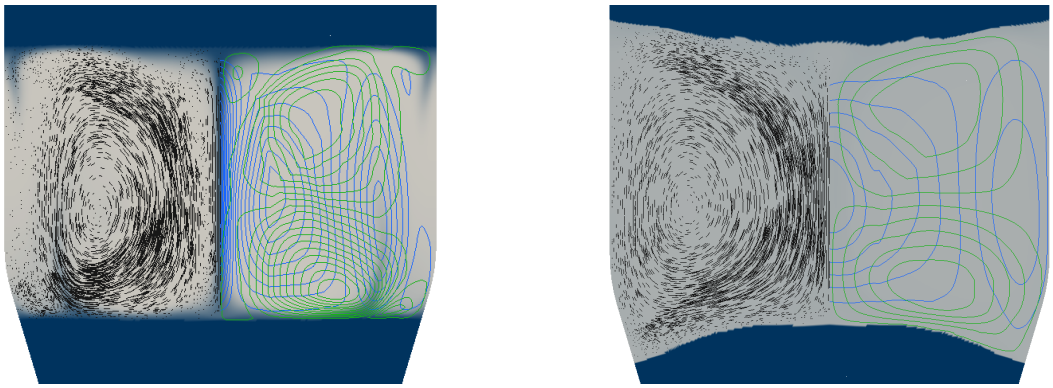

Figure 6.17: Velocity vectors and contours of v_r and v_z for a 25 mm diameter tellurium solution zone. Left: Strong initial flow with $v_{max} = 20$ mm/s as CdTe first dissolves into the solution. Right: Weaker thermal convection with $v_{max} = 5$ mm/s after the solution composition has become uniform.

convection is dominated largely by the temperature gradient with the thermal and solutal Grashof numbers calculated to be $Gr_T \approx 10^8$ and $Gr_C \approx 10^9$. The maximum velocities in the 25 mm and 65 mm systems dropped to the range of 5 mm/s and 20 mm/s respectively with Reynolds numbers between 250 and 2000 for the smaller system and between 5,000 and 10,000 for the large system depending on the thermal conditions.

This convection is very strong. Simulations by other authors have reported similarly strong convection in THM systems, albeit usually at smaller diameters. Ghaddar et al, simulating 2 cm diameter THM report Reynolds numbers as high as 300 with Grashof numbers near 10^8 [19]. Stelian reports maximum velocities of 25 mm/s to 80 mm/s in 50 mm diameter THM [56].

The penalty method is used in this work to simulate the incompressible flow field. Unfortunately, although this allows the simulation to proceed without calculating the pressure field, it relies on the penalty parameter, λ, which must be chosen carefully to avoid affecting the result. If it is too low, then a compressible flow field results which at its worst is simply a uniform velocity with no flow circulation. If λ is too large, the velocity field is artificially damped and attenuates in proportion to the penalty parameter. Figure 6.18 compares the computed velocity fields for the 65 mm diameter simulations under varying values of λ. For the conditions shown, The structure of the flow field changes from uniform flow at $\lambda = 10^3$ to a single stable convection cell at $\lambda = 5 \times 10^5$ in which the maximum velocity is between 13 and 20 mm/s. When the penalty parameter continues to increase, the flow stucture is maintained but the

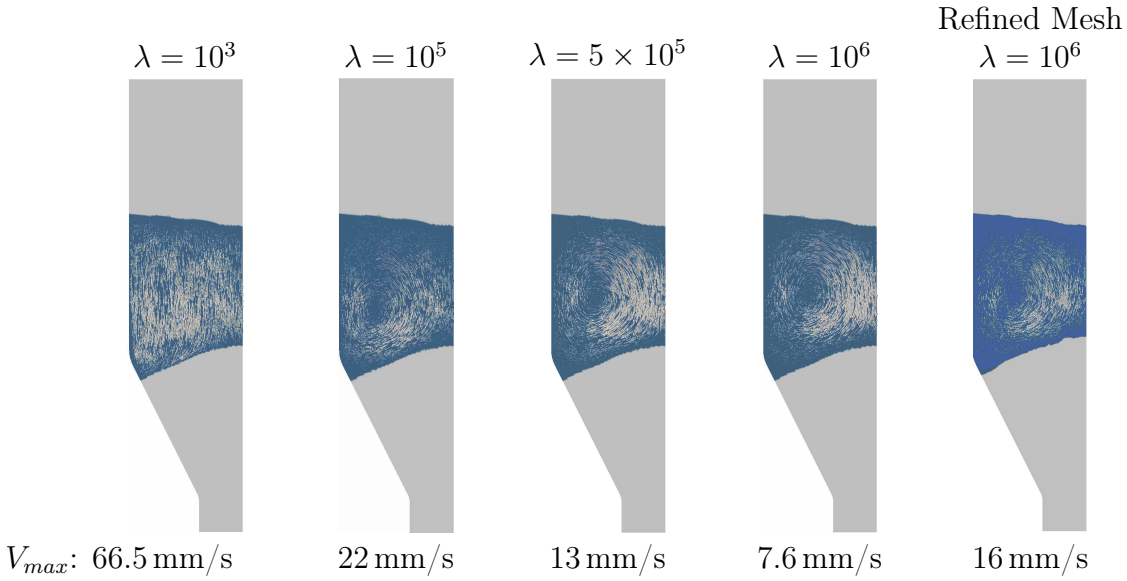

Figure 6.18: Sensitivity of the velocity field to the choice of penalty parameter, λ. At values of $\lambda > 5 \times 10^6$ the flow structure stays the same and velocity is inversely proportional to λ. When the number of liquid elements is doubled, the flow structure is consistent for $\lambda > 10^6$. Diameter is 65 mm

entire velocity field is attenuated.

The attenuation of the flow field with increasing values of the penalty parameter is an unfortunate property of these simulations, and its cause is not clearly understood. The penalty method for modelling incompressible flows has been widely used, and such artificial attenuation has been reported before occasionally. Reddy et al, discussing element-by-element finite element solvers in 1992 for example report a similar dependence on λ for the axial velocity profile for flow inside a pipe. [45].

The attenuation of velocity when λ is large may be related to the problem of LBB stability, which was discussed in Section 6.2.3, but reduced-order quadrature of the penalty terms did not resolve the problem. In general, though, the velocity field is assumed to be most accurate when λ is set to the minimum value for which the shape of the flow field no longer changes. This was tested by recreating the simulation conditions modelled by Dost and Liu, and the velocity field obtained in this model was the same [40].

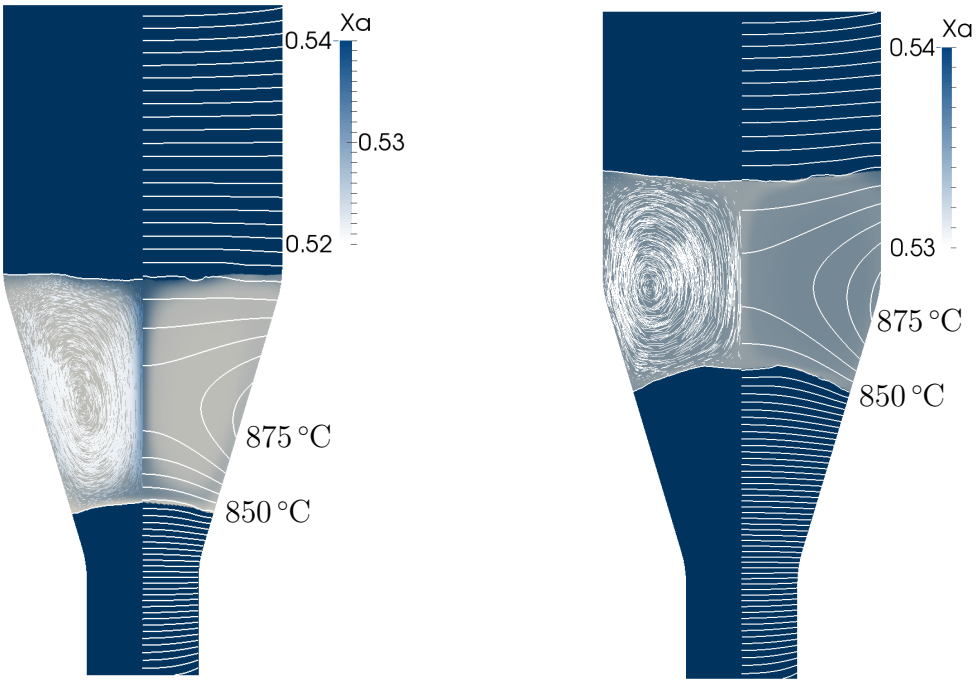

Figure 6.19: 25 mm diameter growth experiment with a 10 mm seed. $v_{max} = 5\,\mathrm{mm/s}$, $Re = 600$.

6.5.2 Convection and Interface Shape

The shape of the growth interface is found to be highly dependant not just on the temperature field imposed by the design of the THM furnace, but also on the amount of thermosolutal convection. This is because the rate of growth or dissolution of a solid-liquid interface depends both on its temperature and on the local solute concentration through the material's phase diagram. It is therefore possible to have significant variation of the interface temperature if it is accompanied by a significant variation in the liquid composition. This is in contrast to the simulation of melt growth, in which the solid-liquid interface is assumed to be isothermal.

The experimental approach in much of this study has been to pursue a convex interface shape by extracting heat through the seed crystal. Simulations, however, indicate that this may have been counter-productive. The problem arises due to the stagnation points at the centre and outside edges of the growth interface. The velocity field does not penetrate into these regions, so the transport of solute to the centre of the growth interface is dominated by diffusion no matter how strong the convection in the rest of the solution zone. In simulations with strong convection ($Re = 500$), growth is observed in a ring around the centre of the growth interface, where the

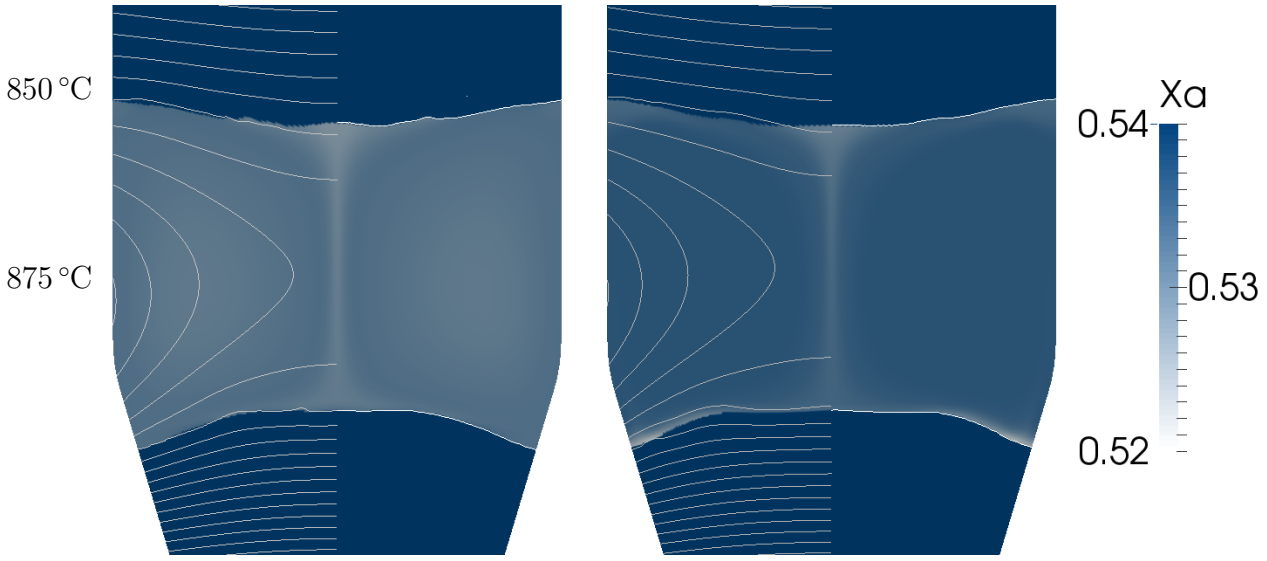

Figure 6.20: Left: Translation begins with a THM solution that is not quite at steady state. Right: After 6 h the growth interface becomes concave.

interface is awash in convected solute. The centre itself becomes depleted of solute and a concave divot forms. Importantly, this effect is not observed if the system is allowed to reach a steady state with no translation. It results from the greater diffusion boundary layer thickness and therefore the lower interface temperature needed to sustain the steady state growth rate.

Because of the advective nature of mass transport in the liquid zone, the interface shape is very sensitive to transient effects. Figure 6.20 shows a solution zone which has not been given sufficient simulation time to come to complete equilibrium. The dissolution interface is not fully isothermal and it is actually still growing in the centre. As a result, although the growth interface is favourably flat when translation begins, a plume of depleted solution prevents growth in the centre of the interface resulting in a depression after 6 h of growth. The range of solute mole fractions in the liquid zone is only 0.528 to 0.532, but this one-percent variation in composition is enough to produce concavity in the growth interface and lead to the formation of secondary grains.

This inability to achieve the desired interface shape through pure thermal design is due to the fundamental difference between THM growth and melt techniques such as VGF. In THM it is the transport of solute within the liquid zone that controls the interface shape rather than the transport of energy.

6.6 Discussion

The strength and importance of thermosolutal convection has been known and discussed for over thirty years. In 1975 Wald and Bell estimated convection rates and calculated interface shapes for THM growth of CdTe at 1 cm diameter and recommended AAR to replace already strong natural convection with stronger but controllable forced convection [15]. In 1994 Mokri, Triboulet et. al. applied AAR to 50 mm THM in order to make convection more controllable and found larger grains in the resulting ingots [16]. Since then research by several groups has focused on the impact of AAR and other techniques such as RMF on convection and on the resulting growth interface shape.

The relationship between convection and interface shape has also been observed before in simulations. Sadik Dost and YongCai Lui, reported in 2007 on simulations of CdTe THM at 25 mm diameter [40]. In fact, their numerical work was a simulation of the THM experiments conducted prior to the current study using the same 25 mm furnace, and its results were used to test the performance of the current simulation software with respect to the temperature and velocity fields. Their thermal boundary condition at the wall was also adopted in the current work. Dost and Liu reported the same dip in the centre of the growth interface under the influence of convection, and their article compared heat extraction and ampoule rotation as strategies to mitigate the problem. They reported that the interface could be made more flat by removing more heat from the bottom of the crystal very early in experiments, and that as experiments progressed the interface naturally became flatter. They do not discuss the mechanism that causes the growth interface to improve as the experiment progresses, but based on the current work, it is likely that reduced convection due to weaker temperature gradients reduced the rate of convective transport to the growth interface allowing diffusive transport to be more dominant.

A key difference between Dost and Liu's simulations and this model is the choice of boundary condition at the growth interface. In their work, the interface position was calculated from the energy equation through the latent heat and the furnace translation rate, V_g.

$$k\frac{\partial T}{\partial n}\bigg|_l - k_s\frac{\partial T}{\partial n}\bigg|_s = \rho_s h_L V_g(\boldsymbol{n}\cdot\boldsymbol{e}_z) \tag{6.88}$$

In the present model, the interface motion is calculated directly from the flow of

solute in and out of the liquid. The energy equation is used to calculate the interface temperature but not its motion. Moreover, the furnace translation rate is not used in the interface boundary condition. It is believed that the interface in these simulations is therefore more free to follow the local physics of the solute transport rather than respond to a quasi-steady imposed growth condition.

At steady state at the outset of growth in a flat-bottomed THM experiment, Dost and Liu observe the "double-humped" interface which is caused by the downward flow hot liquid in the centre of the ampoule and local heating of the centre of the growth interface. This is corrected by increasing the rate of heat extraction through the centre region of the seed crystal resulting in an interface that is convex toward the liquid. This works because at steady state the solute concentration across the growth interface is uniform and the interface is isothermal. As the system translates, solute is incorporated by the advancing solid and the motion of the interface becomes dependant not on the temperature field but rather on the rate of solute transport to the growth interface. After some time, the interface depression returns but this time as a result of the convection of solute rather than heat.

In the present simulations, the depression required several hours to develop as a result of solute transport. Dost and Liu show the state of their interface after 10 min, but it is possible that the flattening achieved through cooling of the seed was short-lived after growth begain. It is also possible, however, that the use of the furnace translation rate in the interface boundary conditions obscured the variation in the growth rate caused by inadequate solute transport in the stagnant regions of the interface. In the present simulations, so long as convection is strong and the translation rate is large compared to the very slow rate of diffusive solute transport a depression will form in the centre of the growth interface caused by flow stagnation and depletion of the local solute.

One approach to reduce convection is improved thermal design aimed at reducing the temperature gradients in the solution zone. Figure 6.21 shows a simulation in which the furnace wall temperature is assumed to be much flatter than has been used to date. In this case, the furnace temperature is 810 °C within the solution zone and 775 °C elsewhere. The temperature gradients in such a system are reduced, and the interface is much flatter. The overall temperature has also been reduced. Thermal convection in this zone is reduced by 70 percent. This is likely closer to the experimental conditions that should be adopted in future work. It is noted, however that the temperature gradient at the growth interface is smaller and it is possible that

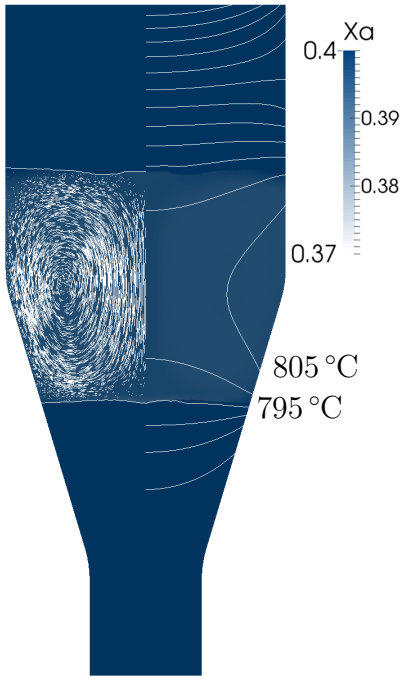

Figure 6.21: 25 mm simulation with lower temperature gradients. $u_{max} = 1.5\,\mathrm{mm/s}$, $Re = 180$

the interface will not be stable under these conditions. Solutal convection will also not be reduced, and very slow growth may be necessary to prevent excessive velocity and deformation of the interface. Such a system would likely benefit further from AAR or RMF.

During development of the software, simulations were conducted for the 65 mm diameter system as well as the 25 mm furnace. Unfortunately these were preliminary in nature, and a more thorough investigation of the transport regime was not possible within the time frame of the project. Qualitatively, results in the larger system appear to be identical to results in the smaller, but convection is even stronger and interfaces are even more sensitive to thermal conditions.

The current model was developed assuming axisymmetric conditions. Other authors have reported 3D simulations, including Dost and Liu and Stelian et. al. [40, 56]. Under unforced conditions their simulation results show axisymmetric flow patterns as should be expected from the THM geometry. When forced convection is added, though, flow fields can become fully 3D. The current model is therefore poorly suited to modelling RMF or AAR although approximate solution might be possible. It would also be interesting to simulate a THM experiment in which the temperature

field is deliberately non-axisymmetric as this might eliminate the stagnation point at the centre of the growth interface.

In principle the EVIE algorithm could be expanded for use in 3D. This would require implementing tetrahedral elements and standardizing the possible element topographies (sub-meshes with 1 to 7 liquid vertices). The challenge is purely one of implementation, but it would require significant effort.

Although full ternary mass transport was modelled well in 1D, ternary simulations in the axisymmetric model do not work well at the time of writing. The reasons are not yet clear, but they appear to be related to the compositions applied to newly dissolved or solidified vertices. Nevertheless, the success of the ternary model in 1D simulations suggests that the EVIE algorithm is capable of handling more than one solute and axisymmetric simulations of CdZnTe growth will be possible with modest additional development. Segregation of zinc does not appear to be a problem in THM, so if necessary binary simulations with the solute species chosen to be $Cd_{.95}Zn_{.05}Te$ could be used as a reasonable approximation to a full ternary mass transport model, but to date simulations have only been done assuming CdTe properties.

6.7 Conclusion

A new finite element model has been developed for THM. A fixed grid algorithm was developed for axisymmetric simulations with quadrilateral elements, extending a method previously applied to the solidification of pure metals. In this EVIE enrichment scheme, mixed-phase elements are subdivided by inferring the condition of a virtual interface and then eliminating its terms from the element equations. It is argued in Section 6.2.4 that the sharp interfaces assumed in the level set method are a better model for the interface between a compound and its solvent than the mixed solid/liquid properties assigned to interfacial cells in other fixed-grid discretizations such as phase field models. The need in THM to model not only energy transport through the interface but also mass transport, and the need for the interface motion to be strictly coupled to the mass transport alone makes a mushy solidification model less reasonable for the same reason that level set methods are chosen for the solidification of pure metals as opposed to alloys.

The new model has been applied successfully to the 1D simulation of ternary (CdZnTe) THM and the axisymmetric simulation of binary (CdTe) THM growth experiments.

The shape of the growth interface is strongly coupled with the velocity and concentration fields so that temperature gradients alone are not enough to ensure a flat or convex growth interface. Depressions form at flow stagnation points where the thickness of the diffusive boundary layer impedes growth. This is generally observed in the centre of the growth interface for these axisymmetric simulations and is consistent with experiments in this and other studies that show additional grains formed in this region.

In order to achieve flat interfaces, it will be necessary to suppress convection or to apply forced convection through RMF or AAR. These effects were not simulated due to time constraints and because they have been reported elsewhere to produce 3D flow structures that cannot be adequately captured by axisymmetric simulations.

6.8 Future Work

If the EVIE model is to be used to simulate forced convection, it should be expanded to a full 3D analysis. This would require significant effort to model the virtual interfaces within mixed elements.

Even with the axisymmetric model, further simulations of the growth experiments are possible. In particular the effect of the applied wall temperature on the velocity field and interface strength could not be fully explored before the end of this study. This is of great interest and might yet yield temperature profiles that give depression-free interfaces without the need for RMF or AAR. Approximate solutions could also be sought by applying RMF and AAR to the current axisymmetric model. Asimuthal velocity is implemented in the code, but the resulting flow structures would need to be validated against 3D simulations by other researchers.

Some minor challenges still exist with the current code, including the treatment of ternary diffusion at the solid-liquid interfaces. This should be resolved as soon as possible.

Chapter 7

Results and Discussion

7.1 Supporting Studies

The preliminary and supporting studies for this project were very successful. Tapered THM growth was demonstrated using 10 mm GaSb seeds to grow out to 25 mm diameter. Some success was also achieved with 25 mm seeds in a 50 mm diameter ampoule. That preliminary study suggested that tapered THM is not significantly more complicated than THM in straight ampoules, and it largely motivated the growth study in the more difficult and more significant telluride materials.

The first step toward the growth of CdTe was the production of suitable seeds using VGF. The growth process was developed quickly with very little optimization, but it was remarkably successful at producing large grains. This is due largely to the previous work done by others using the same growth equipment. Because detector-grade single crystals were not explicitly sought in this study, an unproven two-stage growth process could be tried as described in Section 4.4, and it appears to have been successful. Large grains up to 50 mm in diameter were nucleated using a CdTe melt that was heated isothermally just barely above its melting temperature. This nucleated crystal was maintained in a cooler zone of the furnace while the upper portion of the melt was superheated significantly and then solidified. The lack of optimization is evident in the finished ingots, all of which appear to have formed solid caps and solidified at least partially from both ends. Nevertheless, the production of very large grains in three 50 mm diameter ingots was enough to provide seed crystals for the entire THM growth study.

Synthesis and casting experiments for CdTe and $Cd_{.95}Zn_{.05}Te$ proved the ba-

sic functioning of the THM equipment and demonstrated that large grains can be produced without seeds and using crushed source material. As described in Section 4.3 both of these deviations from the traditional THM process represent potential economies because seed preparation represents the greatest cost and difficulty of a THM growth process and casting source material to the correct diameter represents an additional process and an opportunity for contamination or the introduction of a concentration gradient. Although unseeded growth was later shown to be ineffective for the production of large crystals, the use of crushed source material greatly simplified the preparation of growth experiments.

7.2 Simulations and THM Growth Experiments

Despite the success of preliminary growth studies using GaSb, single crystals have proven very difficult to grow from narrow seeds in the CdTe and CdZnTe systems. The technical development of the growth experiments is discussed in detail in Section 5.1, but their results are re-examined here in light of the simulation results that became available after the end of the experimental study.

Unfortunately, the simulations associated with this study were severely delayed by the development of a new finite element code. The EVIE approach chosen has the advantage that it confines the element enrichment to the finite element assembly process and does not require new terms such as porosity in the governing equations. The EVIE approach therefore appears to be simpler than, for example, the extended finite element method (X-FEM). In practise, however, implementation and debugging of the model was tremendously time-intensive and simulation results came too late to inform the associated experimental study before it was concluded.

Fundamentally, THM growth in tapered ampoules suffers from the same challenges as conventional THM growth using tellurium solutions. The Prandtl number for liquid tellurium, at 0.06 is ten times larger than that of liquid gallium used for the growth of GaSb. This larger Prandtl number results in very strong thermal convection. This commonly results in depressions in the growth interfaces in telluride growth experiments. This depression has commonly been interpreted is the result of convective heating, which is therefore remedied by selective cooling of the crystal through the base of the ampoule. Simulations in this study, however, show that even if the growth interface is cooled, the depression can occur during growth because of a different mechanism. The axisymmetric flow assumed in this work and observed

in 3D simulations by, for example, Dost and Liu [40], must have a stagnation point at the centre of the growth interface. In this region as well as at the ampoule wall, mass transport is dominated by diffusion no matter how strong the convection in the overall solution zone. The different transport regimes across the radius of the growth interface unavoidably produce different growth rates until a depression is formed and the interface temperature is lowered.

It was observed qualitatively in experiments that rotating the ampoule once every two minutes in alternating directions produced interfaces that were not only more symmetrical but also flatter (see for example Figure 5.11 and Figure 5.12). Unfortunately experiments were not similar enough to be compared definitively with and without rotation, but it is possible that the ampoule rotation served to disrupt the thermal convection as well as promote axisymmetry.

Actual axisymmetric simulations of THM growth were limited, but they give some insight into how the growth experiments of this study could have been improved. Most importantly, too much emphasis was placed in the growth study on extracting large amounts of heat through the base of the seed. Heat extraction is very helpful in melt growth where the motion of the interface is determined by the heat flux and latent heat at the interface, but in THM the motion of the interface is ultimately governed by the transport and incorporation of the solute in the solution zone. A small amount of convection is needed to carry solute from the dissolution to the growth interface, but strong convection creates unavoidable deformity of the growth interface due to the stagnation of the velocity field in the centre of the axisymmetric system. The emphasis of future experimental studies must be on the reduction of the convective flows in the solution zone through AAR, RMF or microgravity. At the very least, the design of future experimental THM furnaces should focus on producing a flatter temperature profile to reduce the peak temperature in the solution zone. One interesting possibility is also the prospect of deliberately breaking the axisymmetry of the traditional THM experiment in an effort to eliminate the stagnation point at the centre of the growth interface. Such an experiment cannot be modelled with the current EVIE software which assumes axisymmetry, and 3D simulations have not been published for such a case.

Despite strong thermal convection, largely single crystals of CdTe were grown at 25 mm diameter from 10 mm diameter seeds using sand-blasted quartz ampoules and crushed source material. When these experiments were replicated with CdZnTe source material on CdTe seeds in graphite-coated ampoules the seed crystals were

lost, but one experiment produced large enough grains to produce a 10 mm diameter CdZnTe seed to be mined.The crystal grown on this seed at 25 mm diameter can be seen in Figure 5.11. It is dominated by a single large grain with several twin defects and inset grains along the walls. This is partial success, but not convincing tapered growth. Two seeded CdTe growth experiments at 65 mm diameter produced multiple large grains, but both show two centimetres of outward growth. In the first, smaller grains first form in the centre of the growth interface is might be expected based on a posteriori simulations. In the second, massive tellurium inclusions and an apparently non-planar interface suggest either an insufficient temperature gradient or instability in thermal conditions. On balance, these experiments show that outward growth is possible, but significant development would be required to achieve it in practice.

Chapter 8

Conclusion

8.1 Conclusion

Experimental and numerical studies suggest that it is feasible to grow CdTe and CdZnTe crystals by the travelling heater method using seed crystals with reduced diameter. Development of a reliable process to do so is a prohibitive proposition, however.

Future growth studies would need to reduce thermal convection and likely grow very slowly in order to avoid producing an undesireable interface shape. As a result, it may take two or more weeks to grow through the tapered region of a THM ampoule, which is expensive for a commercial growth process and unfortunately long for a scientific study. Ideally, a research program aimed at achieving tapered growth should have access to five to ten furnaces of similar design and the materials and cutting tools necessary to repeatedly quench and slice experiments under various growth conditions. If further development were to be attempted with one or two furnaces, then simulations suggest that the best approach is very careful control of the wall temperature in and below the solution zone and disruption of thermal convection using AAR or RMF. This work could not be pursued in the current study due to time constraints and the nature of the available THM equipment.

Several supporting technologies were studied and given experimental consideration in preparation for the THM growth study. The diffusivity of CdTe was measured in liquid Te under THM conditions using dissolution experiments. Measured values agreed with first-principles calculations performed by other research groups, and the observed results agree with analytical models and were used to validate the simulation

software developed to support the THM growth study.

CdTe seeds were produced by casting 50 mm diameter boules using an adapted VGF process and an untested approach to managing the degree of superheating in the melt. The resulting boules contained very large grains from which the seed crystals were cut and then etched to confirm their (111)A orientation.

THM synthesis and casting experiments were conducted in preparation for the growth studies. $Cd_{.95}Zn_{.05}Te$ cast by THM was contributed to a space-based growth study conducted by the European Space Agency.

Although unseeded THM produced large grains in experiments at both 25 mm and 65 mm diameter constitutional supercooling appears to have prevented the initial nucleation of large grains and a seed crystal appears to be required to achieve large oriented growth at the outset of THM.

After much technical development, largely single crystal 25 mm diameter boules of CdTe and CdZnTe have been produced using 10 mm seeds. Two seeded growth experiments of 65 mm CdTe boules from 25 mm diameter seeds also showed outward growth. The first experiment resulted in several large grains sharing a (111)-upward orientation, while the second showed definite but short-lived outward growth. All crystals grown in this work contain large secondary grains and twin defects.

A new finite element code was written in C++ using the level set method to model the moving interfaces with a stationary mesh. It is argued that the sharp interfaces used in the level set method are a better model for physical THM interface than the mushy zones associated with other fixed-grid discretizations such as phase field models. Unfortunately the development of the simulation software was finished too late to inform the experimental study. Later simulations of the experiments indicate that the growth interfaces likely formed depressions at the stagnation points at their centres and at the walls leading to the formation of secondary grains.

The experimental results suggest that sand blasting is an excellent surface treatment for experimental growth of CdTe. Crushed source material consolidated by a downward THM pass did not appear to affect the results compared to pre-cast source material. Ampoule rotation was observed to promote axisymmetry and favourable interface shape in both the large and small THM systems. Varying the rate of heat extraction through the ampoule base between experiments did not measurably improve the seeded growth experiments. In order to reduce the change in thermal conditions in the early stages of growth, active control of the heat extraction should be used to compensate for the thermal resistance of the growing seed. More focus should also

be placed on the reduction of thermal and solutal convection which are known to be very strong in liquid tellurium systems.

8.2 Future Work

If CdTe and CdZnTe crystals are to be grown from small seeds by THM, a significant further development process is required. In particular, new furnace equipment must be designed that reduces the drastic change in the thermal conditions during growth through the tapered region. The temperature at the base of the seed should be controlled actively to maintain a consistent heat flux at the growth interface. In general, a flatter temperature profile is desirable which might be accomplished through the use of a conductive ring around the solution zone, but further thermal design is needed before new equipment can be specified.

Results of the current experimental and numerical studies show a pressing need to reduce convection in the liquid zone. Future work should therefore focus on the beneficial impact of AAR and RMF. Ideally the existing software would be expanded to allow full 3D simulations of these techniques, and both capabilities should be built into future experimental furnaces.

It should be noted that in the past decades THM growth of large telluride crystals has passed from academic research to industrial production by large companies. These have the benefit of many furnaces operating concurrently under similar conditions. The time and expense required to achieve large diameter growth using small seed crystals may be too large to be achieved by academic researchers with one or two furnaces. Whether such growth is possible likely depends less on the physics of the problem itself and more on the economics of the necessary technical development.

Bibliography

[1] S.M. Sze. *Semiconductor Devices: Physics and Technology*. John Wiley & Sons, Limited, 1985.

[2] M.A. Green, K. Emery, Y. Hishikawa, W. Warta, and E.D. Dunlop. Solar cell efficiency tables (version 43). *Progress in Photovoltaics: Research and Applications*, 22(1):1 – 9, 2014.

[3] Antoni Rogalski. Progress in focal plane array technologies. *Progress in Quantum Electronics*, 36(2-3):342 – 473, 2012.

[4] R. Arlt, K.-H. Czock, and D.E. Rundquist. Overview of the use of CdTe detectors for the verification of nuclear material in nuclear safeguards. In *Nuclear Instruments & Methods in Physics Research, Section A (Accelerators, Spectrometers, Detectors and Associated Equipment)*, volume A322, pages 575 – 82, 1992.

[5] P. Rudolph, T. Boeck, and P. Schmidt. Thermodiffusion and morphological stability in convectionless crystal growth systems from melts and melt-solutions. *Crystal Research and Technology*, 31(2):221 – 9, 1996.

[6] V. Baventsov, V. Corregidor, K. Benz, T. Feltgen, M. Fiederle, and E. Dieguez. Self-cleaning effect and compensation mechanism in Cl-doped high resistivity cadmium telluride. In *Proceedings of SPIE - The International Society for Optical Engineering*, volume 3794, pages 88 – 95, 1999.

[7] P. Rudolph. Fundamental studies on Bridgman growth of CdTe. *Progress in Crystal Growth and Characterization of Materials*, 29(1-4):275 – 381, 1994.

[8] M.A. Berding. Native defects in CdTe. *Physical Review B*, 60(12), 1999.

[9] J. Steininger, A.J. Strauss, and R.F. Brebrick. Phase diagram of the Zn-Cd-Te ternary system. *Journal of the Electromchemical Society*, 117(10):1305–1309, 1970.

[10] Robert F. Brebrick. The Cd-Te phase diagram. *Calphad: Computer Coupling of Phase Diagrams and Thermochemistry*, 34(4):434 – 440, 2010.

[11] P. Rudolph. Non-stoichiometry related defects at the melt growth of semiconductor compound crystals - a review. *Crystal Research and Technology*, 38(7-8):542 – 54, 2003.

[12] P. Rudolph and M. Muhlberg. Basic problems of vertical Bridgman growth of CdTe. In *Materials Science & Engineering B (Solid-State Materials for Advanced Technology)*, volume B16, pages 8 – 16, 1993.

[13] H.M. Hobgood, B.W. Swanson, and R.N. Thomas. Czochralski growth of CdTe and CdMnTe from liquid encapsulated melts. *Journal of Crystal Growth*, 85(3):510 – 520, 1987.

[14] U.N. Roy, A. Burger, and R.B. James. Growth of CdZnTe crystals by the traveling heater method. *Journal of Crystal Growth*, 379:57 – 62, 2013.

[15] F.W. Wald and R.O. Bell. Natural and forced convection during solution growth of CdTe by the traveling heater method (THM). *Journal of Crystal Growth*, 30(1):29 – 36, 1975.

[16] A. El Mokri, R. Triboulet, A. Lusson, A. Tromson-Carli, and G. Didier. Growth of large high purity, low cost uniform CdZnTe crystals by the 'cold travelling heater method'. volume 138, pages 168 – 74, 1994.

[17] M. Salk, M. Fiederle, K.W. Benz, A.S. Senchenkov, A.V. Egorov, and D.G. Matioukhin. CdTe and $CdTe_{0.9}Se_{0.1}$ crystals grown by the travelling heater method using a rotating magnetic field. volume 138, pages 161 – 7, 1994.

[18] A.S. Senchenkov, I.V. Barmin, A.S. Tomson, and V.V. Krapukhin. Seedless THM growth of $Cd_xHg_{1-x}Te$ (x=0.2) single crystals within rotating magnetic field. volume 197, pages 552 – 6, 1999.

[19] C.K. Ghaddar, C.K. Lee, S. Motakef, and D.C. Gillies. Numerical simulation of THM growth of CdTe in presence of rotating magnetic fields (RMF). *Journal of Crystal Growth*, 205:97–111, 1999.

[20] H. Shiraki, M. Funaki, Y. Ando, A. Tachibana, S. Kominami, and R. Ohno. THM growth and characterization of 100 mm diameter CdTe single crystals. *IEEE Transactions on Nuclear Science*, 56(4):1717 – 23, 2009.

[21] J. MacKenzie, F.J. Kumar, and H. Chen. Advancements in THM-grown CdZnTe for use as substrates for HgCdTe. *Journal of Electronic Materials*, 42(11):3129 – 32, 2013.

[22] Henry Chen, Salah A. Awadalla, Jason Mackenzie, Robert Redden, Glenn Bindley, A.E. Bolotnikov, G.S. Camarda, G. Carini, and R.B. James. Characterization of traveling heater method (THM) grown $Cd_{0.9}Zn_{0.1}Te$ crystals. volume 54, pages 811 – 816, 2007.

[23] J. Roszmann. Application of rotating magnetic fields to the travelling heater method growth of GaSb and the synthesis of CdTe. Master's thesis, University of Victoria, Canada, 2009.

[24] J. Roszmann, S. Dost, and B. Lent. Crystal growth by the travelling heater method using tapered crucibles and applied rotating magnetic field. *Crystal Research and Technology*, 45(8):785 – 790, 2010.

[25] M. Inoue, I. Teramoto, and S. Takayanagi. Etch pits and polarity in CdTe crystals. *Journal of Applied Physics*, 33(8):2578 – 2582, 1962.

[26] W.J. Everson, C.K. Ard, J.L. Sepich, B.E. Dean, G.T. Neugebauer, and H.F. Schaake. Etch pit characterization of CdTe and CdZnTe substrates for use in mercury cadmium telluride epitaxy. volume 24, pages 505 – 10, 1995.

[27] K. Nakagawa, K. Maeda, and S. Takeuchi. Observation of dislocations in cadmium telluride by cathodoluminescence microscopy. *Applied Physics Letters*, 34(9):574–575, 1979.

[28] W.G. Pfann. *Zone melting*. Wiley series on the science and technology of materials. Wiley, 1966.

[29] S. Dost, Y.C. Liu, J. Haas, J. Roszmann, S. Grenier, and N. Audet. Effect of applied electric current on impurity transport in zone refining. *Journal of Crystal Growth*, 307(1):211 – 218, 2007.

[30] J. Roszmann, Y.C. Liu, S. Dost, B. Lent, S. Grenier, and N. Audet. Use of rotating magnetic field for selenium impurity transport in zone refining of tellurium and cadmium. *Fluid Dynamics and Materials Processing*, 5(3):231 – 244, 2009.

[31] C. Stelian and T. Duffar. Influence of rotating magnetic fields on THM growth of CdZnTe crystals under microgravity and ground conditions. *Journal of Crystal Growth*, 429:19 – 26, 2015.

[32] C.P. Khattak and F. Schmid. Growth of CdTe crystals by the heat exchanger method (HEM). In *Proceedings of the SPIE - The International Society for Optical Engineering*, volume 1106, pages 47 – 55, 1989.

[33] J. Roszmann, M. Sekhon, and S. Dost. Measurement of the diffusivity of CdTe in liquid Te at crystal growth temperatures. *Journal of Crystal Growth*, 411:30 – 3, 2015.

[34] X. Ye, B. Tabarrok, and D. Walsh. The influence of thermosolutal convection on CdTe growth by the traveling heater method. *Journal of Crystal Growth*, 169:704–714, 1996.

[35] V. Kumar, S. Dost, and F. Durst. Numerical modeling of crystal growth under strong magnetic fields: An application to the travelling heater method. *Applied Mathematical Modelling*, 31:589–605, 2007.

[36] E. Javierre, C. Vuik, F.J.Vermolen, and S. van der Zwaag. A comparison of numerical models for one-dimensional Stefan problems. *Journal of Computational and Applied Mathematics*, 192:445–459, 2006.

[37] N. Armour and S. Dost. Effect of an applied static magnetic field on silicon dissolution into a germanium melt. *Journal of Crystal Growth*, 311:780–782, 2009.

[38] Y. Liu, S. Dost, B. Lent, and R.F. Redden. A three-dimensional numerical simulation model for the growth of CdTe single crystals by the travelling heater method under magnetic field. *Journal of Crystal Growth*, 254:285–297, 2003.

[39] Eunjung Ko, M.M.G Alemany, J.J. Derby, and J.R. Chelikowsky. Ab initio simulations of nonstoichiometric Cd_xTe_{1-x} liquids. *Journal of Chemical Physics*, 123(8), 2005.

[40] Sadik Dost and YongCai Liu. Controlling the growth interface shape in the growth of CdTe single crystals by the traveling heater method. *Comptes Rendus - Mecanique*, 335(5-6):323 – 329, 2007.

[41] U.N. Roy, S. Weiler, and J. Stein. Growth and interface study of 2 in diameter CdZnTe by THM technique. *Journal of Crystal Growth*, 312(19):2840 – 5, 2010.

[42] T.J.R. Hughes, Wing Kam Liu, and A. Brooks. Finite element analysis incompressible viscous flows by the penalty function formulation. *Journal of Computational Physics*, 30(1):1 – 60, 1979.

[43] A.N. Brooks and T.J.R. Hughes. Streamline upwind/Petrov-Galerkin formulations for convection dominated flows with particular emphasis on the incompressible Navier-Stokes equations. volume 32, pages 199 – 259, 1982.

[44] J.C. Heinrich and R.S. Marshall. Viscous incompressible flow by a penalty function finite element method. *Computers and Fluids*, 9(1):73 – 83, 1981.

[45] M.P. Reddy, J.N. Reddy, and H.U. Akay. Penalty finite element analysis of incompressible flows using element by element solution algorithms. *Computer Methods in Applied Mechanics and Engineering*, 100(2):169 – 205, 1992.

[46] T.J.R. Hughes, L.P. Franca, and M. Balestra. A new finite element formulation for computational fluid dynamics: V. circumventing the Babuska-Brezzi condition: a stable Petrov-Galerkin formulation of the Stokes problem accommodating equal-order interpolations. *Computer Methods in Applied Mechanics and Engineering*, 59(1):85 – 99, 1986.

[47] T. Skrzypczak and Ewa Wegrzyn-Skrzypczak. Mathematical and numerical model of solidification process of pure metals. *International Journal of Heat and Mass Transfer*, 55, 2012.

[48] A.D. Brent, V.P. Voller, and K.J.Reid. Enthalpy-porosity technique for modeling convection-diffusion phas change: application to the melting of a pure metal. *Numerical Heat Transfer*, 13(3), 1988.

[49] J. Chessa, P. Smalinski, and T. Belytschko. The extended finite element method (XFEM) for solidification problems. *International Journal for Numerical Methods in Engineering*, 53, 2002.

[50] J. Chessa and T. Belytschko. An enriched finite element method and level sets for axisymmetric two-phase flow with surface tension. *International Journal for Numerical Methods in Engineering*, 58, 2003.

[51] Christophe Geuzaine and Jean-Francois Remacle. Gmsh: A 3-D finite element mesh generator with built-in pre- and post-processing facilities. *International Journal for Numerical Methods in Engineering*, 79(11):1309 – 1331, 2009.

[52] W. Bangerth, R. Hartmann, and G. Kanschat. Deal.ii-a general-purpose object-oriented finite element library. *ACM Transactions on Mathematical Software*, 33(4), 2007.

[53] T. Davis. *Direct Methods for Sparse Linear Systems*. Society for Industrial and Applied Mathematics, 2006.

[54] A. Henderson, J. Ahrens, and C. Law. *The Paraview guide : a parallel visualization application*. Kitware, Inc., New York, 2004.

[55] Hàn Thế Thành. *Micro-typographic extensions to the TEXtypesetting system*. PhD thesis, Masaryk University, October 2000.

[56] C. Stelian. Numerical optimization of thermal field in CdTe crystal growth by travelling heater method. *Crystal Research and Technology*, 48(9):603 – 11, 2013.